Escola de Camins
Escola Tècnica Superior d'Enginyeria de Camins, Canals i Ports
UPC BARCELONATECH

TREBALL FINAL DE MÀSTER

Numerical analysis of shaft construction in overconsolidated clays

Treball realitzat per:
Sergi Collell Carbonell

Dirigit per:
Alberto Ledesma Villalba
Francesc Xavier Mirada Larroca

Màster en:
Enginyeria de Camins, Canals i Ports

Barcelona, Juny del 2019

Departament d'Enginyeria Civil i Ambiental

Numerical analysis of shaft construction in overconsolidated clays

Sergi Collell Carbonell

in partial fulfilment of the requirements for the degree of

Master of Science
in Civil Engineering (Ingeniero de Caminos, Canales y Puertos)

at the Universitat Politècnica de Catalunya,
Barcelona, June 2019

Supervisors: **Prof. Dr. Alberto Ledesma** (UPC)
Francesc Xavier Mirada (Arup)

UNIVERSITAT POLITÈCNICA DE CATALUNYA
BARCELONATECH
Department of Geotechnical Engineering
and Geo-Sciences

Abstract

Nowadays, the cities are constantly increasing in population and urbanisation and some demographics studies point out that in 2050 two thirds of the world population will live in cities. To provide this new population and urbanisation with the basic supplies, telecommunications utilities and roads or rails transportation needs underground infrastructures. To facilitate construction, to provide access and egress or ventilation or to allow entry or exit of basic supplies, shafts are constructed along the length of the tunnels. Circular shape shafts are commonly constructed, in order to reduce the need for propping the excavation produced by the circular structural properties. The ground movements due to shaft excavation are extremely important because it causes impacts to the nearby infrastructures located on the ground surface and others underground infrastructures. However, overestimating the movement can lead to increase the construction cost with using another construction method or the structural design. Until recently there were few well-documented case studies of circular shafts which made it difficult to estimate the ground movements due to a circular shaft excavation. Within this work the Limmo Peninsula Tunnelling Auxiliary and Main shafts documented in Joseph Newhouse (2017) are correctly modelled. Furthermore, the sensitivity on ground movements due shaft diameter, supported and unsupported excavation depth and overall depth of the shaft is studied. This provides a numerically expanded data-base on circular shafts with the use of finite element methods.

Key words: circular shafts, ground movements, soil movements, settlements, PLAXIS 2D, Limmo Peninsula Tunnelling case study, SCL, Sheet pile, Excavation Before Support, Support Before Excavation

Acknowledgments

I would like to express my special appreciation and thanks to my advisors: Pr. Dr Alberto Ledesma and Francesc Xavier Mirada who have done a great effort helping to develop this work during the 2018/19 academic year and all the things I have learnt from them. Your advice and your limitless availability are of incalculable worth.

Besides, I would like to acknowledge UPC and the Erasmus Programme that gave me the opportunity to go on a mobility programme on the VUT Brno, where I met incredible people from all over the world.

Thanks to all my friends that made my every-day life more comfortable and easier. Also, to the ones that I met in Brno, they were not here but we kept the contact no-matter where they lived or stayed. Thank you all!

Finally, I would like to thank to my parents and family. They were the ones that encouraged and supported me all over these years, when I needed them, they were always there!

Table of contents

Annexes

List of figures

List of tables

1 Introduction

1.1 Background and motivation

Nowadays, the cities are constantly increasing in population and urbanisation and some demographics studies point out that in 2050 two thirds of the world population will live in cities. To provide this new population and urbanisation with the basic supplies, telecommunications utilities and roads or rails transportation needs underground infrastructures. But the scale of this underground construction is also increasing with less space at the ground surface and improving construction capability.

To facilitate construction, to provide access and egress or ventilation or to allow entry or exit of basic supplies, shafts are constructed along the length of the tunnels. Wherein, the circular shape shafts are commonly constructed, in order to reduce the need for propping the excavation produced by the circular structural properties.

The ground movement due to shaft excavation are extremely important because it causes impacts to the nearby infrastructures located on the ground surface and others underground infrastructures. However, overestimating the movement can lead to increase the construction cost with using another construction method or the structural design.

The lack of circular shaft case studies historically has limited the development of empirical methodologies. But some growing knowledge (Faustin et al., 2017; Schwamb, 2014; GCG, 2007) accurate that ground movement predictions are also produced by the ground conditions, structural design and the construction method instead only considering the shaft geometry.

During the last seven years, the new London infrastructure railway (known as Elizabeth line) that has been constructed by Crossrail, that has been provided an opportunity to improve current predictions with several new case studies.

1.2 Scope of this work

The principle aim of this work is to contribute to the validation of the new prediction of ground movement due to shaft excavation proposed by Joseph Newhouse (2017) with the simulation of the Main Shaft and the Auxiliary Shaft at Limmo Peninsula Tunnelling Site. The two shafts at Limmo Peninsula were well instrumented and documented so the shaft geometry, the dewatering undertaken during the construction and the ground movement after the excavation ended is known. Within in this work, the Main Shaft and the Auxiliary Shaft are modelled and compared to the real measured data observed in the site. Additionally, the influences of the shaft diameter, the construction method and the shaft depth are studied.

1.3 Outline and content

A general overview of the existing literature about the recently developed work concerning the ground movement due to shaft excavation in overconsolidated clays is given in *Chapter 2*. The ground movement empirical predictions due to shaft construction are presented. Wherein, it is categorised the most common construction method by two; support before excavation (SBE) and excavation before support (EBS). Moreover, general current methods for predicting the movement that occurs are presented and a new methodology based on the settlement database by Joseph Newhouse (2017).

Chapter 3 summarizes the constitutive models with the governing equation for strain and stress deformation and for fluids. Furthermore, the Strain Softening Mohr-Coulomb, the Hardening Soil and the Hardening Soil – Small Strains used to simulate the behaviour of the Limmo Peninsula Tunnelling Site shafts in overconsolidated clays are presented.

In Chapter 4, an overview of the structural and construction sequence; and the geological stratigraphy and the groundwater of the Main Shaft and the Auxiliary Shaft at Limmo Peninsula Tunnelling Site.

In Chapter 5, the geometry, boundary conditions, the mesh, the materials and the dewatering process used to model the two shafts are presented.

Chapter 6 presents the results of the numerical analysis of the Main Shaft and the Auxiliary Shaft. The ground movement due to shaft excavation are compared to the formula presented by GCG (2007) and the field data measured at the end of the excavation. Moreover, the minimum settlement normalised by the excavation depth against the shaft diameter normalised by the excavation depth is also presented to analyse the behaviour during the excavation progress.

The parametric study concerning the shaft geometry and the wall lining is given in Chapter 7. Using the same excavation depth and lining wall of the Auxiliary Shaft at Limmo Peninsula Tunnelling Site in order to study the effect of different diameter. Then, the influence of the lining wall with different construction method depth is studied. Also, a parametric study of a constant normalised diameter over excavation depth is provided

The concluding remarks are presented in Chapter 8.

Finally, Chapter A refers to a set of annexes including additional figures from Plaxis regarding ground displacements, stresses and strains at different construction stages for both shafts.

2 State of the Art

Ground movement due to shaft construction can result in damage to surrounding structures and utilities. Predictions of the magnitude and extent of movement must be made to assess the risk of damage to a given asset.

In this chapter a general overview of the existing literature about soil movements due to shaft construction, empirical, semi-empirical predictions methodologies and the use of numerical methods (i.e. finite element methods) is given.

2.1 Soil movements due to Shaft Construction

2.1.1 Introduction

The magnitude and extent of ground movement around an excavation depends as much on the method of construction as on any other single factor. Although the designer may specify a particular form or method of construction, the precise details of support, their sequence and timing cannot be controlled accurately since they depend on a large number of factors which vary from day to day on a construction site.

Since the fifty's, researchers have carried out a great effort to predict and understand settlements induced by underground construction in order to avoid failures and catastrophes (Terzaghi and Peck, 1948; Simpson, et al., 1979). Considerable advances in the understanding of the ground effects using numerical modelling has been done recently. Although finite element methods and numerical modelling have become a day-to-day tool for designers, it is still important to have semi-empirical or calibrated expressions in order to assess the movements due to shaft construction.

2.1.2 Causes of ground movement due to shaft construction

Ground movements due to shaft construction can be caused by a number of different reasons. This can include, but not limited to, the following:

- Type of or shaft lining installation and excavation. Driving or boring piles may cause vibrations, however, excavating a panel into the ground or excavating directly without support may involve a soil relaxation behind the wall that will lead to different kind of movements.
- Changes in the groundwater regime due to seepage, consolidation, etc.
- Other site-specific sources of movements like compensation or permeation grouting, nearby excavations, installation of anchors, etc.

It should be noted that many of the site-specific causes cannot easily be predicted by analysis or assessment and each shaft represents a singular structure, with specific ground conditions and

structural details with different designers and contractors involved. However, in Faustin et al. (2017) the following two main categories of circular shaft were identified.

1. The shaft lining is installed prior to excavation: support before excavation (SBE).
2. The shaft is constructed by concurrently excavating the ground and installing the shaft lining: excavation before support (EBS).

A brief outline of the most commonly used construction methods in each category is presented in Table 2.1.

Category	Method	Construction details
Lining installed prior to excavation (SBE)	Contiguous / Secant piling	Bored piles are constructed in a ring, either with gaps between the piles (contiguous), or overlapping piles (secant), prior to excavation of the shaft.
	Diaphragm walls	A grab or hydrofraise is used to excavate a panel trench, which is then filled with concrete. A ring of panels is formed prior to excavation of the shaft.
	Sheet piling	Sheet piles are driven into the ground. These may be supported by ring beams or anchors.
Lining installed concurrently with excavation (EBS)	Caisson	Rings of prefabricated segments are constructed at ground level on top of the previous ring and driven into the ground as the shaft is excavated.
	Sprayed concrete lining (SCL)	Shotcrete is pneumatically sprayed onto the exposed ground as the shaft is excavated. Structural reinforcement may be provided by a mesh, or reinforcing fibres added to the shotcrete.
	Underpinning	As the shaft is excavated, the exposed ground is supported by prefabricated segments in an underpinning operation. Each ring of segments is installed below the previous ring.

Table 2.1 Shafts construction methods (Schwamb 2014 and J. Newhouse 2017)

Ground movement due to shaft construction is produced by three general causes that include both categories: due to installation of the wall, excavation in front of the wall and changes in ground water regime. Table 2.2 presents a summary of the aspects that contribute to this movement generation. Heave on the passive and the active side of the wall is produced by the unloading of the ground excavation. All the other factors in Table 2.2 produce vertical displacements of the ground behind the wall.

Cause	Factor	Details
Installation of the wall	Construction method	The construction method depends on the geological stratigraphy and the mechanism of the ground movement due to wall installation.
	Construction duration	Long periods could generate soil relaxation or deflection on the lining wall
Excavation in front of the wall	Excavation depth	Deeper excavation produces higher displacements.
	Shaft diameter	A larger diameter trends to a greater ground movement.
	Reduced passive resistance	Reduced passive resistance due to excavation results in horizontal displacement of the wall, and consequently ground movement behind the wall.
	Heave of excavation base	During the shaft excavation on the passive side of the wall produces an unloading of the ground. This effect causes ground movement outside the excavation on the passive and the active side.
	Ground strength and stiffness	The soil strength influence on the ground movement. Soft ground will produce higher displacements as the stiff clays
	Ground water pressures	The groundwater pressure produces wall deflection, thus ground movement behind the shaft wall.
	Construction sequence	Shafts where installation and excavation are concurrent produce higher ground movement than where installation occurs prior to excavation.
	Quality of the workmanship	Construction problems or poor workmanship can cause damaging ground mo°1vement.

Cause	Factor	Details
Changes in groundwater regime	Dewatering during construction	Dewatering during construction increases effective stress, resulting in vertical ground movement.

Table 2.2 Causes of ground movement due to shaft construction
(Gaba, et al., 2017; Mot McDonald, 2013; Burland, et al., 2012; and Newhouse, 2017)

2.2 Empirical predictions methodology

2.2.1 Introduction

Ground movements around excavations can be assessed in broad terms from published data from sites with comparable conditions.

2.2.2 Movements due to excavation in front of a wall

When an excavation is formed in the ground, horizontal stresses are removed from the side and vertical stresses from the base. Peck (1969) summarised the observations of vertical movement around several excavations in various soil types is due to the relief of horizontal stress.

In case of vertical pressure, the mechanism of behaviour is perhaps best explained when a downward vertical stress is applied to the soil surface producing a negative (downward) vertical movement. On the other hand, an upward vertical stress produces a positive vertical movement (upward).

2.2.3 Circular shafts

Regarding ground movements produced by shaft excavation, B. M. New & K. H. Bowers (1994) reported surface monitoring measurements for the construction of a shaft at the Heathrow Express Trial Tunnel. The data were taken from two lines of surface measuring stations radially from the shaft. The shaft was 11 meters of diameter and with 26 meters deep.

New & Bowers (1994) presented Equation 2.1 to estimate the vertical movement.

$$\delta_v(x) = \frac{\alpha(H-x)^2}{H} \tag{2.1}$$

where the vertical displacements δ_v is a function of the distance behind the shaft wall ($x \leq H$), H is the depth of the shaft and α is an empirical constant dependent on ground conditions and construction method. For New & Bowser (1994) the best fit for α value is 0.0006 (settlement at shaft wall equal to 0.06% of excavation depth).

The horizontal movement was also described, and while all markers considered to be ‘not altered’, during the construction process indicated less than 5 mm horizontal movement, and because of the significant scatter no trend line was drawn.

The New & Bowers (1994) formula forms the basis of numerous industry design standards for shafts in stiff clays.

2.2.4 Recent developments and case studies

The most used ground movement prediction methods are outlined below.

2.2.4.1 Gaba et al. (2003) and Gaba et al. (2017)

Gaba et al. (2017) collated available horizontal and vertical ground movement data on 'Long walls' relating to the installation of bored and diaphragm walls embedded in stiff clays. Whilst, New & Bowers (1994) ground movement is predicted by excavation depth, H, Gaba et al. (2017) present the data normalised by wall depth, h. Nevertheless, Gaba et al. (2003) relate the ground movement due to excavation to the bounds for 'high' and 'low' stiffness support wherein is predicted by the excavation depth, H.

2.2.4.2 London Underground (2014)

London Underground (2014) use the ground movement data from the sources presented in Gaba et al. (2003), combined with additional case histories predominantly in London Clay, to derive their own trend lines for vertical and horizontal ground movement. Also defines two types of rectangular deep excavation. Figure 2.1 shows the geometry and the abbreviation of London Underground (2014). Long walls have a horizontal length, L, substantially greater than the excavation depth, H (L/H >2.5). Short walls have a ratio less or similar order to 1. The respective formulae to predict the movement on Long walls are presented in Equation 2.2 (for vertical movement) and Equation 2.3 (for horizontal movement). On short walls, they present tabulated reduction factors (Table 1 of London Underground, 2014), to account for the reduced length of wall, on Equation 2.2 and Equation 2.3.

$$\delta_{\mathrm{v}}(x) = 0.0015H.e^{\frac{1-\left(1+\frac{2x}{3H}\right)^2}{2}} \tag{2.2}$$

$$\delta_{\mathrm{h}}(x) = -(0.0008H - 0.00016x) \tag{2.3}$$

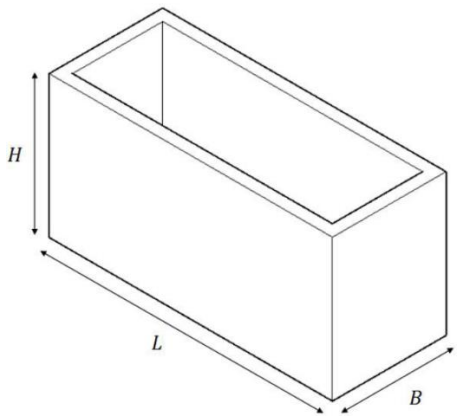

Figure 2.1 Box shaft geometry (J. Newhouse, 2017)

2.2.4.3 Mott MacDonald (2013)

Mott MacDonald (2013) presented Equation 2.4. The equation is only used for circular shaft structure.

$$\delta_v(x) = \frac{a}{R} \times \frac{(RH - x)^2}{RH} \tag{2.4}$$

The equation reduces to the expression proposed by New & Bowers (1994), if R = 1. The best fit α value is 0.06% for Mott MacDonald (2013).

2.2.4.4 GCG (2007)

GCG (2007) present vertical and horizontal ground movement prediction curves (Equation 2.5 and Equation 2.6, respectively) based on the hogging section of a Gaussian error function for box excavations and circular shafts. The curves are defined by the distance behind the wall to negligible movement and the maximum settlement. Each excavation has different defining parameter values, for circular shaft are proposed on Table 2.3 and box excavation are defined in Table 2 of GCG (2007).

$$\delta_{\mathrm{v}}(x) = \delta_{\mathrm{v,max}} e^{1/2} e^{\frac{-\left(x+\frac{2E}{3}\right)^2}{2\left(\frac{2E}{3}\right)^2}} \tag{2.5}$$

$$\delta_{\mathrm{h}}(x) = -\frac{\delta_{\mathrm{h,max}}}{\delta_{\mathrm{v,max}}}\left(1+\frac{3x}{2E}\right).\delta_{\mathrm{v}}(x) \tag{2.6}$$

Equation 2.5 defines the vertical ground movement at distance, x, behind a shaft wall using two parameters, the maximum vertical movement at the wall, $\delta_{\mathrm{v,max}}$, and the extent of the settlement trough, E. These may both be normalised by excavation depth, H, to give α and R respectively (Equation 2.7 and Equation 2.8).

$$\alpha = \frac{\delta_{\mathrm{v,max}}}{H} \tag{2.7}$$

$$R = \frac{E}{H} \tag{2.8}$$

The values for circular shafts in Table 2.3, were proposed following numerical analysis, and 'anecdotal evidence from Jubilee Line Extension'. They show the maximum settlement and the extent of the extent settlement trough to be a function of shaft diameter. It is noted by GCG (2007) that these values are based on very little field data. Nevertheless, GCG (2007) predicts a wider settlement trough, E, this is a result of a Gaussian form of the formula proposed whereby at the trough extent, settlement is still $0.07\delta_{v,max}$.

	Horizontal movement	Vertical movement	
	$\frac{\delta_{h,max}}{\delta_{v,max}}$	$\alpha = \frac{\delta_{v,max}}{H}$	$R = \frac{E}{H}$
D < 10 m	1	0.006·D	1
10 m < D < 25 m	1	0.006·D	1 + (D – 10)/15
D > 25 m	1	0.15	2

Table 2.3 GCG (2007) parameters for circular shaft ground movement predictions, D in metres (Table 3 of GCG, 2007)

In case of box shaft, GCG (2007), presented vertical ground movement data for long walls in stiff clay normalised by excavation depth (see Figure 2.2). It is shown in the Figure a couple of curves as bounds for 'high' and 'low' stiffness support system that is presented by Gaba et al. (2003). It can be observed that a large number of results which lie outside high stiffness bound would be categorised as high stiffness. Albeit, there are some ground movement data with a low plan aspect (L/B < 2, being B the shorter planar dimension of a box shaft) closer to high stiffness boundary

(Figure 2.3). It is produced by the corners of an excavation that restrict ground movement behind the wall

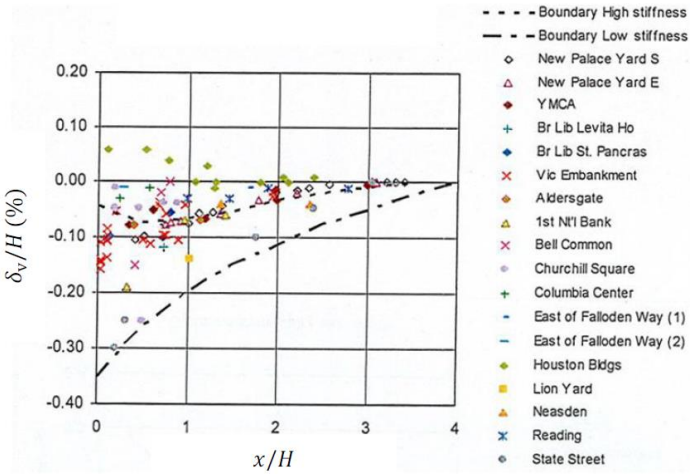

Figure 2.2 Vertical ground surface movement due to excavation in stiff clay for all plan aspect ratios (GCG, 2007)

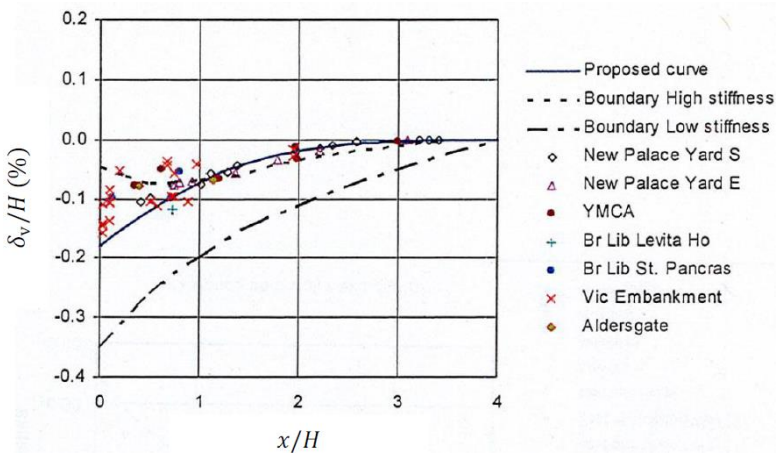

Figure 2.3 Vertical ground surface movement due to excavation in stiff clay for low plan aspect ratios (GCG, 2007)

2.2.4.5 Pairaudeau (2011)

Pairaudeau (2011) modified the formula presented by GCG (2007) (Equation 2.5) and proposed Equation 2.9, along with linear relationships for determining the maximum settlement, and extent of the settlement trough (Equation 2.10 and Equation 2.11). Pairaudeau (2011) conducted 1 g small model test in dry sand to investigate the surface settlement around circular shaft in relation to the diameter, D.

$$\delta_v(x) = \delta_{v,max} e^{1/2} e^{\frac{-\left(\frac{x}{H}+\frac{2E}{3H}\right)^2}{2\left(\frac{2E}{3H}\right)^2}} \quad (2.9)$$

$$\delta_{v,max} = 0.0008D + 0.0008H \quad (2.10)$$

$$E = 0.3D + 0.12H \quad (2.11)$$

2.2.4.6 Comparison ground movement prediction method

To compare the behaviour of the formulae of the ground movement prediction methods presented above, predictions of the settlement and the horizontal ground movement for the Heathrow Express Trial shaft reported in New & Bowers (1994) have been generated. In Figure 2.4 and Figure 2.5 the results are presented for vertical and horizontal ground movement.

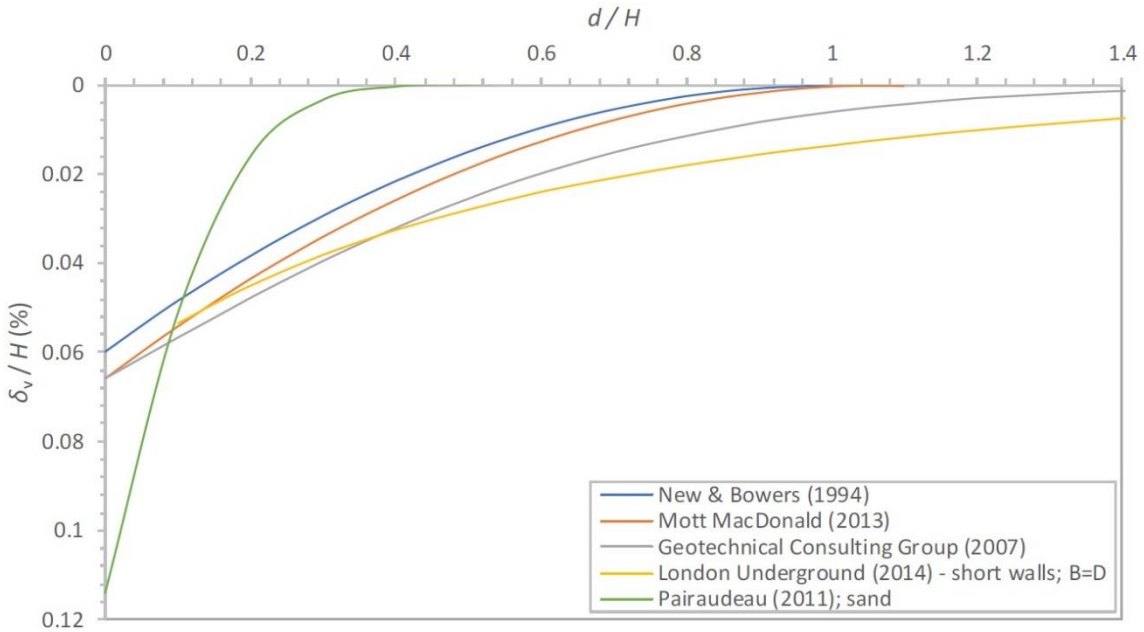

Figure 2.4 Vertical ground movement predictions for Heathrow Express Trial Tunnel shaft (J. Newhouse, 2017)

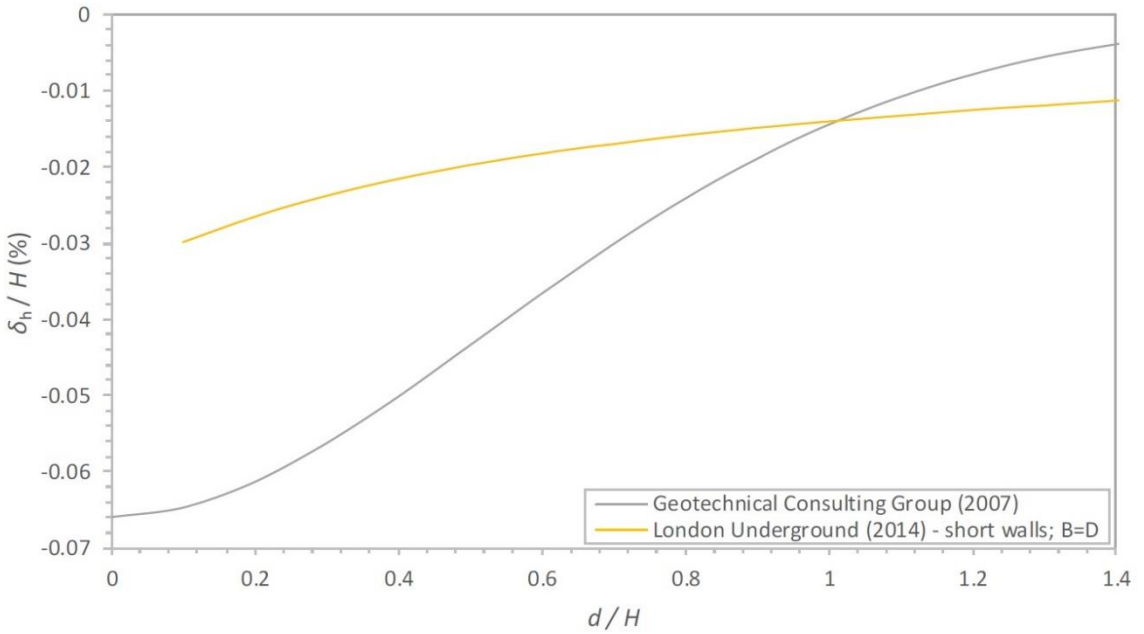

Figure 2.5 Horizontal ground movement predictions for Heathrow Express Trial Tunnel shaft (J. Newhouse, 2017)

2.2.4.7 Joseph Newhouse (2017)

Joseph Newhouse (2017) adopts the formula of GCG (2007), Equation 2.5, and two normalised parameters, α (Equation 2.7) and R (Equation 2.8), defining the maximum vertical movement normalized by excavation depth and the extent of the settlement trough normalized by excavation depth respectively. He was able to compare most of case studies regarding the settlement due to circular shaft excavation in stiff clays.

Newhouse (2017) presented several case studies (Table 2.4), primarily located in London. The table includes details of each shaft construction method, dimensions and ground movement, with its corresponding parameters, α and R. These values are plotted against the diameter normalised by excavation depth, H, in Figure 2.6 and Figure 2.7, and α against the shaft internal diameter, D, in Figure 2.8.

Figure 2.8 considers the shaft construction method (installation of the wall prior to excavation and installation and excavation concurrent), which excavation before support shafts affects more on vertical ground movement than support before excavation shafts with larger diameter.

Considering separately the two construction methods, the values α and R are bigger for shafts of greater diameter and greater diameter normalised by excavation depth (Figure 2.6, Figure 2.7 and Figure 2.8). For a common diameter, or normalised diameter, shafts where installation occurs before to excavation show the smallest values of α. Shafts where installation occurs during the excavation show the greatest value of α. Shafts where the upper half is constructed before the excavation and the lower half during the excavation lie between the two extremes.

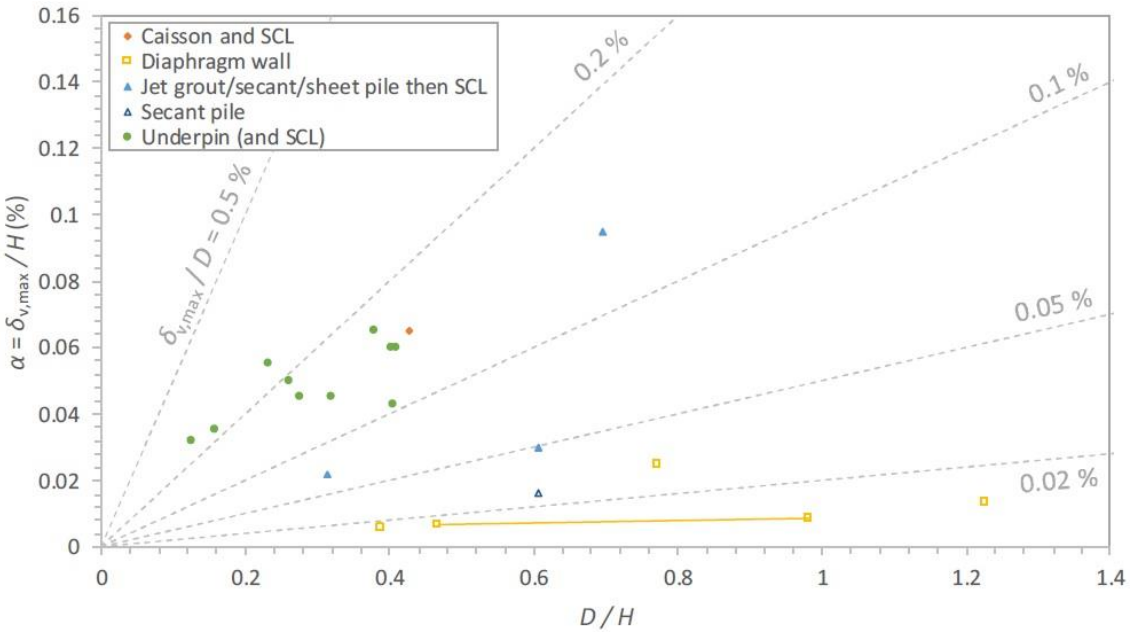

Figure 2.6 Vertical ground movement against normalised diameter due to circular shaft excavation (J. Newhouse, 2017)

Construction method	Shaft	Wall depth, H (m)	Primary lining wall thickness (m)	Excavation depth (m)	Internal diameter, D (m)	D/H (-)	$\alpha = \delta_{v,max}/H$ (%)	R = E/H (-)
Caisson and SCL	London Power Tunnels - Wandsworth	35	-	35 (23 m Caisson, 12 m SCL)	15	0.43	0.065	0.9
Diaphragm wall	Crossrail – Cambridge Heath Shaft	40	1.2	32 (23)	28.2	1.23	0.013	-
	Crossrail – Limmo Peninsula Main Shaft	55	1.2	44.3 (39.1[1])	30.2	0.68	0.025	0.8
	Lee Tunnel – Abbey Mills Shaft F	84	1.2	71	27.6	0.39	0.006	-
	Muashino (Japan)	98	1.2	28.7	28.2	0.98	0.009	-
				60.3	28.2	0.47	0.008	0.25
Jet grout/secant/sheet pile then SCL	Confidential (Mott MacDonald, 2015a)	23	2 m (grout pile) 0.25-0.35 m (SCL)	23 (12 m Jet grout wall, 11 m SCL)	6.8 to 7.7	0.32 (taking D = 7.5 m)	0.022	-
	Confidential (Mott MacDonald, 2015a)	28	-	28 (10 m Secant pile, 18 m SCL)	17	0.61	0.03	1.25
	Crossrail – Limmo Peninsula Auxiliary Shaft	38.8	SCL 0.6 – 0.8	38.8 (16,8 m Secant pile, 22 m SCL)	27	0.7	0.095[2]	1.1
Secant Pile	Crossrail – Farringdon Shaft	33	1.2	24.7	15	0.61	0.016	-
Underpin (and SCL)	Terwillegar (Canada)	20	-	20	2.4 to 3.2	0.16 (taking D = 3.2 m)	0.035	0.55
	Heathrow Express Trial Tunnel	26	-	26	10.62	0.41	0.060	1
	London Power Tunnels – Channel Gate Road	33	-	33	12.5	0.38	0.065	0.6
	London Power Tunnels – Eade Road	39	-	39	12.5	0.32	0.045	1.2

[1] α and R values relate to an excavation depth of 39.1 m, prior to a pause (J. Newhouse, 2017)

[2] α and R values relate at the completion of the excavation depth of 38.8 m (J. Newhouse, 2017)

Construction method	Shaft	Wall depth, H (m)	Primary lining wall thickness (m)	Excavation depth (m)	Internal diameter, D (m)	D/H (-)	$\alpha = \delta_{v,max}/H$ (%)	R = E/H (-)
Underpin (and SCL)	London Power Tunnels – Earls Court	40	-	40	10.5	0.26	0.05	0.8
	London Power Tunnels - Highbury	37	-	37	15	0.41	0.043	1.15
	London Power Tunnels - St John's Wood 1	45	-	45	12.5	0.28	0.045	0.65
	London Power Tunnels - St John's Wood 2	47	-	47	6 to 10	0.13 (taking D = 6 m)	0.032	0.5
	London Power Tunnels – St Pancrass	45	-	45	10.5	0.23	0.055	0.75
	London Power Tunnels – Willesden	31	-	31	12.5	0.4	0.06	0.45

Table 2.4 Cases studies of ground movement due to circular shaft construction

(Schwamb, 2014; Mott MacDonld, 2013; McNicoll, 2013; Faustin et al., 2017; Wong & Kaiser, 1988; Deane & Basset and New & Bowers, 1995; and J. Newhouse, 2017)

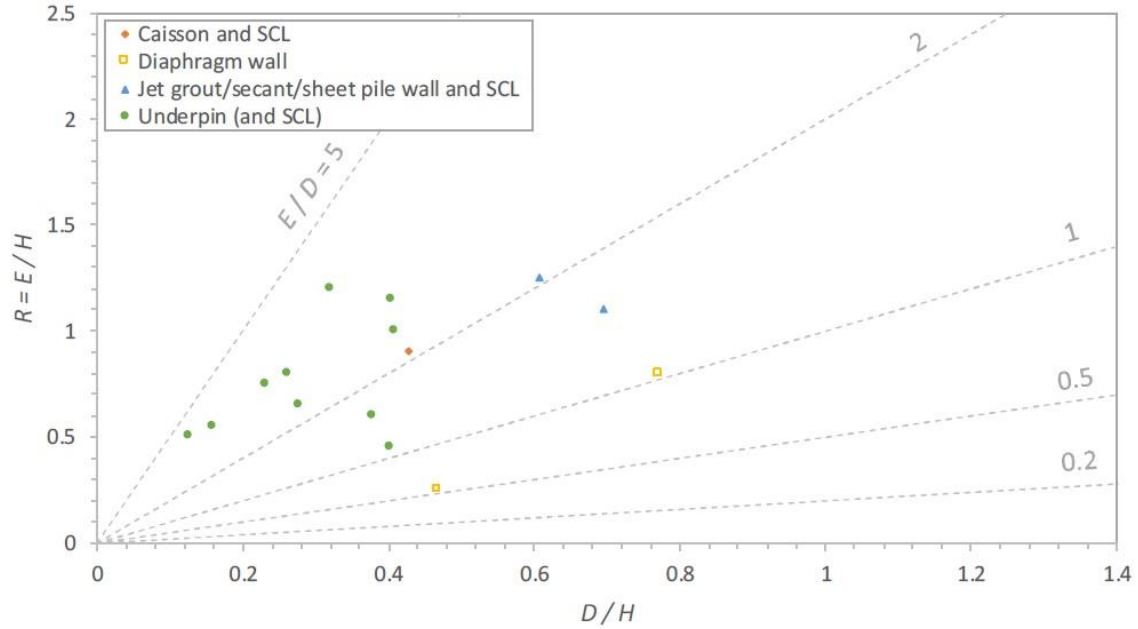

Figure 2.7 Settlement trough extent against normalised diameter due to circular shaft excavation (J. Newhouse, 2017)

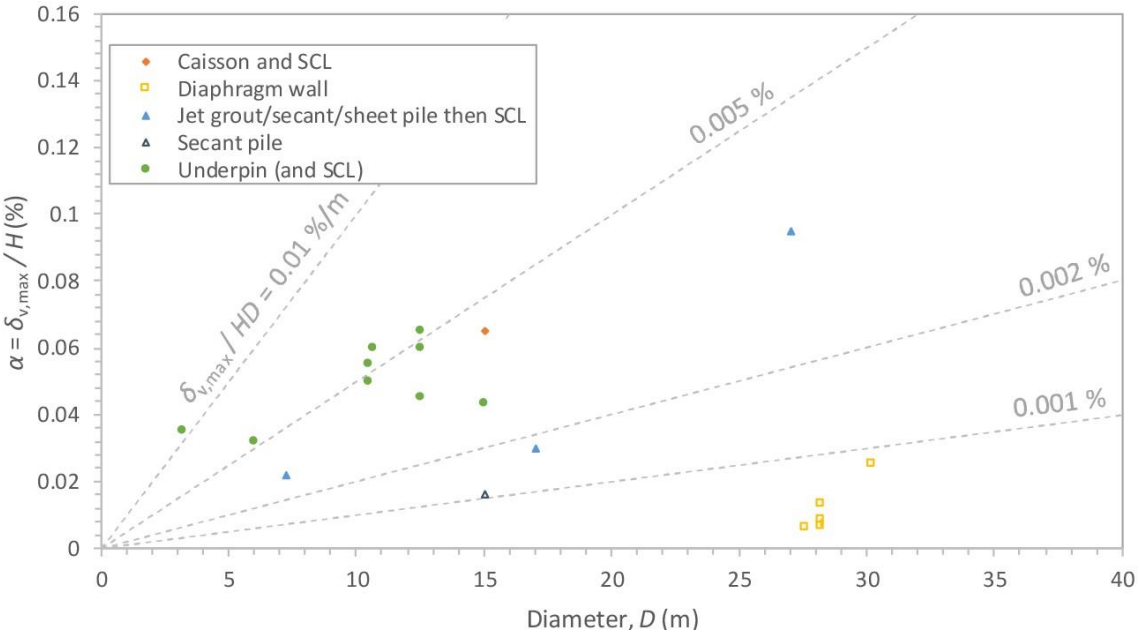

Figure 2.8 Vertical ground movement against diameter due to circular shaft excavation (J. Newhouse, 2017)

The comparison of all the case studies of vertical ground movement due to shaft excavation in stiff clays represents the most unification of shaft-induced ground movement data in the literature to date and foregrounds the importance of considering the shaft construction method. This subsequently allows for underlying trends due to shaft geometry to be examined. These trends would not be evident without the consideration of construction method and for many types of shaft would make the designer at risk of over predicting ground movement.

Joseph Newhouse (2017) studied the settlement due to shaft excavation of the Crossrail infrastructure, located on Limmo Peninsula Tunnelling Site in the London Borough of Newham, comparing the real data measured on the field and the formula proposed by GCG (2007). This

settlement was calculated as the subtraction between the total displacement observed and the ground movement due to dewatering, presenting a new methodology to calculate these displacements. Being Limmo Peninsula Tunnelling Site study the only case of ground movement due to changes in groundwater regime in the context of shaft excavation.

The numerical model of ground movement due to shaft excavation and dewatering of the Main Shaft and the Auxiliary Shaft at Limmo Peninsula Tunnelling Site is presented on Chapter 5.

3 Governing equations and constitutive models

3.1 Introduction

From a mathematical point of view, the constitutive model is the relation between the kinetic quantities and external stimuli. Wherein, the motion of a given body can be calculated with the constitutive equation, the boundary conditions and the external stimuli.

3.2 Governing differential equations

Considering a given part of the continuum occupies a given volume, Ω_0, in an arbitrary initial instant of time, t_0, and a volume, Ω_t, in any instant of time t. The initial configuration or the undeformed configuration is the initial state of the continuum, where the domain volume represents the state after has experienced deformation. In Figure 3.1 the initial and deformed configuration of the continuum are presented.

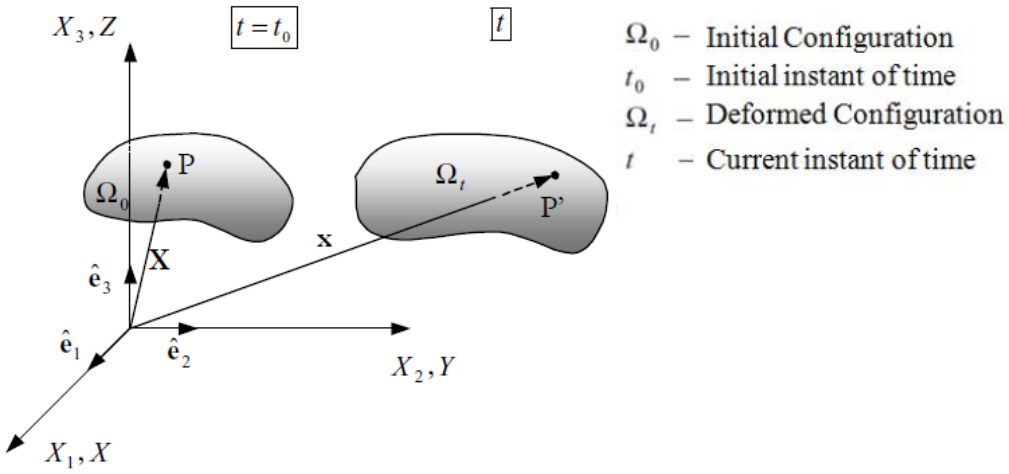

Figure 3.1 Initial and deformed configuration of a continuum (Oliver, et al., 2000)

The material points in the current configuration are denoted by the vector **X** of coordinates and the current position is denoted by the vector $\mathbf{x} = \varphi(\mathbf{X}, t)$. The vector $\mathbf{u}(\mathbf{x}, t) = \mathbf{x}(t) - \mathbf{x}(t_0)$ is the displacement and the velocity is denoted by $\mathbf{v}(\mathbf{x}, t)$; $\boldsymbol{\sigma}(\mathbf{x}, t)$ is defined the Cauchy Stress tensor in the position **x** and time t. The mass density for the position **x** in the t instant of time is denoted by $\rho(\mathbf{x}, t)$. The Cauchy Stress tensor in scientific coordinates is presented in Figure 3.2.

$$\boldsymbol{\sigma} \equiv \begin{bmatrix} \sigma_{11} & \sigma_{12} & \sigma_{13} \\ \sigma_{21} & \sigma_{22} & \sigma_{23} \\ \sigma_{31} & \sigma_{32} & \sigma_{33} \end{bmatrix}$$

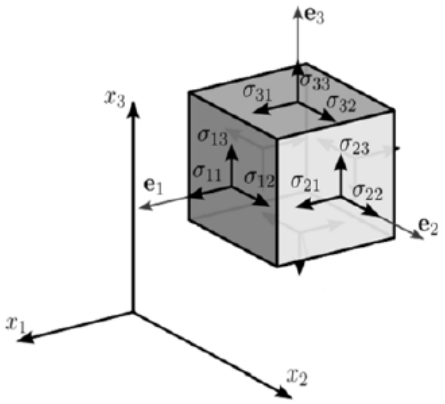

Figure 3.2 Cauchy Stress Tensor (Oliver, et al., 2000)

3.2.1 Conservation of mass

The material time derivative of the mass be zero for any region of a material volume is required for the mass conservation. The continuity equation (local or differential spatial form of mass conservation principle) is presented in Equation 3.1 and the global spatial form in Equation 3.2.

$$\frac{d\rho}{dt} + \rho \nabla \cdot \mathbf{v} = 0 \tag{3.1}$$

$$\frac{d}{dt} \int_{V_t} \rho \, dV = \int_{V_t} \left(\frac{d\rho}{dt} + \rho \nabla \cdot \mathbf{v} \right) dV = 0 \tag{3.2}$$

3.2.2 Linear momentum balance

The time-variation of the linear momentum of a material volume is equal to the resultant force acting on the material volume. The linear momentum is conserved, if the body is in equilibrium. The global spatial form for the linear momentum balance is presented in Equation 3.3. wherein the local spatial form for the linear momentum balance (Cauchy's Equation of Motion) is presented in Equation 3.4, the **b** vector is the body forces vector.

$$\int_V (\nabla \cdot \boldsymbol{\sigma} + \rho \, \mathbf{b}) dV = \int_V \rho \frac{d\mathbf{v}}{dt} dV \tag{3.3}$$

$$\nabla \cdot \boldsymbol{\sigma} + \rho \mathbf{b} = \rho \frac{d\mathbf{v}}{dt} = \rho \, \mathbf{a} \tag{3.4}$$

To relate the stresses of the material with the strains and providing the problem with boundary and initial conditions needs the mathematical formulation constitutive laws. The following sections are presented the constitutive relation, the boundary conditions and the initial conditions.

3.2.3 Constitutive relation

The constitutive relation, Equation 3.5, can be written with respect to the stresses and strains by means of the constitutive tensor $\mathbb{C}$.

$$\boldsymbol{\sigma}(\mathbf{x}, t) = \mathbb{C} : \boldsymbol{\varepsilon}(\mathbf{x}, t) \tag{3.5}$$

The Hooke's law is applied for special case of an isotropic linear elastic material. In case of non-lineal, anisotropic materials the constitutive tensor a difficult expression which generally evolves time.

In Equation 3.6, the constitutive relation in fluids is presented, wherein the p is the pressure of the fluid.

$$\boldsymbol{\sigma} = -p\mathbf{1} \tag{3.6}$$

3.2.4 Boundary conditions

The boundary conditions in space affect the unknown's spatial arguments and are applied on the contour, $\partial\Omega = \Gamma$, of the continuum medium.

- Prescribed displacements on Γ_u
$$\mathbf{u}(\mathbf{x},t) = \mathbf{u}^*(\mathbf{x},t) \tag{3.7}$$
- Prescribed tractions on Γ_σ
$$\boldsymbol{\sigma}(\mathbf{x},t)\cdot\mathbf{n} = \mathbf{t}^*(\mathbf{x},t) \tag{3.8}$$

In Figure 3.3 are presented the boundary conditions in space. Wherein, there is a third group of boundary conditions where both, displacements and tractions are prescribed on Γ_u and Γ_σ.

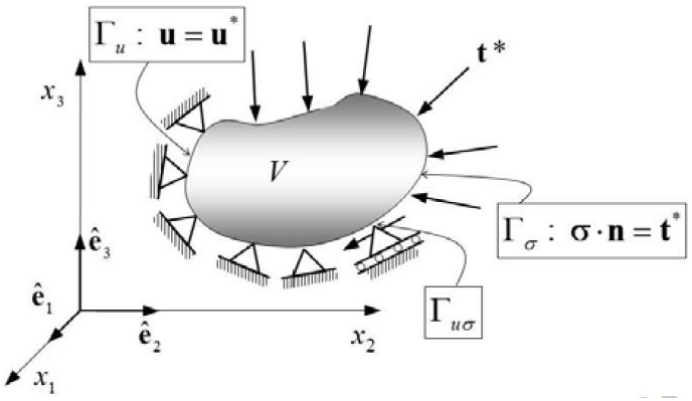

Figure 3.3 Boundary conditions in space (Oliver, et al., 2000)

However, the boundary conditions in fluids are divided by two:

- Prescribed velocity on Γ_v
$$\mathbf{v}(\mathbf{x},t) = \bar{\mathbf{v}}(\mathbf{x},t) \tag{3.9}$$
- Prescribed pressure on Γ_σ
$$\mathbf{t}(\mathbf{x},t) = \boldsymbol{\sigma}\cdot\mathbf{n} = \mathbf{t}^*(\mathbf{x},t) \tag{3.10}$$

Vector **n** is the normal vector to the continuum. Where the prescribed pressure on a free surface is the atmosphere pressure.

3.2.5 Initial conditions

The initial conditions (boundary conditions in time) affect the time argument of the unknowns and generally they are known values at time zero, t_0. The initial displacement is presented in Equation. 3.11, the initial velocity of the momentum is presented in Equation 3.12 and the initial fluid pressure is presented in Equation 3.13.

$$\mathbf{u}(\mathbf{x},0)=\mathbf{0} \tag{3.11}$$

$$\left.\frac{\partial \mathbf{u}(\mathbf{x},t)}{\partial t}\right|_{t=0} \overset{not}{=} \dot{u}(\mathbf{x},0)=\mathbf{v}_0(\mathbf{x}) \tag{3.12}$$

$$\mathbf{t}(\mathbf{x},0)=\mathbf{t}_0(\mathbf{x}) \tag{3.13}$$

3.3 Discretization of the governing equations

The continuum is modelled by diving it into elements, wherein contains a constant in time mass. These elements are described by a number of particles N_p, p =1, 2, 3,…. In Equation 3.14, it can be observed the mass density is defined as the summation of discrete masses, where $\delta(\mathbf{x}–\mathbf{x}_p(t))$ is the Dirac delta function with dimension of inverse of volume.

$$\rho(\mathbf{x},t)=\sum_{p=1}^{N_p} m_p \delta\left(\mathbf{x}-\mathbf{x}_p(t)\right) \tag{3.14}$$

The weak form of the Continuity Equation are presented in Equation 3.15, based in the standard fashion of FEM.

$$\int_{\Omega_t} \rho w_i \, \mathbf{a} \, d\Omega = -\int_{\Omega_t} \rho \mathbf{S}:\nabla w_i \, d\Omega + \int_{\Gamma_t} w_i \cdot \boldsymbol{\tau} d\Gamma + \int_{\Omega_t} \rho w_i \cdot \mathbf{b} d\Omega \tag{3.15}$$

$$\mathbf{v}=\sum_{i=1}^{N_n} \mathbf{v}_i(t) N_i(\mathbf{x}) \tag{3.16}$$

$$w_i = N_i \tag{3.17}$$

By using the expression of the mass density, Equation 3.14, in the continuity equation weak form (Equation 3.15) obtain a discrete equation of linear momentum conservation and the integrals are transformed into summations. In Equation 3.18 it can be observe the integral form of the inertial forces.

$$\int_{\Omega_t} \rho w_i \, \mathbf{a} \, d\Omega = \sum_{j=1}^{N_n} \sum_{p=1}^{N_p} m_p \; N_i(\mathbf{x}) N_j(\mathbf{x}) \mathbf{a}_j(t) \tag{3.18}$$

The Continuity Equation weak form and since w_i are arbitrary except the components of displacement are prescribed becomes in Equation 3.19.

$$\sum_{j=1}^{N_n} m_{ij}^k \mathbf{a}_j^k = \mathbf{f}_i^{\text{int},k} + \mathbf{f}_i^{\text{ext},k}, \qquad i = 1,\ldots,N_n \tag{3.19}$$

3.4 Deformation theory

The static equilibrium of a continuum can be formulated as in Equation 3.20. This equation describes the derivatives of the six stress components, assembled in the vector $\underline{\sigma}$, to the three components of the body forces assembled in vector $\underline{b}$. Being the transpose of a differential operator as $\underline{\underline{L}}^T$.

$$\underline{\underline{L}}^T \underline{\sigma} + \underline{b} = \underline{0} \tag{3.20}$$

As described in Section 3.3, it can be reformulated as weak form to Galerkin's variation principle, Equation 3.21.

$$\int \delta \underline{u}^T \left(\underline{\underline{L}}^T \underline{\sigma} + \underline{b} \right) dV = 0 \tag{3.21}$$

And after the discretization the static equilibrium equation can be write as:

$$\int \underline{\underline{B}}^T \Delta \underline{\sigma} \, dV = \int \underline{\underline{N}}^T \underline{b}^i \, dV + \int \underline{\underline{N}}^T \underline{t}^i \, dS - \int \underline{\underline{B}}^T \underline{\sigma}^{i-1} \, dV \tag{3.22}$$

3.4.1 Implicit integration of differential plasticity models

According to Plaxis Manual, when using differential plasticity models the stress increments, according to the integration of the stress rates Equation 3.23, can be written as Equation 3.24

$$\underline{\sigma}^i = \underline{\sigma}^{i-1} + \Delta \underline{\sigma} \tag{3.23}$$

$$\Delta \underline{\sigma} = \underline{\underline{D}}^e \left(\Delta \underline{\varepsilon} - \Delta \underline{\varepsilon}^p \right) \tag{3.24}$$

$\underline{\underline{D}}^e$ is the elastic material matrix for the current stress increment. For elastic material behaviour, the plastic strain increment $\Delta \underline{\varepsilon}^p$ is zero. The plastic strain increment can be written in Equation 3.25, for plastic material behaviour proposed by Vermeer (1979).

$$\Delta \underline{\varepsilon}^p = \Delta \lambda \left[(1 - \omega) \left(\frac{\partial g}{\partial \underline{\sigma}} \right)^{i-1} + \omega \left(\frac{\partial g}{\partial \underline{\sigma}} \right)^{i} \right] \tag{3.25}$$

In this relation, $\Delta\lambda$ is the increment of the plastic multiplier and ω is a parameter that indicates the type of time integration. For $\omega = 0$ the integration is called explicit and for $\omega = 1$ the integration is called implicit.

Therefore, for $\omega = 1$ Equation 3.22 reduces to:

$$\Delta \underline{\varepsilon}^p = \Delta \lambda \left(\frac{\partial g}{\partial \underline{\sigma}} \right)^{i} \tag{3.26}$$

Substitution of Equation 3.26 into Equation 3.21 and successively into Equation 3.23 gives:

$$\underline{\sigma}^i = \underline{\sigma}^{tr} - \Delta \lambda \underline{\underline{D}}^e \left(\frac{\partial g}{\partial \underline{\sigma}} \right)^{i} \quad \text{with:} \quad \underline{\sigma}^{tr} = \underline{\sigma}^{i-1} + \underline{\underline{D}}^e \Delta \underline{\varepsilon} \tag{3.27}$$

The increment of the plastic multiplier $\Delta\lambda$ as used in Equation 3.27, can be solved from the condition that the new stress state has to satisfy the yield condition:

$$f\left(\underline{\sigma}^i \right) = 0 \tag{3.28}$$

For perfectly-plastic and linear hardening models the increment of the plastic multiplier can be written as:

$$\Delta \lambda = \frac{f\left(\underline{\sigma}^{tr} \right)}{d + h} \tag{3.29}$$

where:

$$d = \left(\frac{\partial f}{\partial \underline{\sigma}}\right)^{\underline{\sigma}^{tr}} \underline{\underline{D}}^{e} \left(\frac{\partial g}{\partial \underline{\sigma}}\right)^{i} \tag{3.30}$$

The symbol *h* denotes the hardening parameter, which for perfectly-plastic models is zero and constant for linear hardening model. In the latter case the new stress state can be formulated as:

$$\underline{\sigma}^{i} = \underline{\sigma}^{tr} - \frac{\langle}{f}(\underline{\sigma}^{tr})\rangle d + h\underline{\underline{D}}^{e}\left(\frac{\partial g}{\partial \underline{\sigma}}\right)^{i} \tag{3.31}$$

The $\langle\rangle$-brackets are referred to as McCauley brackets which have the next convention:

$$\langle x\rangle = 0 \quad \text{for:} \quad x \leq 0 \quad \text{and:} \quad \langle x\rangle = x \quad \text{for:} \quad x > 0$$

For non-linear hardening models the increment of the plastic multiplier is obtained using a Newton-type iterative procedure with convergence control.

3.5 Groundwater flow theory

The flow in porous medium can be described by the Darcy's law expressed, in Equation 3.32, in three dimensions. Where, $\underline{q}$, $\underline{\underline{k}}$, $\underline{g}$ and ρ_w are the specific discharge (fluid velocity) the tensor of permeability, the acceleration vector due to gravity and the density of water, respectively. $\underline{\nabla} p_w$ is the gradient of the water pore pressure which causes groundwater flow.

$$\underline{q} = \frac{\underline{\underline{k}}}{\rho_w g}\left(\underline{\nabla} p_w + \rho_w \underline{g}\right) \tag{3.32}$$

In unsaturated soils the coefficient of permeability $\underline{\underline{k}}$ can be related to the soil saturation in Equation 3.33. where, k_{rel} is the ratio of the permeability at given saturation to the permeability in saturated state k^{sat}.

$$\underline{\underline{k}} = k_{rel}\,\underline{\underline{k}}^{sat} \tag{3.33}$$

The continuity equation is described in Equation 3.34 (Song, 1990), the water outflow from the volume is equal to the changes in the mass concentration. Where, the parameters *S* and *n* are the degree of saturation of the soil and the porosity, respectively.

$$\nabla^{T} \cdot (\rho_w \underline{q}) = -\frac{\partial}{\partial t}(\rho_w n S) \tag{3.34}$$

In Equation 3.35, the continuity equation for the transient ground water flow is described as the displacements of solid particles are neglected.

$$\nabla^{T} \cdot (\rho_w \underline{q}) - n\left(\frac{S}{K_w} - \frac{\partial S}{\partial p_w}\right)\frac{\partial p_w}{\partial t} = 0 \tag{3.35}$$

And for steady state flow $\left({}^{\partial p_w}/_{\partial t} = 0\right)$ the continuity condition in Equation 3.36. it expresses that there is no net inflow or outflow in an elementary area, as illustrated in Figure 3.4.

$$\nabla^{T} \cdot (\rho_w \underline{q}) = 0 \tag{3.36}$$

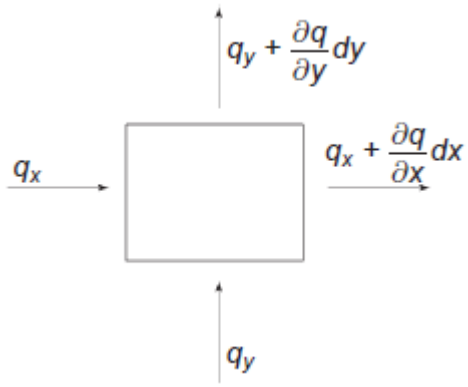

Figure 3.4 illustration of continuity condition (Plaxis, 2018)

According to the discretization of the governing equations in Section 3.3, applying the Galerkin approach to the continuity equation and the prescribed boundary conditions, it can be described in Equation 3.37.

$$-\underline{\underline{H}}\,\underline{p_w}_n - \underline{\underline{S}}\frac{d\underline{p_w}_n}{dt} = \underline{q}_p \tag{3.37}$$

Where $\underline{\underline{H}}$, $\underline{\underline{S}}$ and $\underline{q}_p$ are the permeability matrix (Equation 3.38), the compressibility matrix (Equation 3.39) and the prescribed recharges that are given by the boundary conditions (Equation 3.40), respectively. $\bar{q}$ is the outflow prescribed flux on the boundary. The term $d\Gamma$ indicates a surface integral.

$$\underline{\underline{H}} = \int (\nabla \underline{\underline{N}})^T \frac{k_{rel}}{\gamma_w} \underline{\underline{k}}^{sat} (\nabla \underline{\underline{N}})\, dV \tag{3.38}$$

$$\underline{\underline{S}} = \int \underline{\underline{N}}^T \left(\frac{nS}{K_w} - n\frac{\partial S}{\partial p_w} \right) \underline{\underline{N}}\, dV \tag{3.39}$$

$$\underline{q}_p = \int (\nabla \underline{\underline{N}})^T \frac{k_{rel}}{\gamma_w} \underline{\underline{k}}^{sat} \rho_w \underline{g}\, dV - \int \underline{\underline{N}}^T \bar{q}\, d\Gamma \tag{3.40}$$

Due to the unsaturated zone the equations described above are non-linear and to solve iteratively the system of equations use a Picard scheme, Equation 3.41. The linear set is solved with incremental form using an implicit time. The parameter α is the time integration coefficient. In general, the integration coefficient α can take values from 0 to 1.

$$-\left(\alpha \Delta t \underline{\underline{H}} + \underline{\underline{S}}\right) \Delta \underline{p_w}_n = \Delta t \underline{\underline{H}}\, \underline{p_w}_{n0} + \Delta t \underline{q}_p \tag{3.41}$$

For steady state flow the governing equation is:

$$-\alpha \underline{\underline{H}}\, \Delta \underline{p_w}_n = \underline{\underline{H}}\, \underline{p_w}_{n0} + \underline{q}_p \tag{3.42}$$

3.6 Mohr-Coulomb strain softening law

The theory was presented by Mohr (1886) for rupture in soils that contended that a material fails of a critical combination of normal stress and shearing stress. Thus, the functional relationship between normal stress and shear stress on a failure plane can be expressed in the following form:

$$\tau_f = f(\sigma) \tag{3.43}$$

The failure envelope defined by Equation 3.43 is a curved line. For most soil mechanics problems, it is sufficient to approximate the shear stress on the failure plane as a linear function of the normal stress (Coulomb, 1776). This linear function can be written as:

$$\tau_f = c + \sigma \tan \phi \tag{3.44}$$

Where c, ϕ, σ and τ_f are the cohesion, the angle of internal friction, the normal stress on the failure plane and the shear strength respectively.

In saturated soil, the total normal stress at a point is the sum of the effective stress (σ') and pore water (u), or (assuming compressions positive)

$$\sigma = \sigma' + u \tag{3.45}$$

The effective stress σ' is carried by the soil solids. The Mohr-Coulomb failure criterion, expressed in terms of effective stress, will be of the form

$$\tau_f = c' + \sigma' \tan \phi' \tag{3.46}$$

Where c' is the cohesion and the ϕ' the friction angle, based on effective stress.

Thus, Equation 3.44 and Equation 3.46 are expression of shear strength based on total stress and effective stress, respectively. The value of c' for sand and inorganic silt is 0. For normally consolidated clays, c' can be approximated at 0. Overconsolidated clays have values greater than 0.

The significance of Equation 3.46 can be explained by referring to Figure 3.5, which shows an elemental soil mass. Let the effective normal stress and the shear stress on the plane *ab* be σ' and τ, respectively, in Figure 3.5a. If the magnitudes of normal and shear stress in this plane are such that they plot as point A in Figure 3.5b, shear failure will not occur along the plane. If the effective normal stress and the shear stress on plane *ab* plot as point *B* (which falls on the failure envelope), shear failure will occur along the plane. A state of stress on a plane represented by point *C* cannot exist, because it plots above the failure envelope, and shear failure in a soil would have occurred already

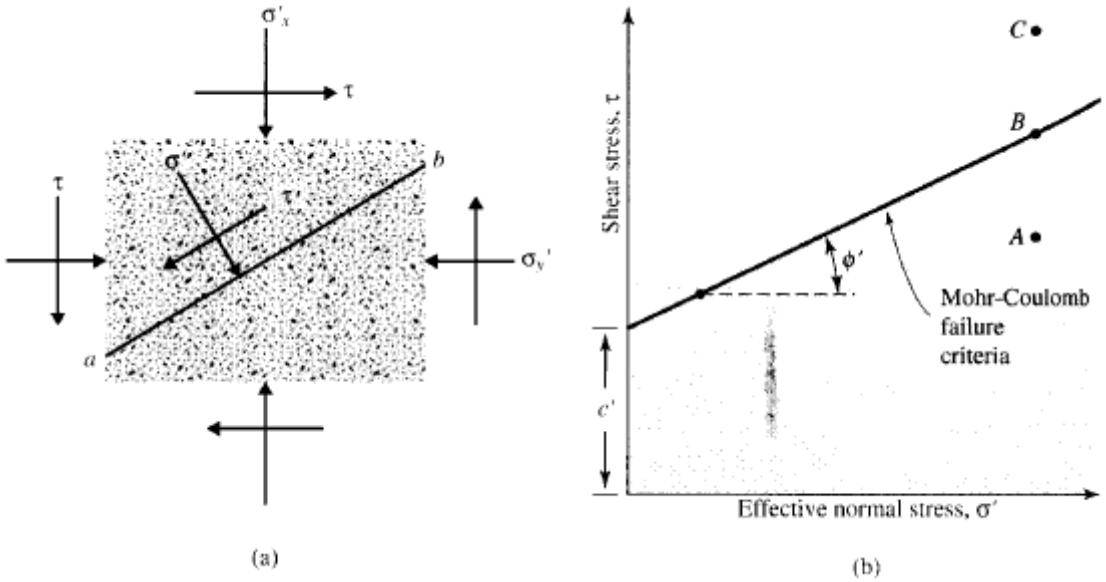

Figure 3.5 Mohr-Coulomb failure criterion (Braja, et al., 1994)

3.7 Hardening Soil models

In general, a precise deformation analysis requires the application of advanced constitutive models which approximate the stress strain relation more accurately than simple linear-elastic. On the other hand, to study the ULS (Ultimate Limit State) behaviour for bearing capacity or slope stability may be limited to basic models such as Mohr-Coulomb model.

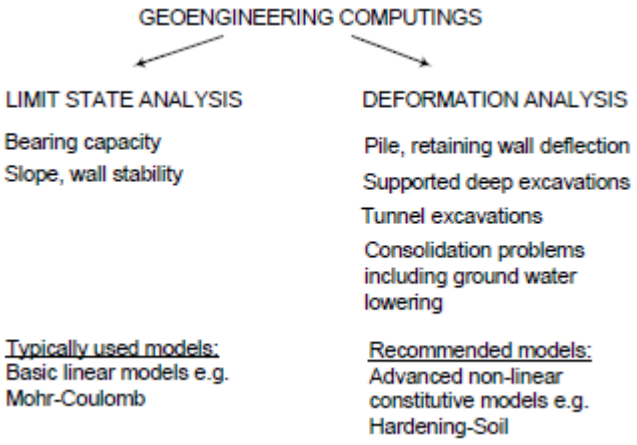

Figure 3.6 General types of geoengineering computing's (Obrzud, et al., 2010)

The dashed line presented in Figure 3.7, the model choice may be used but not recommended in terms of quality results; the solid lines, can be applied and the green boxes are recommended.

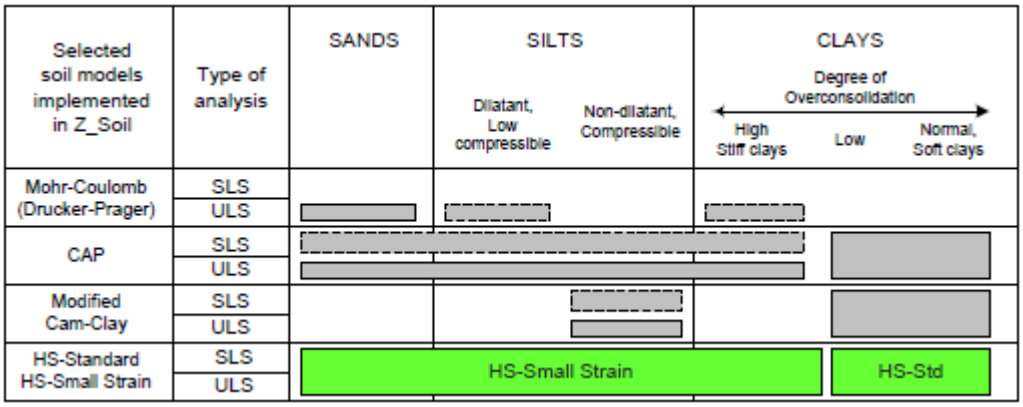

Figure 3.7 Recommendations for the model choice for soil type and types of analysis (Obrzud, et al., 2010)

3.7.1 Hardening Soil model

The Hardening Soil model (HS-Standard) was designed in order to reproduce basic macroscopic phenomena exhibited by soils such as:

- Densification
- Stress dependent stiffness
- Soil stress history
- Plastic yielding
- Dilatancy

This model is derived from the hyperbolic model (Duncan, et al., 1970). It is adapted to all types of soil. Two mechanisms with isotropic hardening controlling the volumetric and deviatoric strains describe the yield surface, Figure 3.8. the input parameters are:

- The resistance parameters ϕ, c (similarly to the Mohr-Coulomb model) and ψ (dilatancy angle).
- The stiffness of the soil is defined by parameters E_{50}^{ref} (secant stiffness in standard drained triaxial test), E_{oed}^{ref} (tangent stiffness for primary oedometer loading) governs the volumetric behaviour and E_{ur}^{ref} the unloading-reloading modulus.

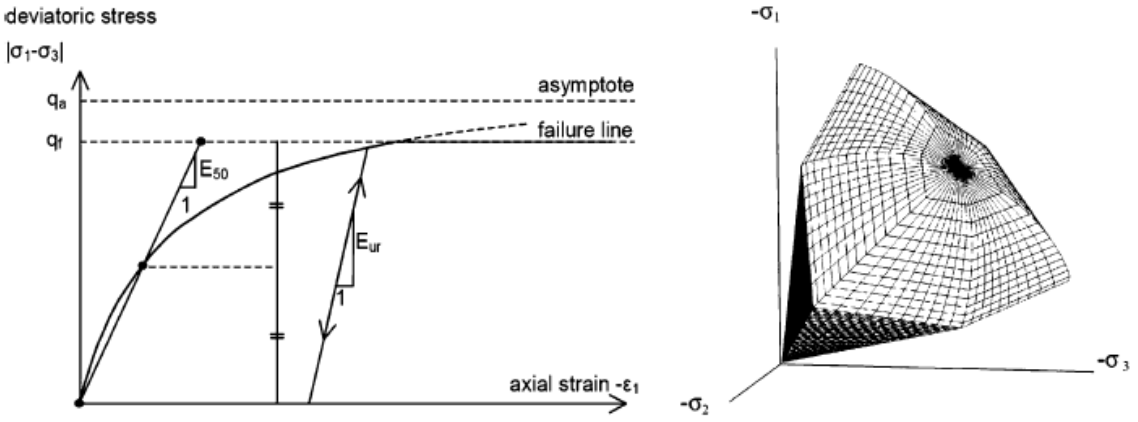

Figure 3.8 HS model, stress-strain relationships and yield surface (Schanz, et al., 1999)

3.7.2 HS Small Strain

The HS Small model is an extension of the Hardening Soil model, where all the features of that model are therefore included in HS Small model.

Infinitesimal strain theory (called Small Strain) is based on two hypotheses:

1) Displacements are very small compared to the typical dimensions in the continuous medium:
$$\|\mathbf{u}\| << \|\mathbf{X}\| \tag{3.47}$$
2) Displacement gradients are very small (infinitesimal).
$$\left|\frac{\partial u_i}{\partial x_j}\right| << 1, \quad \forall i, j \in \{1,2,3\} \tag{3.48}$$

Many authors have studied the behaviour of soils using high precision triaxial tests. They obtained a reversible behaviour and high stiffness for strains less than 10^{-5} and showed that the shear modulus was constant under very small-strain (strains between 10^{-6} and 10^{-5}).

In fact, in Plaxis Software, only two additional parameters are needed to describe the stiffness behaviour at small strains. The initial or very small-strain shear modulus G_0^{ref} and the shear strain level $\gamma_{0.7}$ at which the secant shear modulus G is reduced to 70% of G_0^{ref}.

$$\frac{G_s}{G_0} = \frac{1}{1 + \frac{3}{7} \cdot \left|\frac{\gamma}{\gamma_{0.7}}\right|} \tag{3.49}$$

Figure 3.9 presents an example of the calibration of the stress-strain that has been obtained for an overconsolidated clay during the execution of Terminal 5 of Heathrow airport. It shows the behaviour between the three model predictions (Mohr-Coulomb, Hardening Soil and HS Small Strain) and a drained test data. Figure 3.10 explains the degradation of the Young modulus with the axial strain level. The stress paths followed in this numerical analysis are given by Gasparre (2005) (The experimental data in this paper represent the tests 26DC and 28DC).

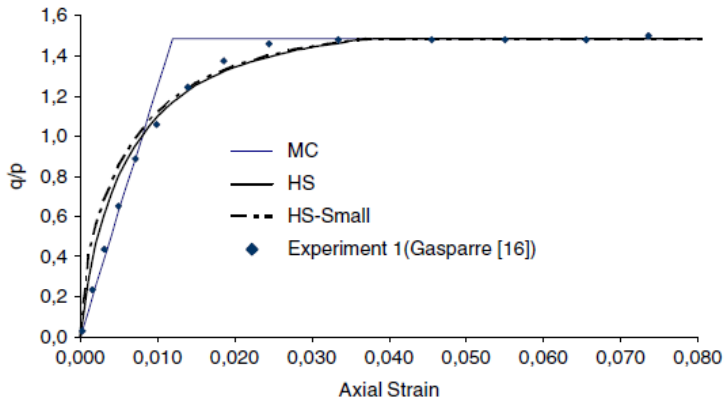

Figure 3.9 Stress-strain curves (comparison between model predictions and drained test data) (Hejazi, et al., 2008)

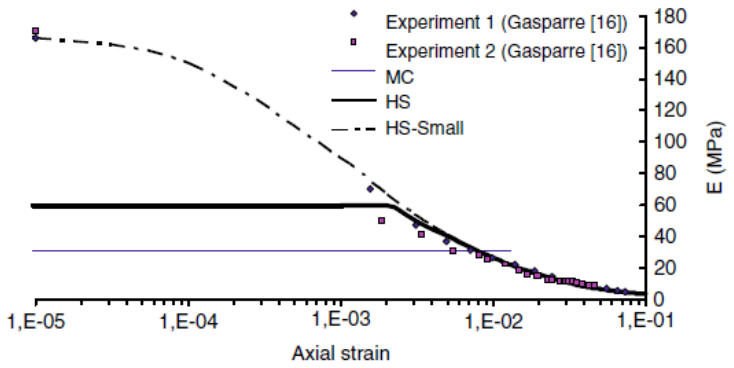

Figure 3.10 Stiffness-strain curves (comparison between model predictions and drained test data) (Hejazi, et al., 2008)

4 Limmo Peninsula Tunnelling Site case study

In this Chapter the Limo Peninsula shaft construction case study is summarised based in all the information given in Joseph Newhouse (2017). Information about the site including geological and groundwater conditions is given. The structural overview and full construction sequence are also presented including the dewatering timeline achieved for construction of the circular shafts.

4.1 Site overview

The Limmo Peninsula Tunnelling Site excavation belongs to the new railway that will become known as Elizabeth line. It comprises a new railway running from Maidenhead and Heathrow in the west to Shenfield and Abbey Wood on the east across 42 km of new tunnels under London, being the Europe's largest infrastructure project set up to build by Crossrail LTD. Limmo Peninsula Tunnelling Site is located in the London Borough of Newham.

The excavation site is formed by two shafts; Main Shaft and Auxiliary Shaft. The function of the Main Shaft during construction is to provide a launch and service emplacement for the Tunnel Boring Machines (TBM). Nevertheless, the site also served for a long-term function to provide intervention access. The Auxiliary Shaft was constructed to allow for the assembly of the TBM below ground prior to commencing their respective bores. This Auxiliary Shaft has been backfilled afterwards.

4.2 Structural overview and construction sequence

The Main Shaft and Auxiliary Shaft have been made by different construction methods: Main Shaft involved the installation of the wall prior to excavation (Diaphragm Walls) and for the Auxiliary Shaft, the upper half was constructed also before the excavation (Steel Sheet Piles) but in the lower half, the installation and the excavation were concurrent (Sprayed Concrete Lining), respectively.

The structural details of the Limmo Peninsula Tunnelling Site Shafts are summarised in Table 4.1. The Main Shaft is designed with a 30.2 m diameter, 44.3 m deep shaft constructed using 55 m deep diaphragm walls. While the Auxiliary Shaft comprises a 27 m diameter, 38.8m deep shaft and constructed using 16.8 m of steel sheet piles the upper half and the lower 22 m were constructed using SCL.

The shafts are linked by two SCL launch adits and with two SCL foreshunt from which the bored tunnels machines were then advanced.

Shaft	Location	Construction method	Wall depth, h (m)	Primary lining wall thickness (m)	Excavation depth, (m)	Internal diameter, D (m)	D/H (-)
Main Shaft	London, UK	Diaphragm wall	55	1.2	44.3 (39.1*)	30.2	0.68
Auxiliary shaft		16.8 m Sheet pile 22 m SCL	38.8	SCL 0.6 - 0.8	38.8	27	0.7

*Depth reached before to pause in excavation

Table 4.1 Details of the Limmo Peninsula Shafts Site shafts
(Crossrail, 2016b; Crossrail ,2012b; Crossrail, 2012a and J. Newhouse, 2017)

On Table 4.2 it can be observe the key dates in the construction sequence at Limmo Peninsula Tunnelling Site Shaft. There is a pause of over four months in the excavation progress of the Main Shaft when it reaches 39.1 m depth and recommencing excavation. During this period, it took place the majority of the foreshunt and launch adit excavation producing a large ground movement affecting on the studio. Accordingly, the data corresponding to the second part of the excavation are not presented herein.

Construction Stage	Start	End	Days
Main Shaft diaphragm wall installation	10/2011	12/2011	-
Main Shaft excavation to 39.1 m	17/02/2012	23/04/2012	66
Main Shaft excavation from 39.1 m to 44.3 m	10/09/2012	14/09/2012	4
Auxiliary Shaft sheet pile installation	-	-	-
Auxiliary Shat excavation (sheet piles)	14/02/2012	13/04/2012	59
Auxiliary shaft excavation (SCL)	13/04/2012	01/06/2012	49
Foreshunt and Adit excavation	05/07/2012	26/09/2012	83

Table 4.2 Key dates of the shaft construction at Limmo Peninsula Tunnelling Site
(Faustin et al., 2017; Crossrail, 2016e; DSJV, 2012b and J. Newhouse, 2017)

4.3 Geological and groundwater overview

The Limmo Peninsula Tunnelling Site stratigraphic sequence is composed of Made Ground, Alluvium, River Terrace Deposit, London Clay, Harwich Formation, Lambeth Group, Thanet Sand and Chalk. On Figure 4.1, all the materials according to Joseph Newhouse (2017) are presented in a simplified manner. wherein it can observe a 13.5 m layer of Upper Aquifer (including Made Ground, Alluvium and River Terrace Deposit), a 30 m of Aquiclude (London Clay), a 5.5 layer of Middle Aquifer (Harwich Formation and Lambeth Group), a 4 m of Aquiclude (Lambeth Group) and the Lower Aquifer comprised by Lambeth Group, Thanet Sand and Chalk.

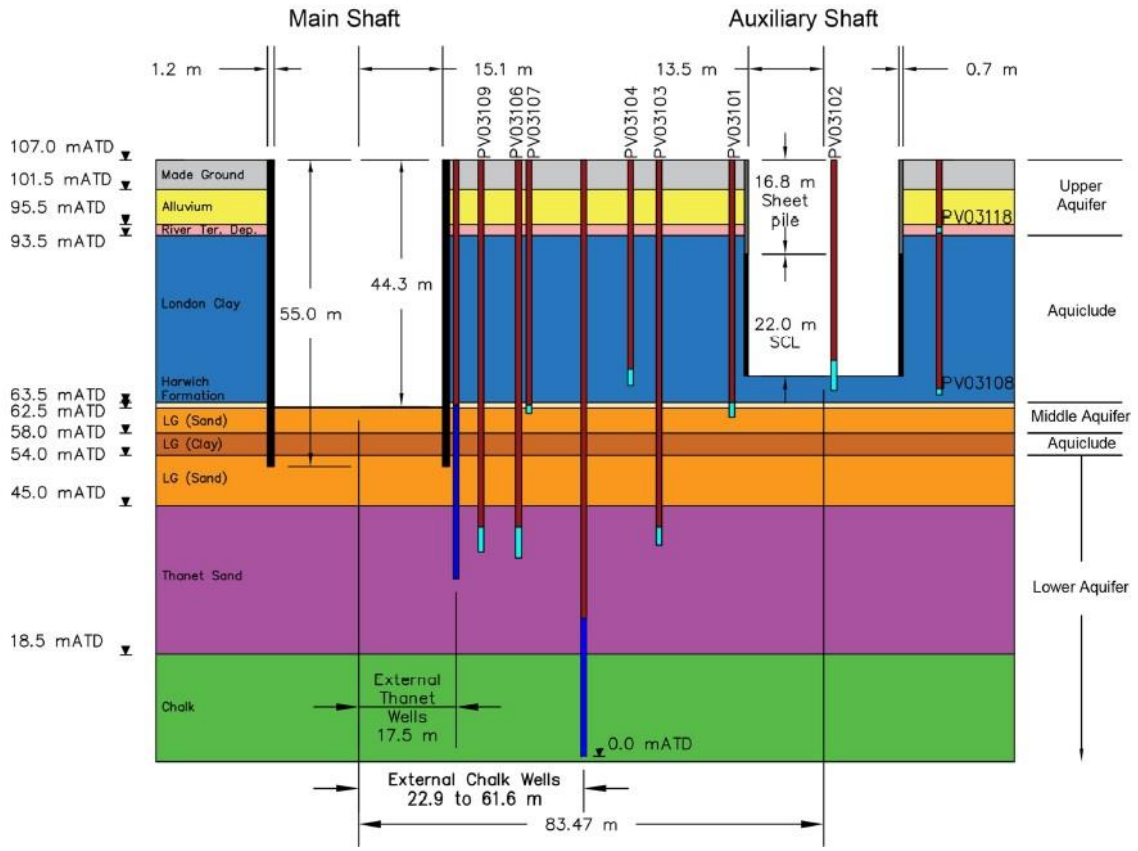

Figure 4.1 Ground model section for Limmo Peninsula Tunnelling Site, including piezometer and well dimensions and structural (J. Newhouse, 2017)

During all the excavation progress, a change of a groundwater level controlled by the two External Wells (Thanet Sand and Chalk). In Figure 4.1, it can be observed the distribution of the vibrating wire piezometric and the two External Wells. This groundwater control measures were required during the construction to maintain the face stability of excavations for SCL elements in high permeability strata and to prevent base heave failure of the shaft and tunnel excavation.

The piezometric level data collected during the shaft construction for each layer in Figure 4.2. Thus, the Lower Aquifer has a fast response to the dewatering characterized for the high permeability of those materials where the two External Wells (Thanet Sand and Chalk). The piezometric head on London Clay has a progressive behaviour, until it is reached the Auxiliary Shaft Excavation Sheet Piles End / SCL start Stage. This is due to the location of vibrating wire piezometer, which is inside the Auxiliary Shaft and the SCL excavation start, producing an outflow groundwater on the shaft base every time is excavated. The Upper Aquifer does not have any response due to the 30 m layer of Aquiclude formed of London Clay, characterized for a low permeability.

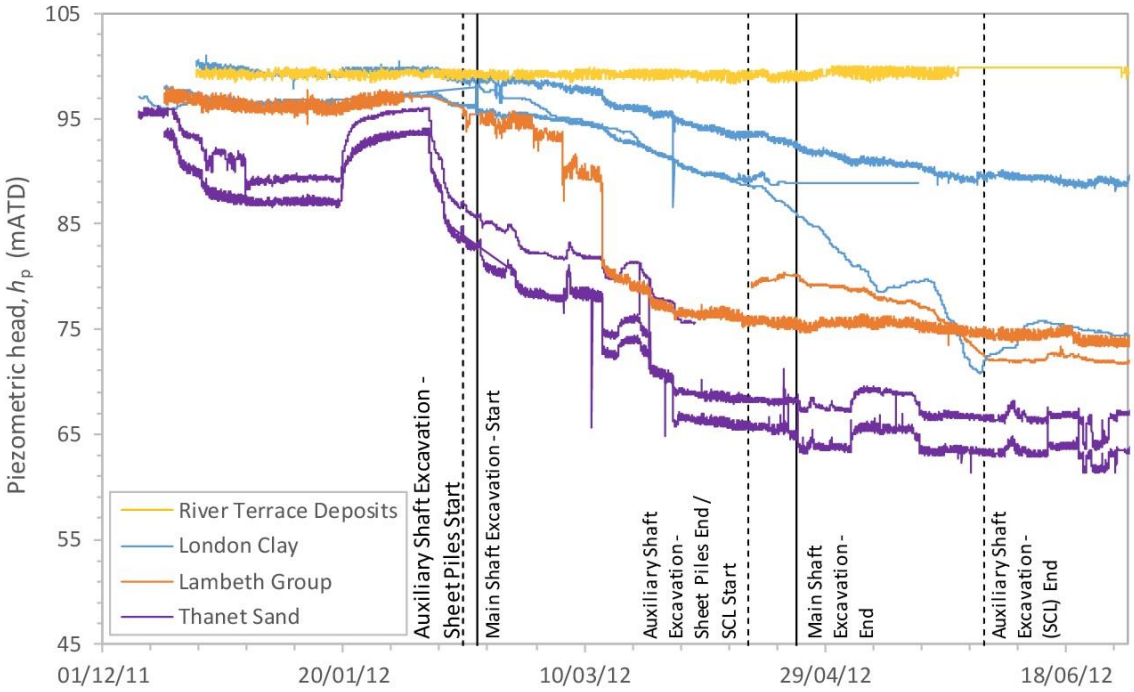

Figure 4.2 Piezometric head with time (Crossrail, 2016e; and J. Newhouse, 2017)

5 Numerical Analysis of the ground movement at Limmo Peninsula Tunnelling Site

In this Chapter the software used and the simplifications carried out in order to model the Limmo Peninsula Tunnelling Site shafts are presented. The geometry, boundary conditions, materials and excavation phases are presented. The simplified process in order to replicate the dewatering scheme used to construct the shafts is also explained.

5.1 Introduction

The software used for analysis the geometry, the material properties, the boundary conditions, flow conditions and stage construction is PLAXIS 2D FEM v2018.01 developed by Plaxis Company. Moreover, Plaxis Company provides another software for three-dimensional analysis, PLAXIS 3D.

On PLAXIS 2D FEM Input v2018.01, two types of model, axisymmetric or plane strain. The condition used in this work is Axisymmetric condition which is a simplification of a 3D model as the shafts are considered to be rotationally symmetric around the central axis. This type of analysis is commonly applied for circular structures with uniform radial cross-section and loading conditions around the central axis and the deformation and stress state are assumed to be identical in any radial direction.

For post-processing purposes, Plaxis provides an output software called PLAXIS 2D Output v2018.01.

5.2 Main Shaft

5.2.1 Geometry

The simplified geometry of the Main Shaft at Limmo Peninsula Tunnelling Site is presented on Figure 5.1. The 2D model extended vertically from the top of the Made Ground to the bottom of the Thaned Sand. Horizontally, the extension of the model is three times the excavation depth, avoiding the interaction with the boundary. The Lambeth Group is considered as London Clay, but with higher permeability, assuming that the mechanical properties for each soil are identical.

The Main Shaft excavation consist of an installation before the excavation of 55 meters Diaphragm wall and then 39.1 meters of inner excavation

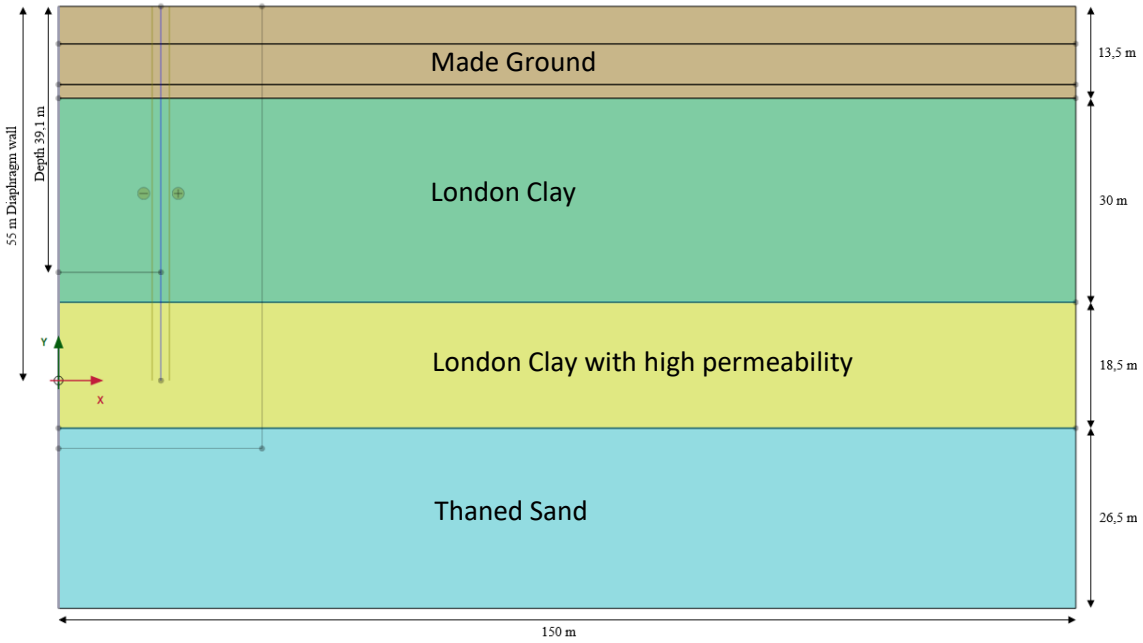

Figure 5.1 Geometry of the Main Shaft

5.2.2 Boundary conditions

In order to simulate the axisymmetric behaviour, the lower boundary is completely fixed and the horizontal displacements along the vertical contours are fixed. The soil is considered to be partially saturated throughout all the calculation. Thus, the upper boundary along the horizontal contour and the right boundary along the vertical contour are open. However, the left boundary along the vertical contour (where is located the symmetry axis) and the lower boundary along the horizontal are closed for water flow.

5.2.3 Mesh

The mesh has been refined in the region where the stresses and ground movement are relevant for the Main Shaft in order to get more accurate results and optimise the computational cost. In the area, which is not considered the refinement, an unstructured mesh is studied with an element size of 6.97 m. It can be observed the refined region in Figure 5.2.

Figure 5.2 Refined region of the Main Shaft

Figure 5.3 shows the mesh formed as a triangular element with 15 nodes used for the calculation. The solution of the problem can be slightly mesh dependent in finite element calculations, indicating the minimum size of the elements in the model to ensure that the results of an analysis are not influenced by changing the size of the mesh.

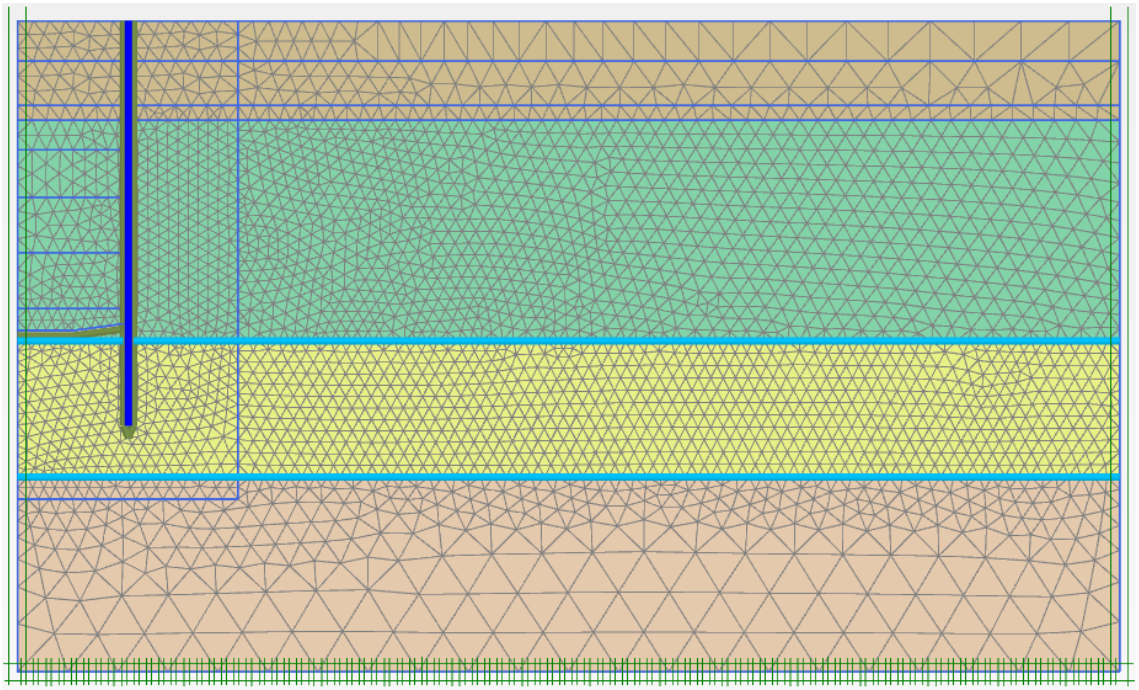

Figure 5.3 Used mesh for calculations of the Main Shaft (6.97 m triangle elements with 15-nodes)

5.3 Auxiliary Shaft

5.3.1 Geometry

The vertical and horizontal extensions of the model are the same of the Main Shaft as described in Section 5.2.1. The Lambeth Group is also considered as London Clay, but with higher permeability. Figure 5.4 presents the simplified geometry for the Auxiliary Shaft.

The Auxiliary Shaft consist of 16.8 meters of Steel Sheet Pile (support before the excavation) and 22 meters of Sprayed Concrete Lining (support after excavation).

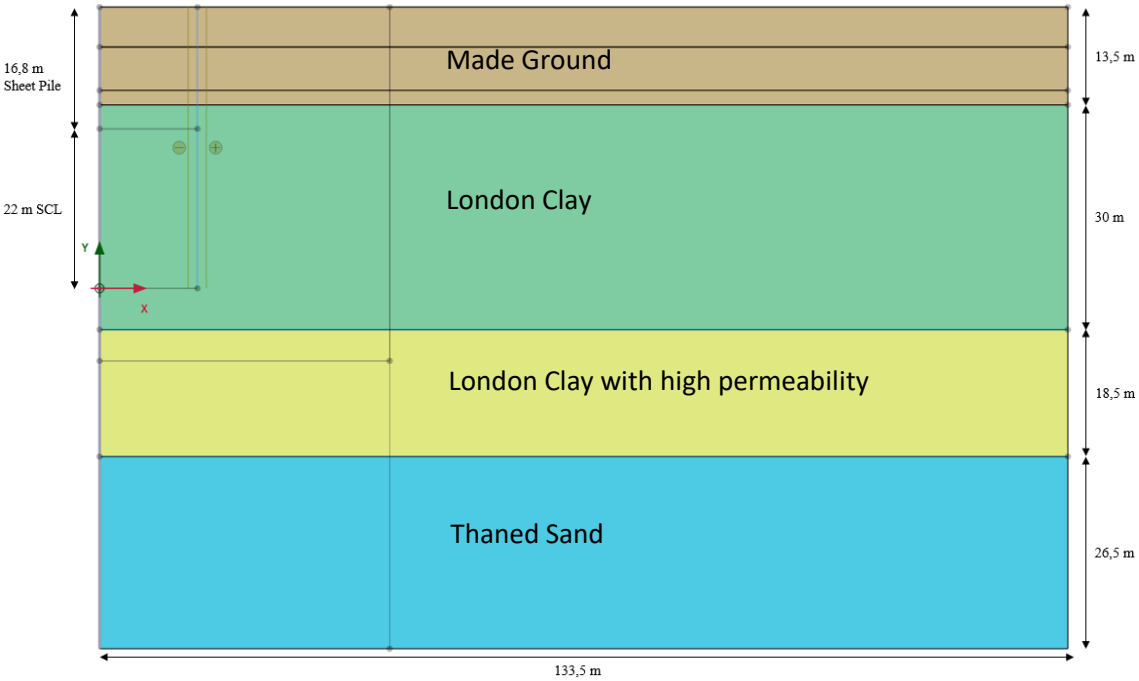

Figure 5.4 Geometry of the Auxiliary Shaft

5.3.2 Boundary conditions

As described in Section 5.2.2, the boundary conditions are the same defined on the Main Shaft at Limmo Peninsula Tunnelling Site.

5.3.3 Mesh

The Auxiliary Shaft mesh, it has been refined as described in Section 5.2.3. But, the element size of the unstructured mesh is 6.41 m. Figure 5.5, shows the refined region. The mesh is also formed with 15-nodes triangular elements.

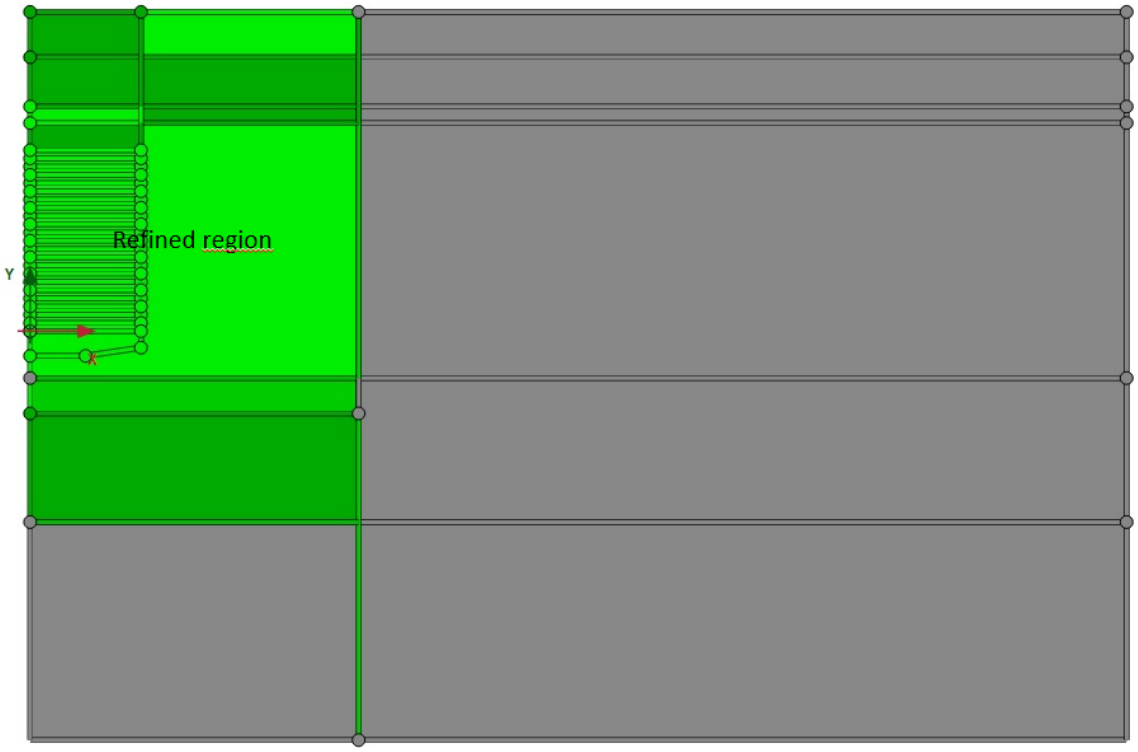

Figure 5.5 Refined region of the Auxiliary Shaft

5.4 Materials

Within this work, the Hardening Soil constitutive models is used to model the behaviour of the soil, particularly the Hardening Soil model for Made Ground and the Hardening Soil Small Strain model for London Clay. The soil material properties assumed while simulating the Main Shafts and Auxiliary Shaft at Limmo Peninsula Tunnelling Site are presented in Table 5.1, proposed by M. Chandegra and A. Kokkinou (2016). In this case, as Lambeth Group is present on site, the strength parameters used for the London Clay are applied to the Lambeth Group strata but with high soil permeability, i.e. with a 1E-5 m/s permeability in both directions.

As selected the Hardening Soil and Hardening Soil – Small Strain models on PLAXIS 2D FEM, it is possible to choose the type of material behaviour (Drained, Undrained A and Undrained B). The drained behaviour is used for high permeability soils, low loading velocity and long-term behaviour. However, the undrained behaviour is used for high permeability soils, high loading velocity and short-term behaviour. Within this work, the model characteristics is carried out are the undrained behaviour. Moreover, the Undrained (A) is chosen, because the Undrained (B) sets automatically a friction angle of 0 and the stiffness moduli of the model is no longer stress-dependent and exhibits no compression hardening, despite retaining shear hardening and unloading-reloading modulus, according to Plaxis Manuals (2018).

Parameter	Made Ground	London Clay
Drainage type	Undrained (A)	Undrained (A)
Dry soil weight (kN/m^3)	18	20
Wet soil weight (kN/m^3)	18	20
Permeability in hor. direction (m/s)	1.0E-10	1.0E-11
Permeability in vert. direction (m/s)	1.0E-10	1.0E-11
Secant stiffness in standard drained triaxial test (kPa)	10000	77625

Parameter	Made Ground	London Clay
Tangent stiffness for primary oedometer loading (kPa)	10000	77625
Unloading/reloading stiffness (kPa)	30000	232875
Cohesion (kPa)	20	1
Friction angle (º)	25	24
Dilatancy angle (º)	0	0
Poisson's ratio for unloading/reloading	0.2	0.2
Reference stress for stiffness (kPa)	8	100
Power for stress-level dependency of stiffness	0.01	0.6
Ko value for normal (1 – sin φ′, default setting)	0.577	0.593
Lateral Coefficient of At Rest Earth Pressure, K_o	-	1
Cohesion Increment (kN/m^3)	0	0
Cohesion and stiffness reference level (m)	0	55 – 38.8*
Failure ratio (default setting)	0.9	0.9
Tensile Cut of Stress value (kPa)	0	0
Interface strength reduction factor	0.67	0.5
Reference small strain shear modulus (kPa)	-	139725
Shear strain magnitude at $0.722G_0$	-	0.000293

*Main Shaft and Auxiliary Shaft reference level values.

Table 5.1 Soil parameters for the simulation (based on M. Chandegra and A. Kokkinou, 2016)

The Main Shaft and the Auxiliary Shaft linings are modelled in both cases as an elastic material. The Main Shat structure was built using diaphragm walls and the Auxiliary shaft, the first 16.8 m deep with steel sheet pile, GU 6N according to ArcelorMittal Sheet Piling (2018), and the next 22 m with Sprayed Concrete Lining; as described in Chapter 4. The lining parameters for diaphragm wall and sheet pile are presented in Table 5.2.

Structural element	Young Modulus (MPa)	Primary lining wall thickness (m)
Diaphragm wall	19600	1.2
Sheet pile (GU 6N)	200000	0.308

Table 5.2 Diaphragm wall and sheet pile parameter (ArcelorMittal Sheet Piling, 2018)

However, the primary SCL lining properties change along time: the compressive strength, modulus of elasticity, creep and shrinkage. The last two properties are greater than the conventional concrete. This effect is taken into account on numerical modelling considering a reduction of the modulus of elasticity (between 1.5 - 2.5). Three different SCL parameters have been used, as defined in Table 5.3.

SCL	Time (days)	Young modulus (MPa)	Primary lining wall thickness (m)
Initial young	0.25	5000*	0.75
Primary young	0.625	10000*	0.75
Primary old	28	18000	0.75

*Values obtained from Meschke (1996) Equation.

Table 5.3 Sprayed Concrete Lining parameter for the simulation

It should be noted that more advanced constitutive materials could be implemented in Plaxis in order to simulate the concrete ageing and this is discussed in Chapter 8.

5.5 Dewatering

As described in Section 4.3, changes on the groundwater level affects directly to the ground movement and the total stresses generated during the excavation. To reproduce the dewatering during the excavation, two drains between London Clay – London Clay with high permeability – and Thaned Sand have been implemented in the model. From Figure 4.2 (on page 28) the initial piezometric level head (98.5 mATD) and piezometric level head along time is obtained. Figure 5.6 provides the excavation depth at a given time. However, groundwater within the London Clay stratum has been historically shown to be hydrostatic, with the pressures below decreasing due to underdrainage into the more permeable strata below. However, within this work, the water pressures have been assumed to be fully hydrostatic.

To reproduce the dewatering in the PLAXIS 2D FEM software, several excavation phases have been created in the model. Phases were of 5 – 10 m excavation depth each one for the Main Shaft and the steel sheet pile lining for the Auxiliary Shaft, but for the SCL lining of the Auxiliary Shaft each phase was of 1 m depth. Before each excavation step is computed, a dewatering phase is defined, wherein the groundwater level corresponds to its excavation depth and time.

To analyse the changes on the groundwater level in PLAXIS 2D, it has been defined in calculation type as *Fully coupled flow-deformation*. According to Plaxis 2D Manuals, it analyses the simultaneous development of deformation and the pore pressures in totally saturated and partially saturated soils as a result of time-dependent changes of the hydraulic conditions. This analysis directly operates on the total pore water pressure, i.e. the sum of the steady-state and excess pore pressure. The results of the analyses are presented in next chapter.

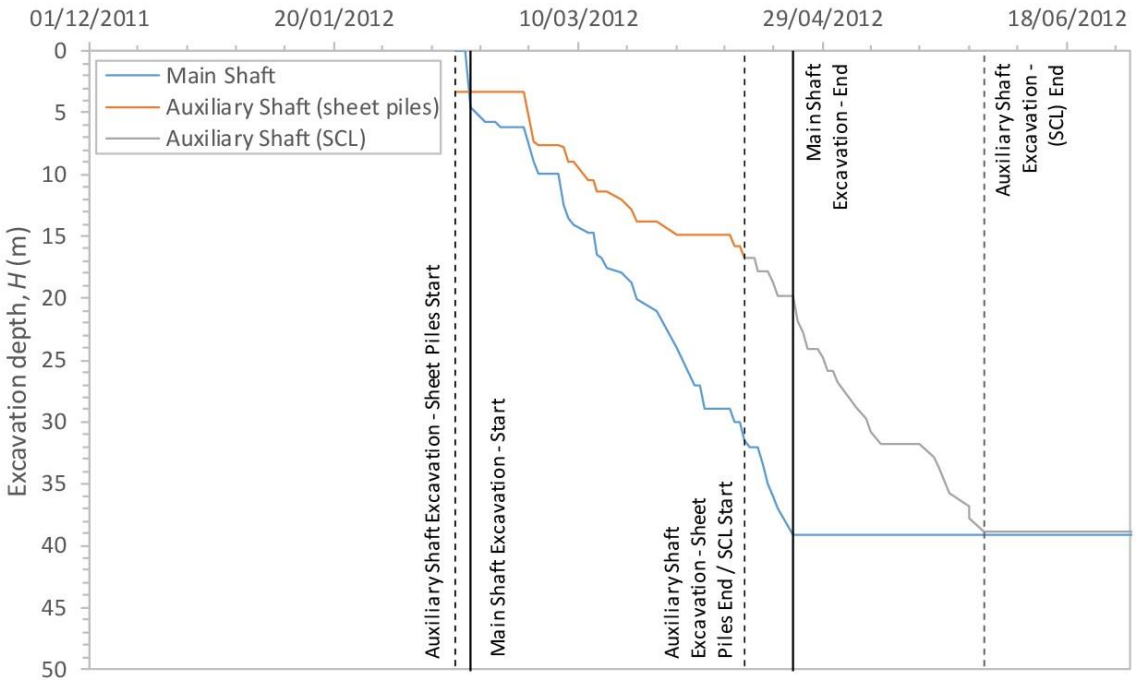

Figure 5.6 Main Shaft and Auxiliary Shaft excavation depth with time (DSJV, 2012b; and J. Newhouse ,2017)

6 Results

In this chapter, the Main Shaft and Auxiliary Shaft at Limmo Peninsula Tunnelling Site modelling carried out with Hardening Soil and Hardening Soil Small Strain material model are presented. The ground movement results have been compared with the ground movement measured during shaft construction and observed by Joseph Newhouse (2017) at Limmo Peninsula Tunnelling Site.

6.1 Introduction

Within this work, the real field data are measured shortly after the end of the excavation, hence the consolidation ground movement is not to be considered, but it has been calculated. The dewatering process has been reproduced in the model in a simplified manner. However, an effort has been devoted to reproduce as accurate as possible the effective stress changes in the soil, as described in Section 5.5. To analyse entirely the vertical displacements due to shaft excavation, the settlement generated due to the dewatering has been removed from the total displacement. However, the interaction between the Main Shaft and the Auxiliary Shaft has not been considered due to the axisymmetric model limitations on Plaxis 2D.

Furthermore, the ground movement due to shaft excavation achieved are compared to the formula presented by GCG (2007), that is Equation 2.5 in Section 2.2.4. Joseph Newhouse (2017) uses the formula to describe ground movement with distance from the wall in terms of the maximum movement at the wall, $\delta_{v,min}$, and the extent of the settlement trough, E, presented on Table 6.1, for the Main Shaft and Auxiliary Shaft.

Shaft	Excavation depth, H (m)	Internal diameter, D (m)	D/H (-)	$\alpha = \delta_{vmin}/H$ (%)	R = E/H	$\delta_{v,max}$ (mm)	E (m)
Main Shaft	39.1	30.2	0.68	-0.025	0.8	-9.775	31.28
Auxiliary Shaft	38.8	27	0.7	-0.095	1.1	-36.86	42.68

Table 6.1 Parameters used for GCG formula (2007) (Faustin et al., 2017; and J. Newhouse, 2017)

6.2 Main Shaft

The ground movement due to shaft excavation and dewatering at the end of the Main Shaft excavation, is presented in Figure 6.1. The changes on the groundwater level produce a total stress reduction, affected directly by the water pressure decrease, thus, generating settlements behind shaft lining in the Main Shaft model. However, at the end of the excavation it produces a positive vertical displacement in front of the shaft lining (i.e. formation level of the shafts) that has been generated by the difference between the initial stresses and final stresses under the shaft (i.e. removal of overburden).

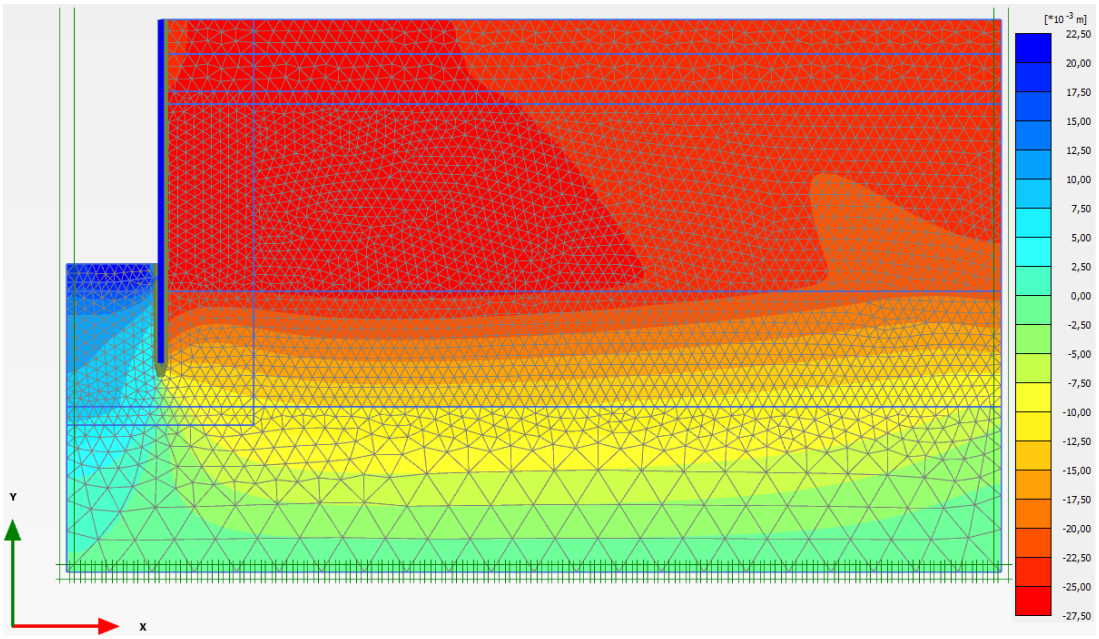

Figure 6.1 Total displacement u_y at the end of the excavation (scaled up 100 times), Max. value (blue, positive) = 0.0220 m and Min. value (red, negative) = -0.02696 m

Figure 6.2 presents the active pore pressure closer to the diaphragm wall (19 meters distance from the centre of the shaft) that occur at the end of the shaft excavation of the Main Shaft. It can be seen that the active pore pressure increases where London Clay layer is located due to its low permeability. However, the pressure decreases dramatically on the transition between London Clay soils but with different permeability. The active pore pressure is acting against the diaphragm wall and can generate ground movement.

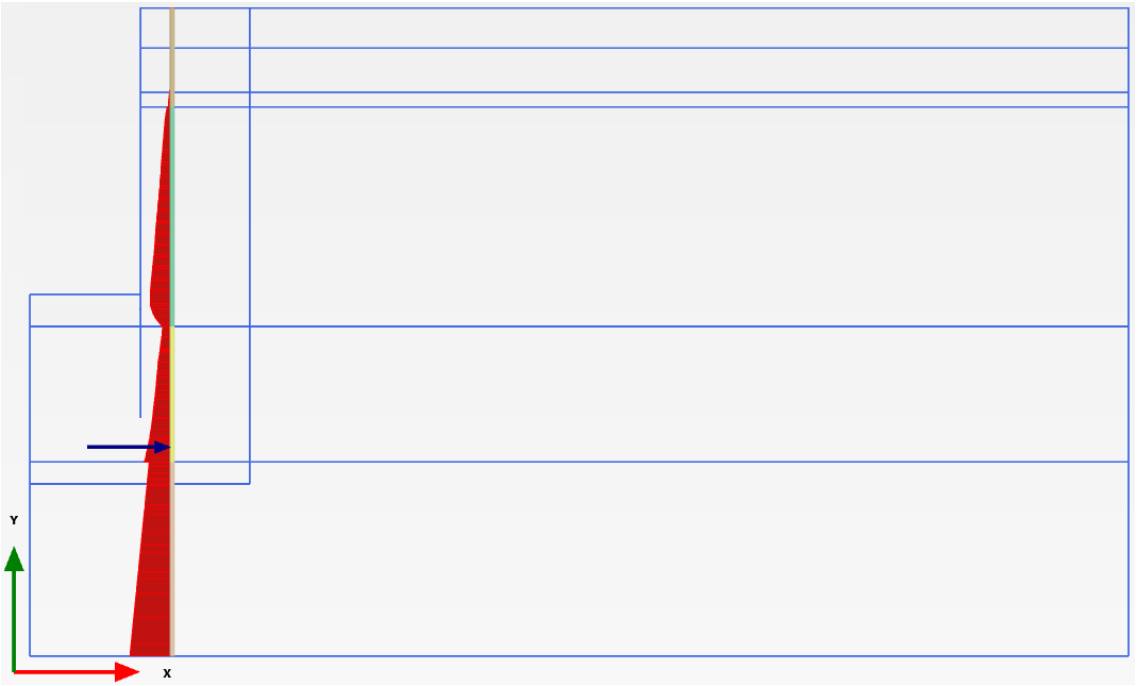

Figure 6.2 Active pore pressure p_{active} at the end of the excavation (scaled up 0.01 times) (Pressure = Negative) Max. value = 22.76 kN/m^2, Min. value = 575.4kN/m^2 and Equivalent force = -426.7E^3 kN/rad at x = 19 m, y = -4 m)

Figure 6.3 illustrates the vertical ground movement surface due to shaft excavation of the Main Shaft at the Limmo Peninsula Tunnelling Site observed on site (in blue dots). To prepare this figure, the dewatering displacements were removed from the total settlement (Newhouse 2017). As it can be seen, the field data with the dewatering movement subtracted, shows a lot of scatter including some positive movements (i.e. heave). The ground movements after 90 meters from the diaphragm wall show a scatter (in blue dots) in the range of +/- 5mm, being not representative. This is due to the fact that shaft excavation at Limmo Peninsula Tunnelling Site is located in London and 90 m away movements can be affected from an external element of the Main Shaft.

The yellow line in Figure 6.3 shows the calculated displacements after removing the displacements due to the dewatering process. A positive displacement is shown for approximately the first 20m behind the wall. This is due to the ground heave of overconsolidated clays during the excavation phase and the friction between the soil and the diaphragm wall. This effect largely occurs on shafts where the wall installation is prior to the excavation. Installation effects of the wall have not been modelled numerically due to the modelling difficulties and Plaxis 2D limitations.

It is considered that installing a diaphragm wall panel may produce release of soil initial stresses, developing some settlements close to the panel. If measurements close to the wall were available, most probably they would have been well reproduced by the black dashed line in Figure 6.3.

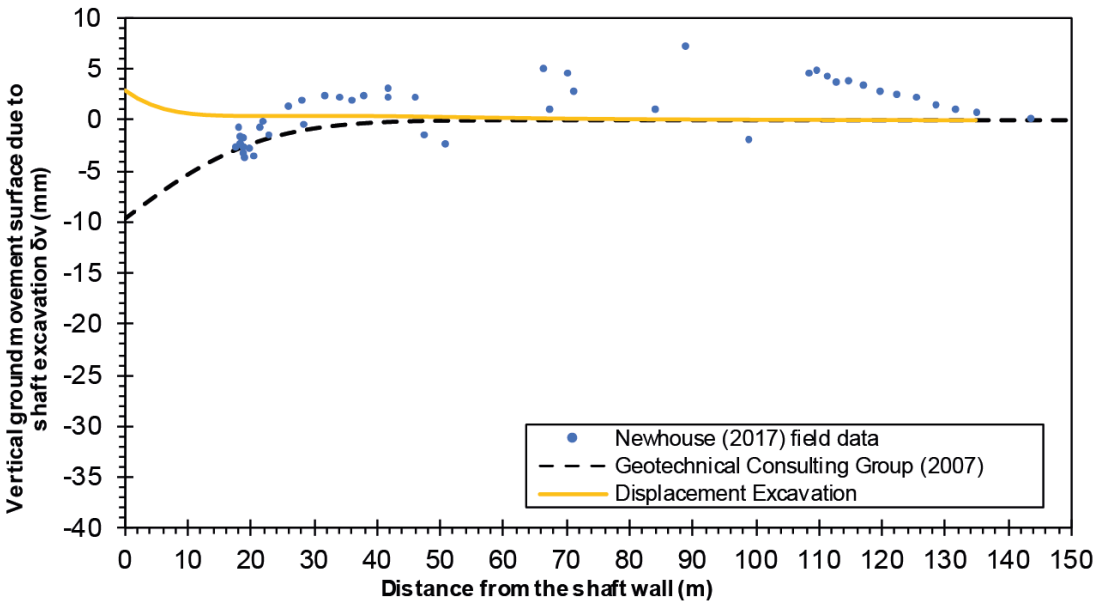

Figure 6.3 Settlement due to excavation with distance from the Main Shaft wall, after the excavation ends (Field data is obtained from J. Newhouse, 2017)

6.3 Auxiliary Shaft

In this section the ground movement due to Auxiliary Shaft excavation and dewatering is presented. Figure 6.4 presents the total displacements that occur at the end of the shaft excavation. In the upper half, the support lining of the shaft is built before the excavation and in the lower half, the support is finished after the excavation. As described in Section 6.2, in this shaft model settlements are generated behind shaft lining by the changes on the groundwater level. However, there is a significant negative increment of settlements behind the shaft wall due to the two different construction methods.

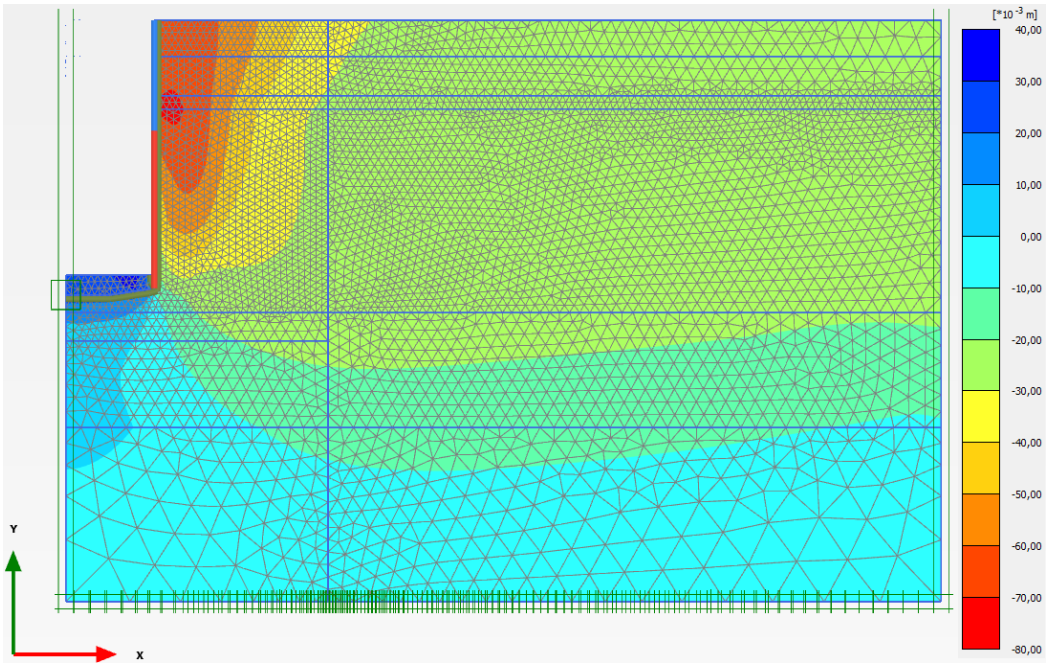

Figure 6.4 Total displacement u_y at the end of the excavation (scaled up 50 times), Max. value (blue, positive) = 0.03303 m and Min. value (red, negative) = -0.07160 m

Figure 6.5 presents the active pore pressure closer to the lining wall (19 meters distance from the centre of the shaft) that occur at the end of the shaft excavation of the Auxiliary Shaft. As described in Section 6.2, it can be seen that the active pore pressure increases where London Clay layer with low permeability is located. Also, the pressure decreases dramatically on the transition between soils with different permeability.

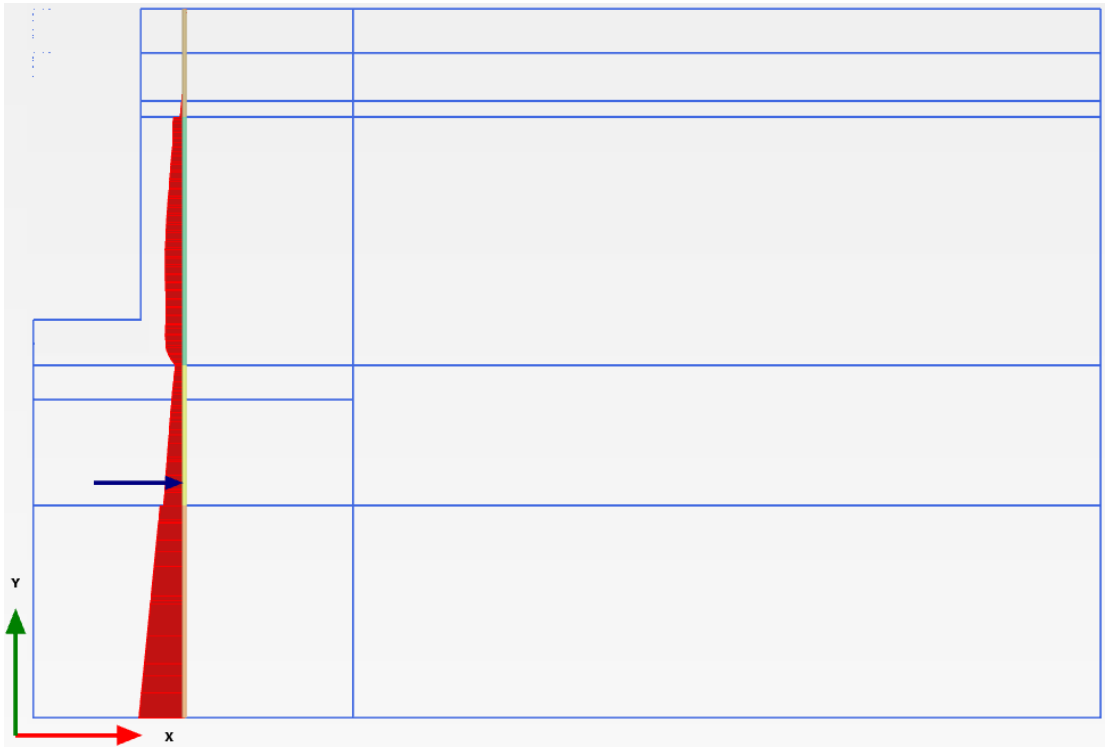

Figure 6.5 Active pore pressure p_{active} at the end of the excavation (scaled up 0.01 times) (Pressure = Negative) Max. value = 22.74 kN/m^2, Min. value = 566.0kN/m^2 and Equivalent force = -399.9E^3 kN/rad at x = 19 m, y = -20 m)

Figure 6.6 presents the settlements surface due to shaft excavation of the Auxiliary Shaft observed on site (in blue dots). Furthermore, the settlement generated due to the dewatering had been removed from the total displacement (Newhouse 2017). As described in Section 6.2, the ground movements after 90 meters from the Auxiliary Shaft wall also show a scatter in the range of +/- 5 mm, being not representative.

In Figure 6.6, it can be observed the calculated displacements of the Auxiliary Shaft (in yellow line) after using the subtraction procedure as described in Section 6.2. Herein, it produces a significant settlement the first 40m behind wall, larger movement due to the shaft excavation than the Main Shaft. It can be seen that the minimum displacement is found closer to the wall (2.5 meters away). Note that minimum vertical displacement refers to maximum settlement because of the sign convention. This effect mainly has been generated between the heave of overconsolidated clays during the sheet pile half excavation and the friction between the soil and the lining wall.

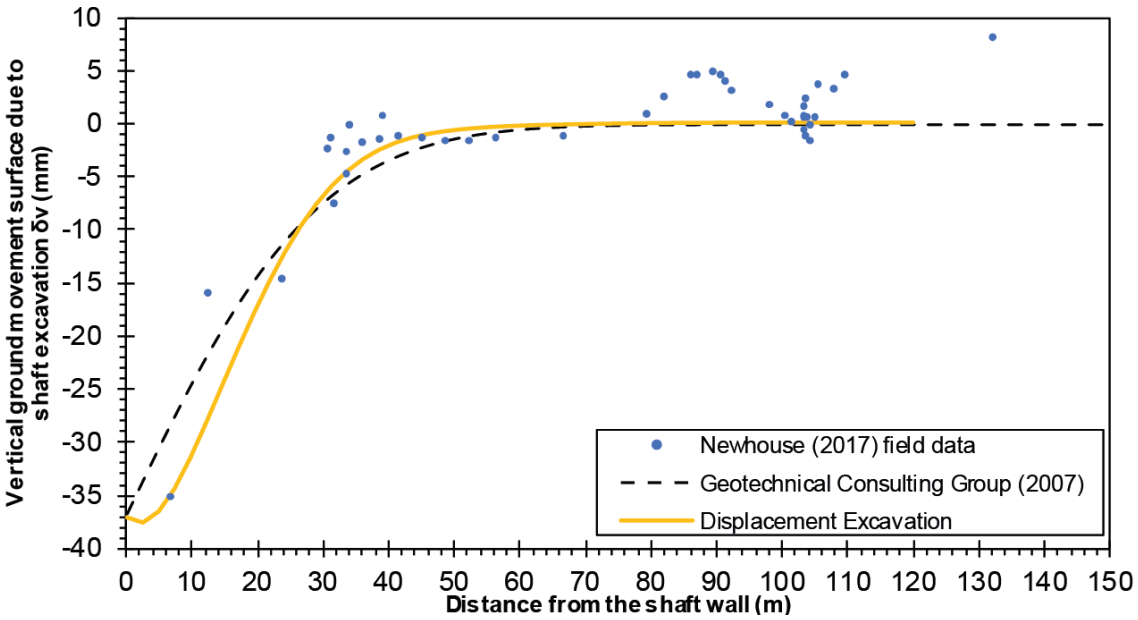

Figure 6.6 Settlement due to excavation with distance from the Auxiliary Shaft wall, after the excavation ends (Field data is obtained from J. Newhouse, 2017)

6.4 Discussion

It can be seen in Figure 6.3 and Figure 6.6, that the Main Shaft and the Auxiliary Shaft numerical model tackled within this work the ground movement due to shaft excavation and matches reasonably the one observed and measured in the field (J. Newhouse 2017). Furthermore, these results validate the soil parameters proposed by M. Chandegra and A. Kokkinou (2016) to accurately model ground movements in overconsolidated clay deposits.

Figure 6.3 and Figure 6.6 show the difference between the ground movement surface due to the shaft excavation on the Main Shaft and the Auxiliary Shaft, after the excavation ends; which highlights the importance of the construction method adopted for shaft construction; whether the installation occurs before the excavation and the installation or the excavation are concurrent. However, the Auxiliary Shaft is supported in the upper half of the wall by Steel Sheet Pile, catalogued as installation prior to excavation, but the dimensions and the material properties are different than the diaphragm wall from the Main Shaft.

In this work, the importance of the ground movement after the excavation end has been studied, including the behaviour of the settlement during the excavation progress and in case of Sprayed Concrete Lining, the effect of excavation and installation following the methodology adopted by Newhouse (2017).

Figure 6.7, it presents the behaviour of the ground movement during the excavation progress of the Main Shaft (Diaphragm wall) and Auxiliary Shaft (Steel Sheet Pile and SCL) in terms of the minimum vertical displacement, $\delta_{v,min}$, normalised by the excavation depth, H, against the shaft diameter, D, normalised by the excavation depth. Grey dashes lines indicate linear relationships between the variables and are shown for reference, with gradients at intervals on a logarithmic scale. Key points to note are listed below:

1. The Main Shaft shows no appreciable ground movement during the excavation process and excavation ends and thus the value of α has been taking as zero. This occurs because in the course of all the shaft excavation the vertical displacements behind the diaphragm wall are positive and the minimum settlement is located on the end of the model surface.
2. The Auxiliary Shaft shows no appreciable ground movement until D/H < 2.3 (H ≈ 11.5), wherein starts progressively to increase. This increment is taken place by the water pressure applied behind the sheet pile wall and the excavation. However, in transition to SCL excavation, the settlement and the normalised ground movement dramatically increase.

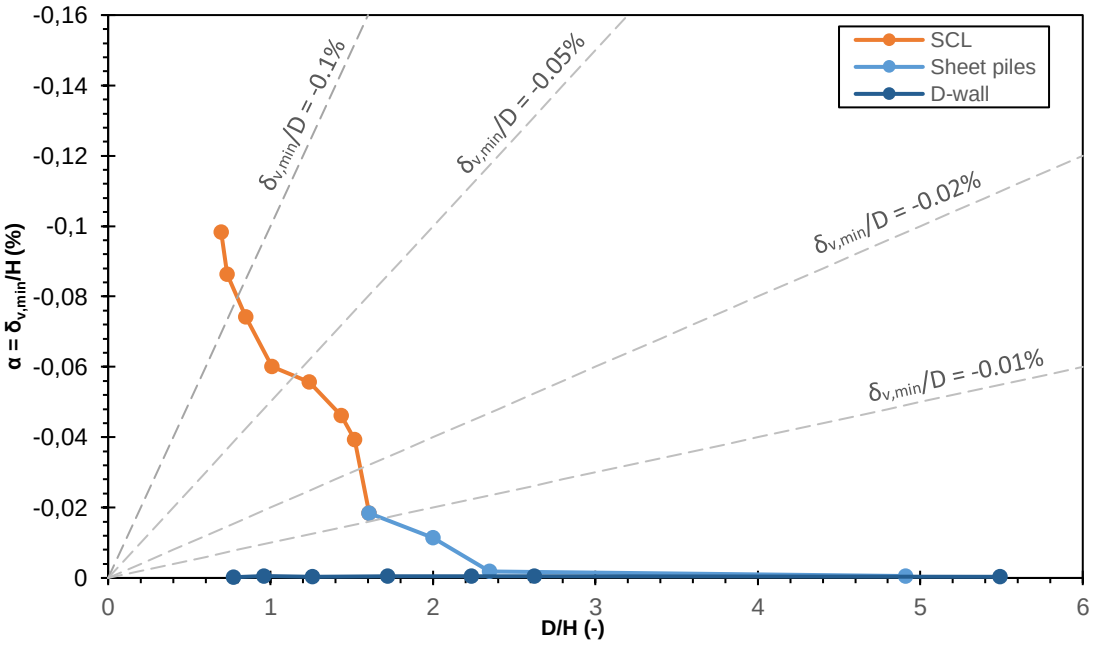

Figure 6.7 Vertical ground movement against normalised diameter due to Main Shaft and Auxiliary Shaft excavation

Furthermore, using the same geometry and materials, an analysis has been undertaken with totally unsaturated soil and fully saturated soil without dewatering. It can be observed that groundwater is a crucial characteristic that influence on the final ground movement results. Thus, are listed below:

1. The shaft models totally dried shows fewer ground movements during the excavation and after the excavation ends. This is due to the absence of water pressure in the soil that in the saturated case will be pushing the wall with this pressure behind the excavation.

2. The shaft models without dewatering shows higher settlements during the excavation as higher is the hydrostatic force against the wall. The results obtained are more conservative than the models considering changes on the groundwater level.

Next chapter a sensitivity analysis is presented, with the aim of expanding the knowledge on the behaviour of shafts, construction method and induced ground displacements.

7 Parametric study

In this chapter, a parametric study concerning the geometry (i.e. depth and diameter values) of the shaft excavation and installation is carried out. For this analysis, the same geometry and material properties have been used (i.e. axisymmetric model of a shaft with the same structural element properties). For the sake of simplification, the geological stratigraphy adopted for the parametric study consists of only the London Clay unit. This will make a parametric study more general for the future and for practical purposes for shafts in overconsolidated clay deposits. The same constitutive model and strength parameters have been used (i.e. Hardening Soil – Small Strain model and parameters presented in Table 5.1).

Moreover, in the parametric study has been upheld the initial groundwater level. However, it is not reproduced the dewatering among the shaft construction. For this reason, the parametric study is considered to be more conservative for practical applications, as described in Section 6.4

7.1 Influence of the shaft diameter

In order to study the effect of different radii of the shaft excavation, three different diameters are taken into account. In Table 7.1, four cases with different diameter are shown, wherein, the first one is the model described in Chapter 5 in order to compare the results. The depth of the shaft for all cases is 38.8 meters, where, the 16.8 meters of the upper half is constructed with Steel Sheet Piles and the 22 meters of the lower part, with Sprayed Concrete Lining.

	1st case*	2nd case	3rd case	4th case
Internal diameter, D (m)	27	27	32	20
Excavation depth, h (m)	38.8	38.8	38.8	38.8

*Same model as described in Chapter 5

Table 7.1 Parameters used for the parametric study in Section 7.1

Figure 7.1 presents the vertical displacements after the excavation ends. Between the first and the second case (yellow and blue line, respectively), there is only a difference of 3mm having the same diameter and excavation depth. The second case has higher settlement produced by the hydrostatic force against the wall. It can be seen, that changing the shaft diameter affects directly the vertical ground movement, as the higher diameter, the higher the displacement.

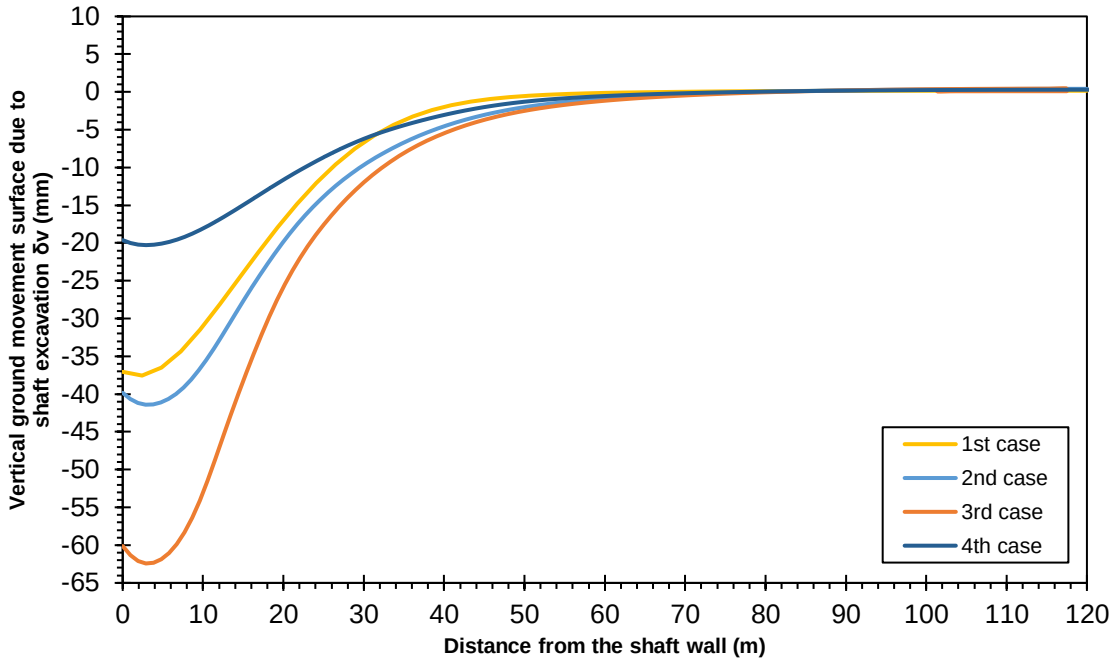

Figure 7.1 Settlement due to excavation with distance from the shaft wall cases, after the excavation ends

In Figure 7.2, it can be seen the behaviour of the ground movement during the excavation progress of the shaft constructed with Steel Sheet Pile and SCL in terms of the minimum vertical displacement, $\delta_{v,min}$, normalised by the excavation depth, H, against the shaft diameter, D, normalised by the excavation depth. The dashed coloured lines indicate the displacement occurred when the excavation is in front of the Steel Sheet Pile whereas when the excavation is in front of the SCL, this is shown in coloured solid lines. Grey dashed lines indicate linear relationships between the variables and they are shown for reference, with gradients at intervals on a logarithmic scale. Herein, it can be observed the importance of the diameter, as higher diameter higher settlement. During the sheet pile excavation, the second, the third and fourth cases produce higher normalised vertical displacements compared with the first case, presented in Chapter 5. This is due to the fact that in these three cases, the dewatering has not been reproduced and the excavation depth reaches the groundwater level between the first and the second point, increasing the hydrostatic force against the wall.

However, between the first case and the second case (yellow and blue line, respectively) when r the SCL excavation begins the same normalised vertical displacement behaviour is obtained. As described in Section 6.4, when no changes are considered in the groundwater level, the results obtained are more conservative.

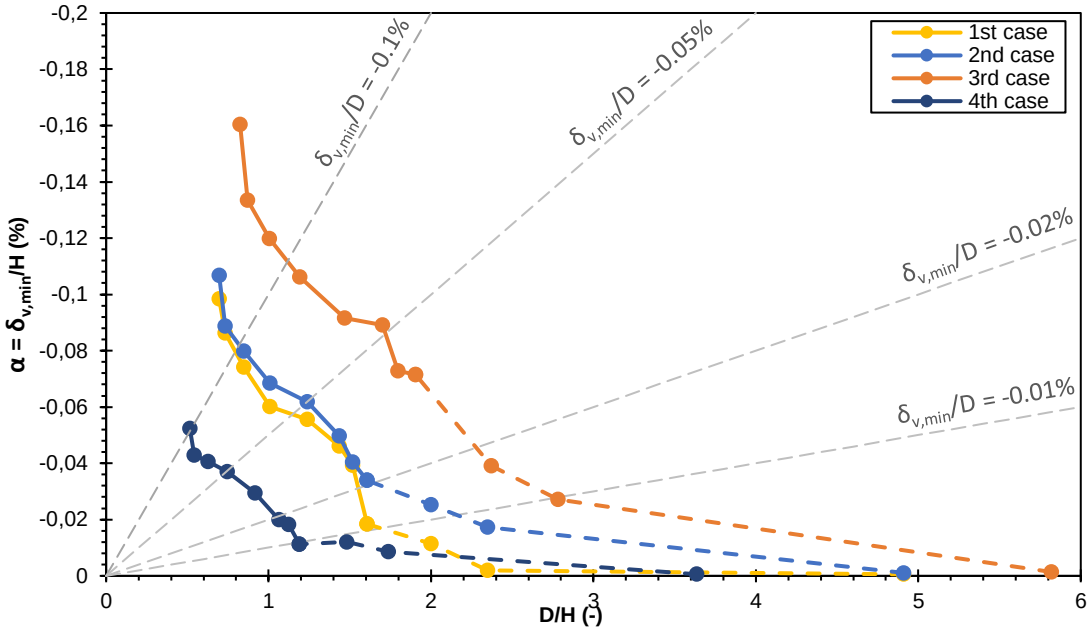

Figure 7.2 Vertical ground surface movement against normalised diameter due to excavation

7.2 Influence of the SCL shaft depth

Once studied the effect of changing the diameter of the shaft excavation, the excavation depth parametric study is presented in this section. The Steel Sheet Pile excavation depth has maintained and only the Sprayed Concrete Lining (SCL) depth has been changed. The six case studies are presented in Table 7.2, also the internal diameter has been changed for some cases, to understand its sensitivity. The first case has the shaft geometry model presented in Section 5 (38.8 meters shaft depth, 16.8m Steel Sheet Piles excavation depth and 22m of SCL.

	1st case	2nd case	3rd case	4th case	5th case	6th case
Internal diameter, D (m)	27	32	27	32	20	20
Excavation depth, H (m)	38.8	43.8	43.8	38.8	32.8	38.8
SCL excavation depth (m)	22	27	27	22	16	22

Table 7.2 Parameters used for the parametric study in Section 7.2

In Figure 7.3, the vertical ground movement normalised by the excavation depth for all the cases are presented. It can be observed that, when the diameter is the same, the normalised settlement behaviour is identical during the shaft excavation until this reaches the final depth. It can also be seen that the normalised ground movement increases for the sheet pile excavation and this is believed to be due to the hydrostatic force acting on the wall produced by the groundwater level.

It is possible to observe that, for cases with 27 meters of inner diameter (first and third case), the normalised vertical ground movement when the shaft excavation begins and during the sheet pile digging increases linearly. At the transition to SCL (D/H = 1.6) movements increase dramatically due to the change in construction method (installation and excavation are concurrent method). Thus, until the excavation ends, the normalised ground movement for case 1 is obtained with $\alpha = \delta_{v,min}/H = -0.107\%$ and for case 2, $\alpha = -0.112\%$ (D/H = 0.69 and D/H = 0.62, respectively).

However, the cases two and four where the internal diameter is 32 meters the normalised ground movement increases linearly when the excavation begins, as described for cases 1 and 3, and ends before the transition to SCL occurs. For D/H > 2.37 (sheet pile excavation zone), the settlement normalised by the excavation depth increases dramatically and reaches the final digging depth with α = -0.168% for case 2 (D/H = 0.73) and α = -0.160% for case 4 (D/H = 0.69).

Finally, the normalised vertical displacement of cases 5 and 6 with 20 meters of inner diameter increases linearly until D/H = 1.48. A decrease in the normalised ground movement is between D/H = 1.48 and D/H = 1.19, but it can be seen that settlements also occur, taking into account the slope between the grey dashed line $\delta_{v,min}/D$ = -0.01% and the shaft excavation progress. After the transition to SCL, movements increase dramatically until shaft excavation ends, with α = -0.051% for case 5 and α = -0.052% for case 6 (D/H = 0.61 and D/H = 0.52, respectively).

In addition to that, it can be seen that SCL excavation depth has also some influence on the total final normalised displacement. In this case the more SCL excavation and consequently the deeper the total excavation, the final normalised vertical ground movement is slightly bigger than for the shallower excavated shaft.

Hence, the vertical displacements due to shaft excavation are affected more by the shaft diameter than by the excavation depth. The larger diameter of the shaft, the more vertical displacements are observed.

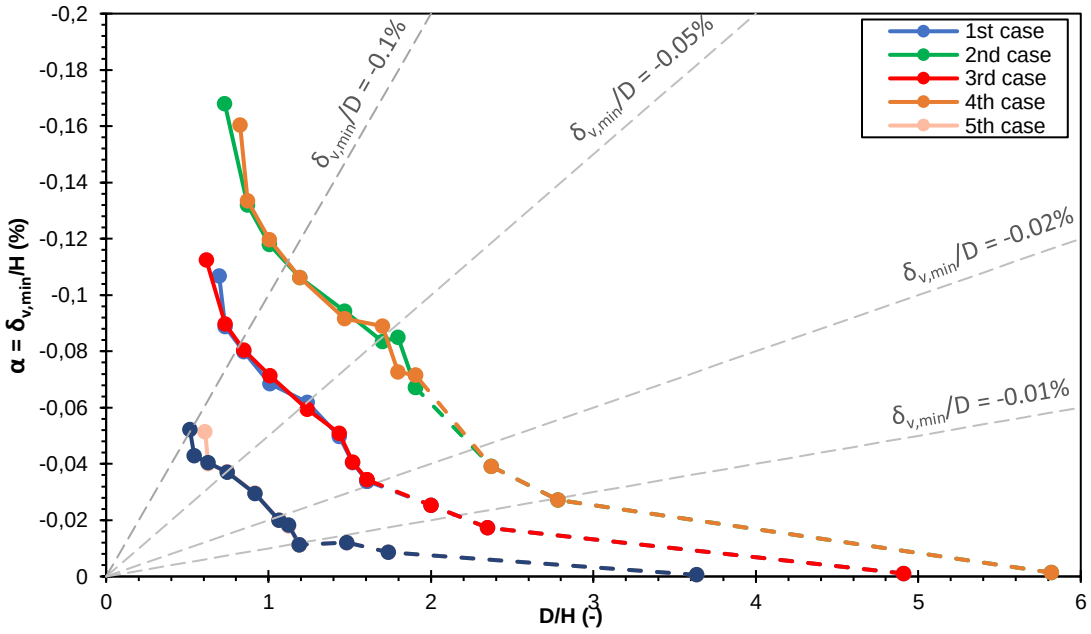

Figure 7.3 Vertical ground surface movement against normalised diameter due to excavation

7.3 Influence of Steel Sheet Pile length

After being analysed the influence of the excavation depth with Sprayed Concrete Lining, the effect of Steel Sheet Piles length is presented below. Two different sheet pile lengths (7.8 meters and 24.8 meters) have been selected to carry out the parametric study. In what follows, the Steel Sheet Pile excavation results have coloured dashed lines and the Sprayed Concrete Lining, coloured solid lines.

The six studies cases are presented in Table 7.3, wherein, the odd cases are 7.8 meters of sheet pile length and the even cases, 24.8 meters.

	1st case	2nd case	3rd case	4th case	5th case	6th case
Internal diameter, D (m)	27	27	32	32	20	20
Excavation depth, H (m)	38.8	38.8	38.8	38.8	32.8	32.8
Sheet pile length (m)	7.8	24.8	7.8	24.8	7.8	24.8
SCL length (m)	31	14	31	14	25	8

Table 7.3 Parameters used for the parametric study in Section 7.3

In Figure 7.4, it can be seen for odd cases (7.8 meters of sheet pile length), during the sheet pile excavation, the normalised vertical ground movement due to shaft excavation is negligible. This is due to the short length of supported excavation plus that the groundwater level is not acting on its full length. However, in the transition to SCL (coloured solid lines) excavation the normalised ground movement increases due to the unsupported excavation. After a certain point the normalised settlement, α, dramatically increases up until the end of the excavation.

Additionally, it can be observed that the normalised vertical displacement, α, at the beginning of the excavation increases significantly for the even cases. As described above, the water pressure produced by the ground water level affects pressure directly to the Steel Sheet Pile wall and generates displacements behind the lining wall. Moreover, when the excavation depth is reaching the end of the sheet pile excavation the normalised ground movement dramatically increases, caused by the soil digging in the passive site of the wall. On transition to SCL that value continues to increase until the excavation ends.

Between cases 1 and 2, where the internal diameter is 27 meters, the normalised ground movement shows after the excavation ends (D/H = 0.67) a difference of $\Delta\alpha$ = -0.019% (α = -0.123% for case 1 and α = -0.104% for case 2). Furthermore, for cases 3 and 4 (32 meters of internal diameter), after the excavation ends (D/H = 0.82) those values are α = -0.181% and α = -0.161%, respectively. Finally, cases 5 and 6 (20 meters of internal diameter), at the end of excavation, (D/H = 0.60) the obtained α values are α = -0.066% and α = -0.046%, respectively.

Figure 7.4 shows that the final displacement is influenced by the method of construction independently of the shaft diameter, as described above. Moreover, it can also be seen that for small diameters (cases 5 and 6), i.e. 20 meters of internal diameter, the construction methodology affects the final normalised vertical displacement and the intermediate stages, too. For instance, case 6 shows a final vertical displacement smaller than case 5 which has a deeper length of unsupported excavation.

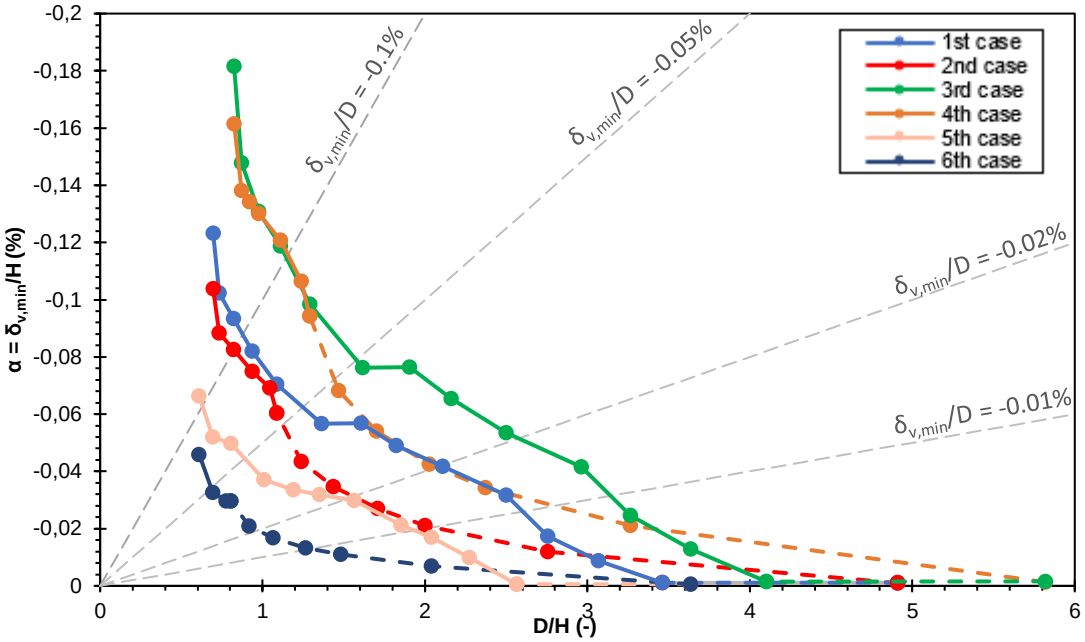

Figure 7.4 Vertical ground surface movement against normalised diameter due to excavation

7.4 Constant normalised diameter over depth, D/H = 0.5

From the previous parametric studies, it can be concluded that the key modelling parameters that influence the ground movement due to shaft excavation are the internal diameter and the excavation depth. Thus, a constant normalised diameter over depth study is presented in this Section.

When modifying the internal diameter and the excavation depth keeping its ratio constant, the relationship between that ratio and the minimum vertical displacement, $\delta_{v,min}$, (or maximum settlement), normalised by the excavation depth, becomes almost proportional. In Table 7.4, the basic dimensions of the six studied cases are presented; with a singularity related with the parameters in Section 7.2, each parameter is divided by two.

	1st case	2nd case	3rd case	4th case	5th case	6th case
Internal diameter, D (m)	13.5	16	13.5	16	10	10
Excavation depth, h (m)	19.4	21.9	21.9	19.4	16.4	19.4
SCL excavation depth (m)	11	13.5	13.5	11	8	11

Table 7.4 Parameters used for the parametric study in Section 7.4

In Figure 7.5, the minimum vertical displacement, $\delta_{v,min}$, normalised by the excavation depth, H, against the shaft diameter, D, normalised by the excavation depth, is presented. The shaft excavation is constructed with Steel Sheet Pile (coloured dashed lines) and SCL (coloured solid lines), as previously described. It can be seen that during the sheet pile excavation, the normalised ground movement is negligible (about 10^{-4}). However, after SCL transition, the normalised vertical displacement increases dramatically for all cases. Grey dashes lines indicate linear relationships between the variables and are shown for reference, with gradients at intervals on a logarithmic scale.

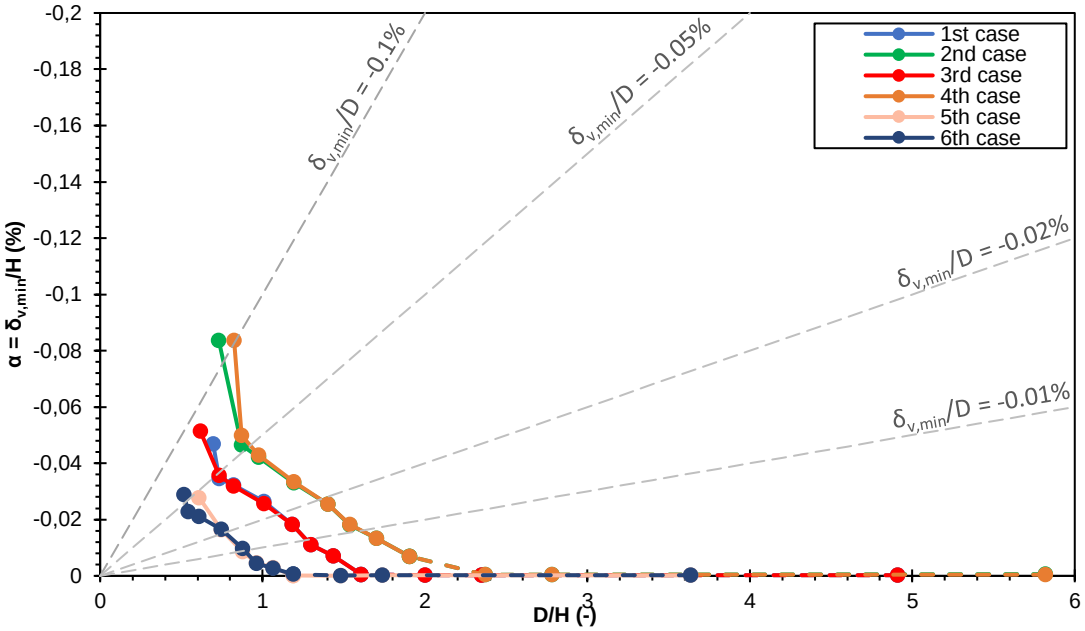

Figure 7.5 Vertical ground surface movement against normalised diameter due to excavation

The normalised ground movement due to shaft excavation in this section and the results in Section 7.2 have been compared. Figure 7.6 shows that, just after starting the excavation, for small internal diameters, the normalised ground movements are negligible. However, the cases studied above show for the same ratio D/H, a significant normalised settlement for high excavation depths.

Figure 7.6 presents the normalised vertical ground movement for case 1 studied above and case 1 in Section 7.2. It shows on the transition of SCL about the same D/H = 1.6, but different α, $\alpha = \delta_{v,min}/H$ = -0.0005% and α = 0.0339%, respectively, and also when the shaft excavation ends D/H = 0.70, the values obtained are α = -0.047% and α = 0.107%. Moreover, for cases 4, studied in this section and Section 7.2, a similar behaviour is observed , for D/H = 1.9 (transition of SCL), α = -0.0069% and α = 0.0715%, respectively, and for D/H = 0.82 (shaft excavation ends), α = -0.047% and α = 0.160%.

Up to a point, the normalised ground movement increases for cases with small internal diameter and excavation depth. The behaviour for the first and the fourth cases between different internal diameter and shaft excavation parameters but maintaining the ratio D/H are approximately identical.

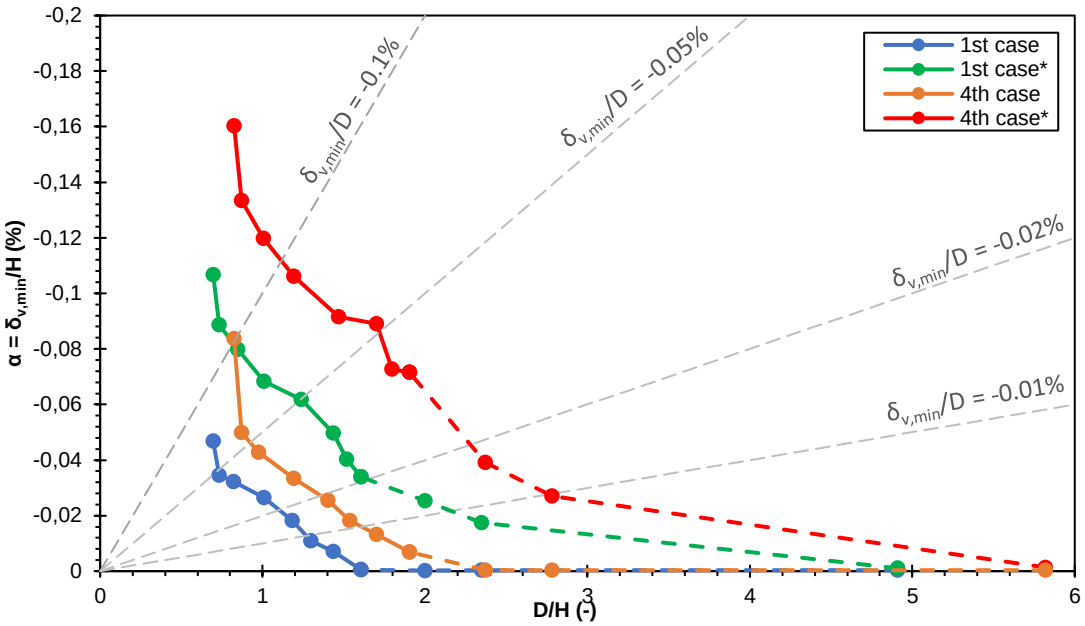

*Figure 7.6 Vertical ground surface movement against normalised diameter due to excavation cases between Section 7.2 and 7.4 (*Study cases of Section 7.2)*

8 Conclusions

Until recently there were few well-documented case studies of circular shafts, which made it difficult to estimate their impact in terms of ground movements. This work contributes to that by using the Limmo Peninsula Tunnelling Case study documented in Newhouse (2017) and expanding its information with numerical analyses.

A review of the state of the art regarding soil movements due to shaft construction is presented first in this document. Moreover, an introduction and description of the governing differential equations is presented and the advanced constitutive models used to describe overconsolidated clay deposits implemented in the commercial software PLAXIS are presented.

Within this work the Limo Peninsula shaft excavation case study has been correctly reproduced using the software PLAXIS 2D, using the Hardening Soil Models implemented in Plaxis and adopting the constitutive parameters from M. Chandegra and A. Kokkinou (2016).

On the one hand, the results show that the auxiliary shaft has been accurately reproduced including the dewatering sequence adopted on site that allowed the excavation of the shaft. On the other hand, the main shaft behaviour has not been possible to reproduce. This fact leads to conclude that is very difficult to estimate the behaviour of the soil in small strains and also the fact of the limitation of the axisymmetric model that cannot accurately reproduce the installation of a diaphragm wall (i.e. excavating a single panel with the consequent relaxation of the soil). Also highlights the difficulties of modelling the behaviour of the soil with wished-in-place plate elements with PLAXIS. A 3D model would be more suitable for this particular case.

For the unsupported excavation shaft (i.e. auxiliary shaft) the finite element method is capable of describing the behaviour observed on site, as the construction methodology has been accurately reproduced.

Further to that and using the design lines provided by Newhouse (2017), the sensitivity on ground movements due shaft diameter, supported and unsupported excavation, depth and overall depth of the shaft is studied. This will contribute to expand the data base on numerical case studies to further validate the new proposed lines in Newhouse (2017).

It has been found that the diameter is the key parameter that affects the vertical displacement of circular shafts. Further to that, it is noted that the SCL construction procedure and the total depth do not appear to be a critical component affecting the vertical soil displacements.

As expected, it has been observed that the water acting behind the wall also affects the displacements observed during excavation. Dewatering would reduce the ground displacements due to excavation. In addition to that, displacements will occur due to change in the groundwater regime; also when the dewatering system is turned off, the water level will be

recovered to original levels and the water pressure behind the wall can increase the ground movements.

The sheet pile length will reduce ground movements during the excavation progress compared to the generated by the SCL method. However, close to the end of the sheet pile excavation, larger displacements will appear.

Moreover, it has been found that upholding a constant normalised diameter by the excavation depth but with different shaft geometry have similar trends as studied before. As higher diameter has the shaft, higher vertical ground movement and higher settlements normalised by the shaft excavation depth.

During the preparation of this work, some expected limitations of using a 2D Axisymmetric model have been highlighted. Further work could be undertaken in order to model in a 3D model the geometry of the two shafts, accurately modelling the dewatering system installed in the area (as information is public) and generating and expanding the data base for circular shaft excavation in overconsolidated clay deposits.

Finally, all cases seem to adopt an exponential logarithmic behaviour; however, they are very dependent on construction methodology. Further work is proposed in order to be able to calibrate exponential logarithmic lines to provide design guidelines for the intermediate stages of excavation.

References

AETOS. (2014). Diseño, fabricación y puesta en obra del hormigón proyectado en obras subterráneas. *Ref. Documento: AETOS WG 6 Hormigón Proyectado v.01-00.*

ArchelorMittal. (2018). ArcelorMittal Sheet Pilling. Steel Foundation Solutions *(02.2018 ed.).*

Braja, M. D. (1994). Principles of Geotechnical Engineering. *PWS Publishing Company, 1994.*

Chandegra, M. & Kokkinou A. (2016). Design of the deep cut and cover Crossrail Paddington Station using Finite Element Method. *Crossrail Learning Legacy*.

Duncan, J. M. & Chang, C. Y. (1970). Nonlinear analysis of stress and strain in soil, J. Soil Mech. Found. Div.

Gaba, A., Hardy, S., Doughty, L., Powrie, W. & Selemetas, D. (2017). Guidance on embedded retaining wall design. *London: CIRIA. Report number: C760 (Reference extracted from Newhouse 2017, original source has not been reviewed as those are unpublished internal technical reports)*.

Gaba, A., Simpson, B., Powrie, W. & Beadman, D. (2003). Embedded retaining walls - guidance for economic design. *London: CIRIA. Report number: C580 (Reference extracted from Newhouse 2017, original source has not been reviewed as those are unpublished internal technical reports).*

Gasparre, A. (2005). Advance laboratory characterisation of London Clay. *PhD. Imperial College London.*

GCG. (2007). Settlement Estimation Procedure: Box Excavations & Shafts. B London, Crossrail. *Report number: 1D0101-G0G00-01004 (Reference extracted from Newhouse 2017, original source has not been reviewed as those are unpublished internal technical reports).*

Hejazi, Y., Dias, D. & Kastner, R. (2008). Impact of constitutive models on the numerical analysis of underground constructions. *Acta Geotechnica (2008) 3:251–258. doi:10.1007/s11440-008-0056-1*

Jiang, S. & Thomas, A. (2015). Design of sprayed concrete lining in soft ground – a Crossrail perspective .

London Underground. (2014). Civil Engineering - Technical Advice Notes. *A20 Report number: G0058 (Reference extracted from Newhouse 2017, original source has not been reviewed as those are unpublished internal technical reports)*.

Mott MacDonald. (2013). Impacts of Tunnels in the UK. London, HS2. *(Reference extracted from Newhouse 2017, original source has not been reviewed as those are unpublished internal technical reports).*

New, B. M. & Bowers, K. H. (1994). Ground movement model validation at the Heathrow Express trial tunnel. *Tunnelling '94, pp. 301-329.*

Newhouse, J. (2017). Ground movement due to shaft construction. *MSc. Imperial College London.*

Obrzud, R. F. (n.d.). On the use of the Hardening Soil Small Strain model in geotechnical practice.

Oliver, X., & Agelet de Saracíbar, C. (2000). Mecánica de Medios Continuos para Ingenieros. *Barcelona: Edicions UPC.*

Pairaudeau, H. (2011). Construction and Performance of Shafts. *MEng. University of Cambridge. (Reference extracted from Newhouse 2017, original source has not been reviewed as those are unpublished internal technical reports)*.

Peck, R. B. (1969). Deep excavations and tunneling in soft ground. *Proceeding of 7th conference on soil mechanics and foundation engineering. Mexico City: State of-the-Art Volume, pp. 225–290, 1969*

Plaxis. (2018). PLAXIS 2D Manuals.

Schanz, T., Vermeer, P. A. & Bonnier, P. G. (1999). The hardening soil model: Formulation and verification.

Schwamb, T. (2014). Performance Monitoring and Numerical Modelling of a Deep Circular Excavation. *PhD. University of Cambridge.*

Simpson, B., Burland, J. B. & St. John, H. D. (1979). Movements around excavations in London Clay.

Terzaghi, K. & Peck, R.B. (1948). Soil mechanics in engineering practice. *New York.*

Annexes

A Annex: Main Shaft and Auxiliary Shaft analysis

Introduction

In this Annex, the Main Shaft and Auxiliary Shaft construction (the installation, the excavation and the dewatering phases) to reproduce the models in PLAXIS 2D is presented as a kind of tutorial. Also, the deformed mesh, the Cartesian total stresses, the effective mean stress (p'), the deviatoric stress (q), the total deviatoric strain (γ_s) and the pore water pressure is presented for each shaft.

Main Shaft

Construction Stages

This section will focus on the construction stages only. The geometry, the boundary conditions, the mesh and the materials for the Main Shaft are introduced in the software, as described in Section 5.2 and 5.4. Figure A.1 shows a few stages to reproduce the model of the Main Shaft, there is one stage for each cluster is removed. Figure A.1 (a) and (b) show the initial stage and the diaphragm wall installation. Figure A.1 (c), (d) and (e) presents a few excavation stages until the end of the excavation, Figure A.1 (f).

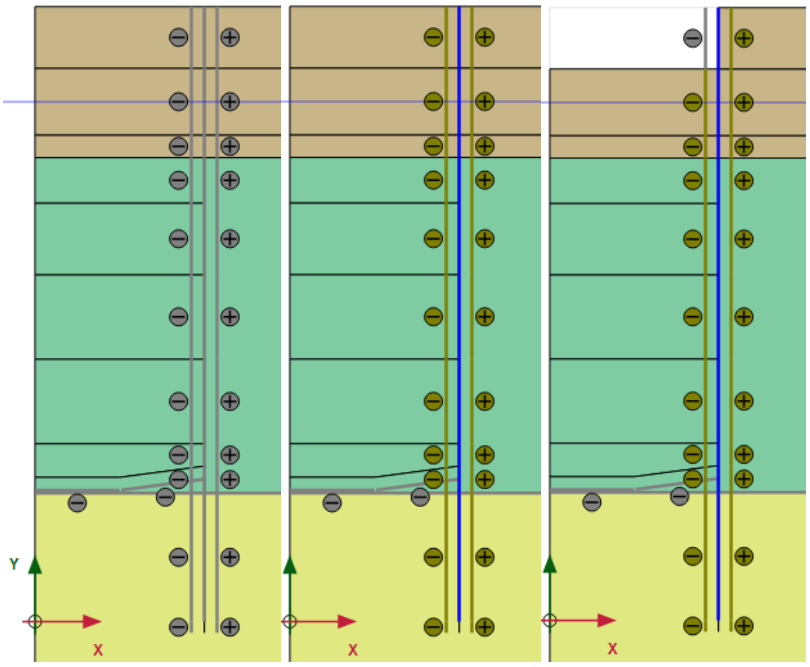

(a) (b) (c)

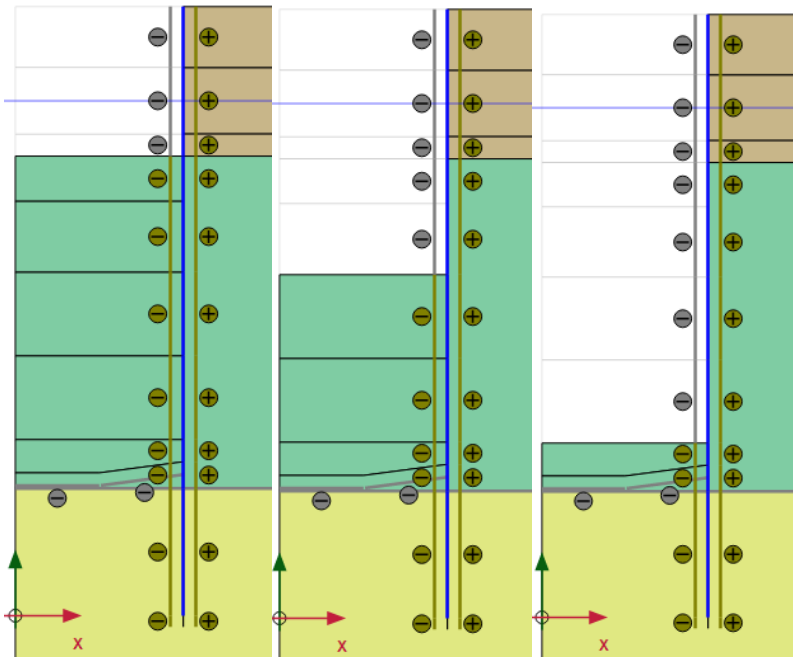

(d) (e) (f)

Figure A.1 Excavation stages of the Main Shaft

Figure A.2 shows the *Flow Conditions*, It has been created a dewatering stage before every excavation stage and it has been defined a groundwater head for the drains from Figure 4.2 and Figure 5.6. It can be seen that the groundwater flow is closed in the left boundary along the vertical contour (where is located the symmetry axis) and open in the right boundary along the vertical contour.

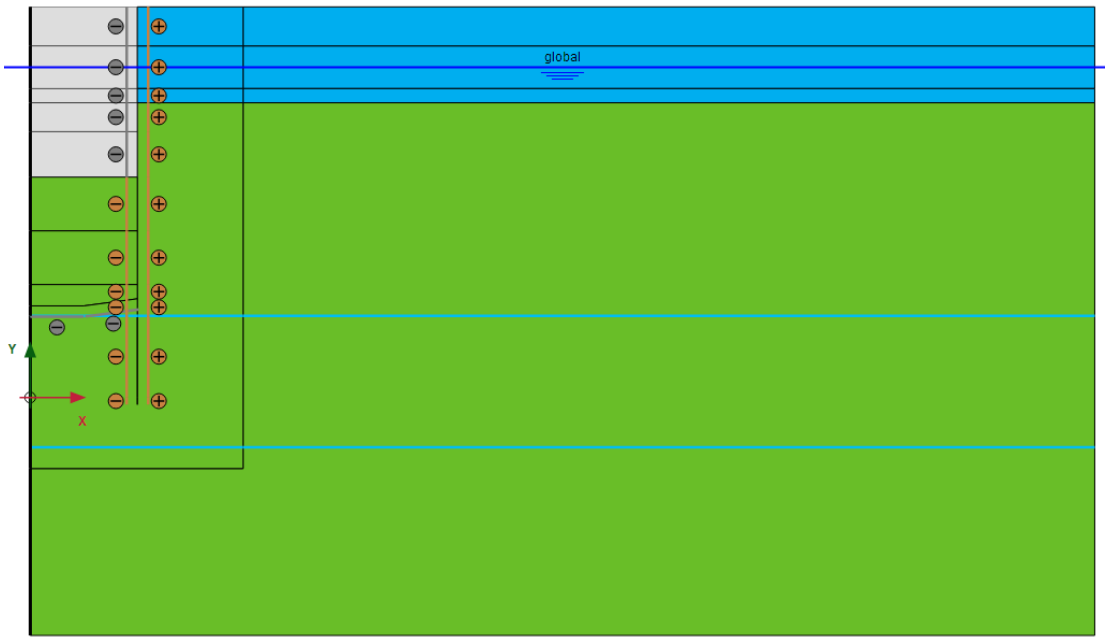

Figure A.2 Flow conditions for each dewatering stage from the Main Shaft

Deformed mesh

Figure A.3 and A.4 show the deformed mesh on an intermediate stage and on the final stage, respectively. Wherein the ground movement is produced by the changes on the groundwater level.

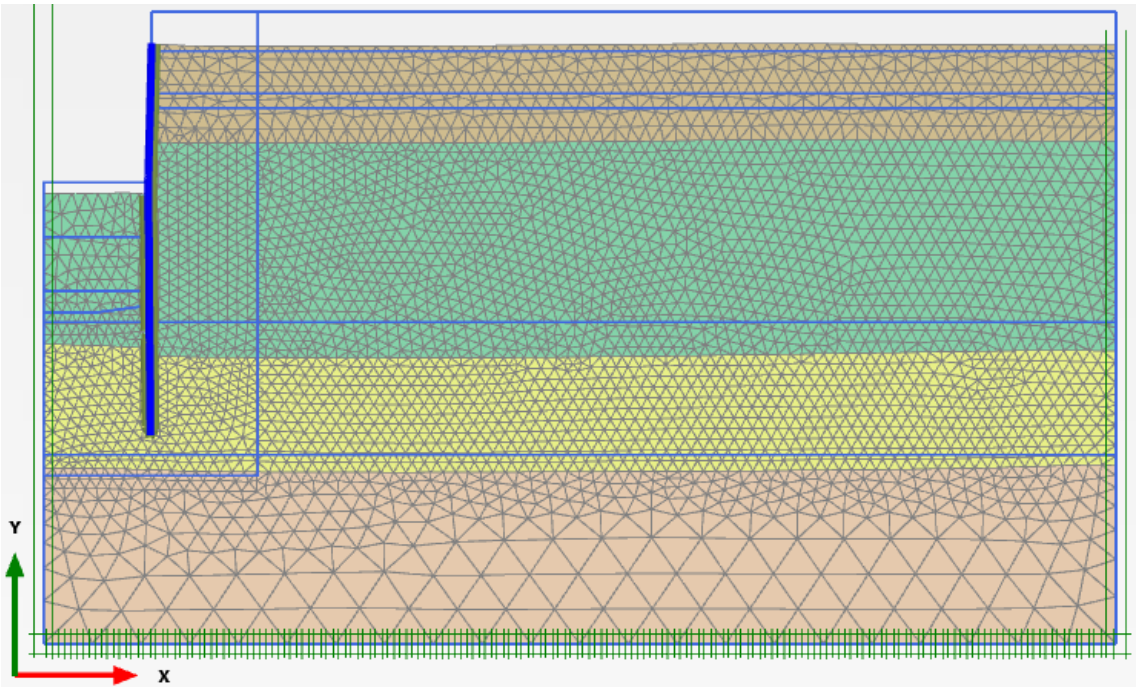

Figure A.3 Deformed mesh |u| on an intermediate stage (scaled up 200 times). Max. value = 0.02567 m

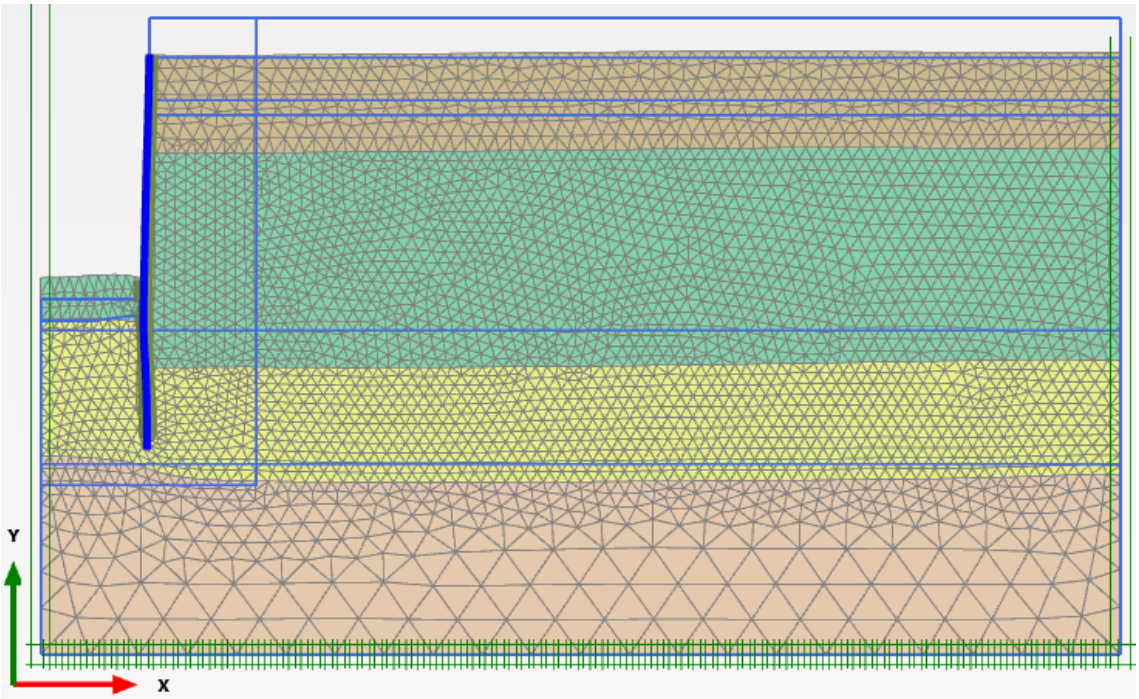

Figure A.4 Deformed mesh |u| after the excavation ends (scaled up 200 times). Max. value = 0.02739 m

Cartesian total stresses

It can be seen the vertical total stress, σ_{yy}, on an intermediate stage and after the excavation ends, Figure A.5 and A.6. Wherein, the vertical total stress varies on the passive side of the wall. Compressions are negative in PLAXIS.

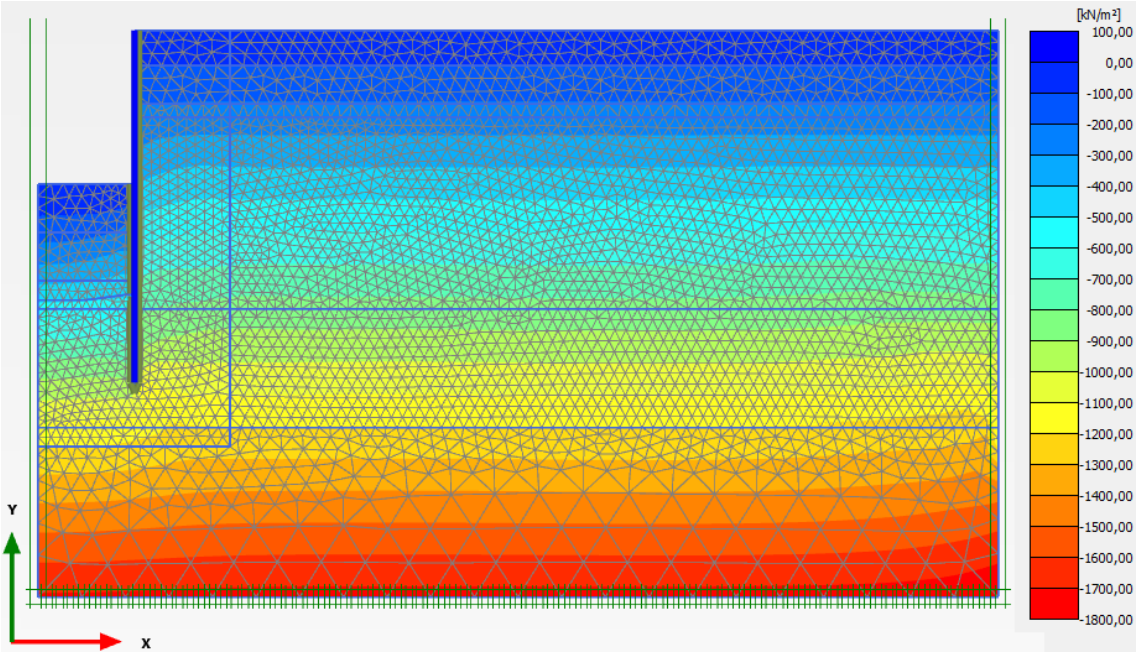

Figure A.5 Vertical total stress σ_{yy} on an intermediate stage (scaled up $2E^{-3}$ times).
Max. value (blue, positive) = 1.120 kN/m² and Min. value (red, negative) = -1788 kN/m²

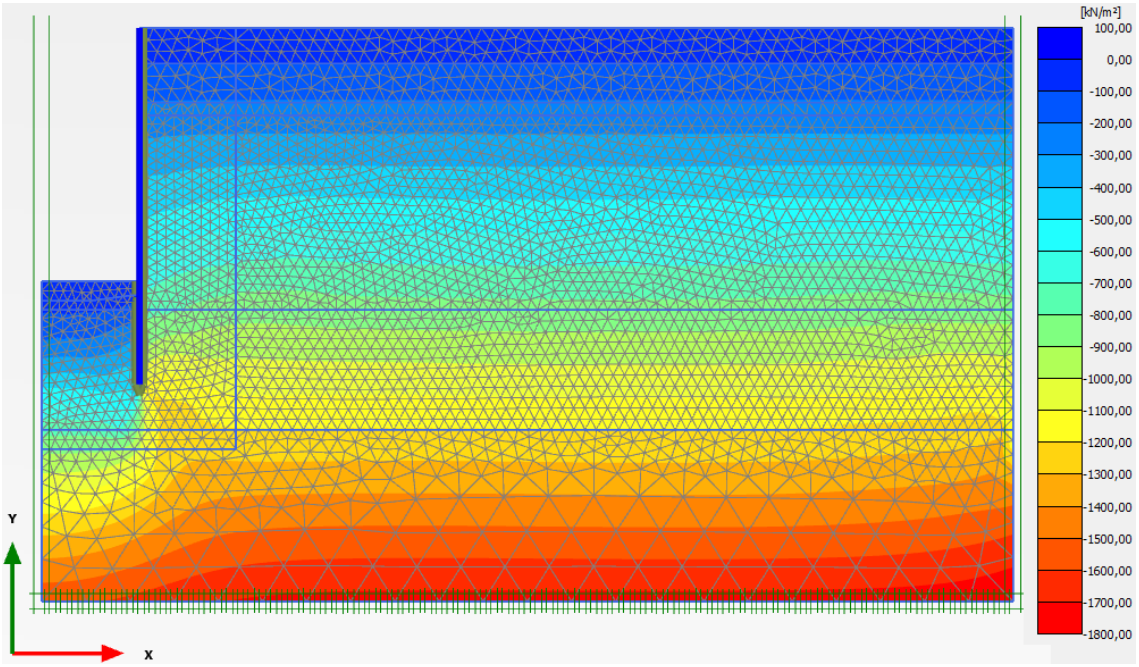

Figure A.6 Vertical total stress σ_{yy} after the excavation ends (scaled up $2E^{-3}$ times).
Max. value (blue, positive) = 9.041 kN/m² and Min. value (red, negative) = -1788 kN/m²

Figure A.7 and A.8 show the horizontal total stress, σ_{xx}, on an intermediate stage and after the excavation ends.

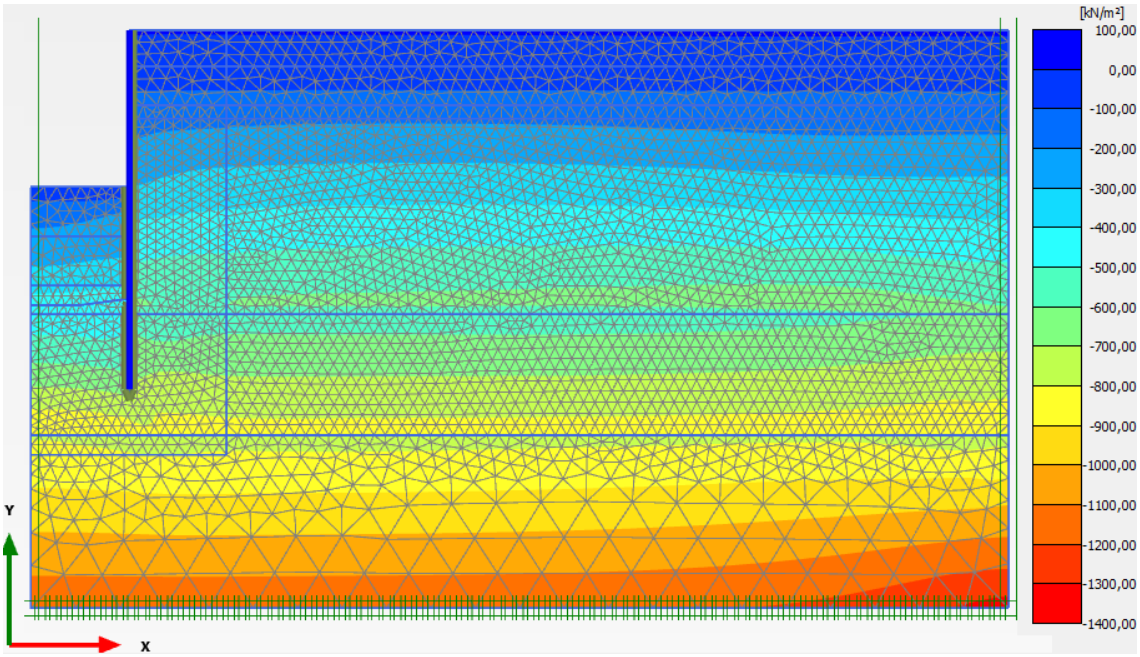

Figure A.7 Horizontal total stress σ_{xx} on an intermediate stage (scaled up $2E^{-3}$ times). Max. value (blue, positive) = 12.35 kN/m² and Min. value (red, negative) = -1350 kN/m²

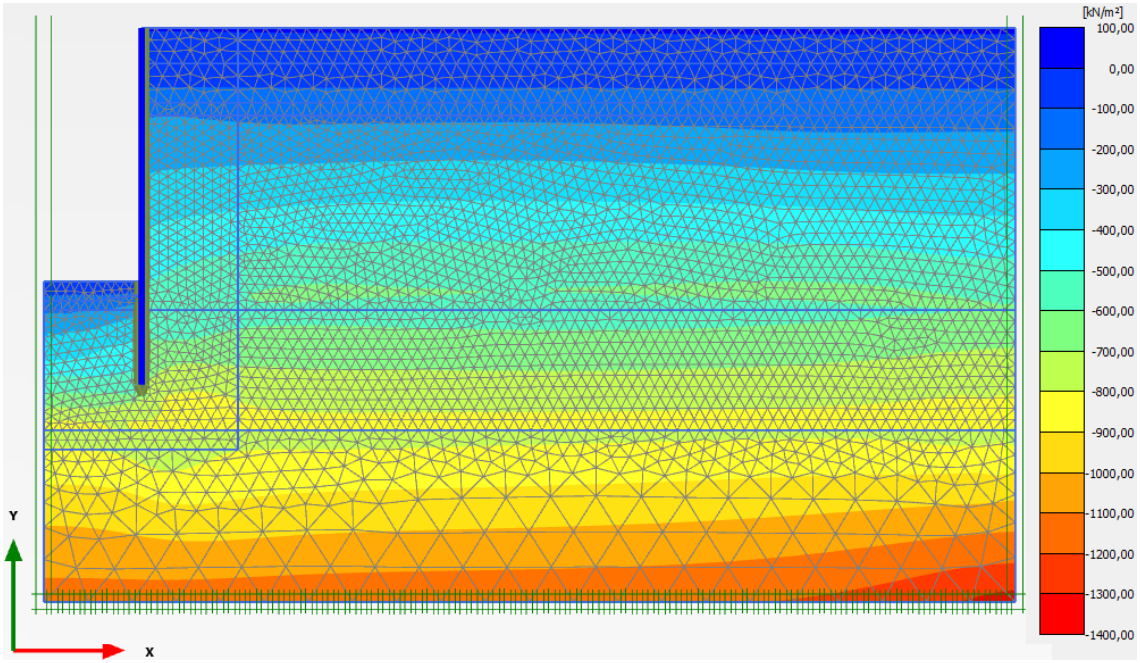

Figure A.8 Horizontal total stress σ_{xx} after the excavation ends (scaled up $2E^{-3}$ times). Max. value (blue, positive) = 10.90 kN/m² and Min. value (red, negative) = -1350 kN/m²

Effective mean stress and deviatoric stress

Figure A.9 and A.10 show the effective mean stress, p', on an intermediate stage and after the excavation ends.

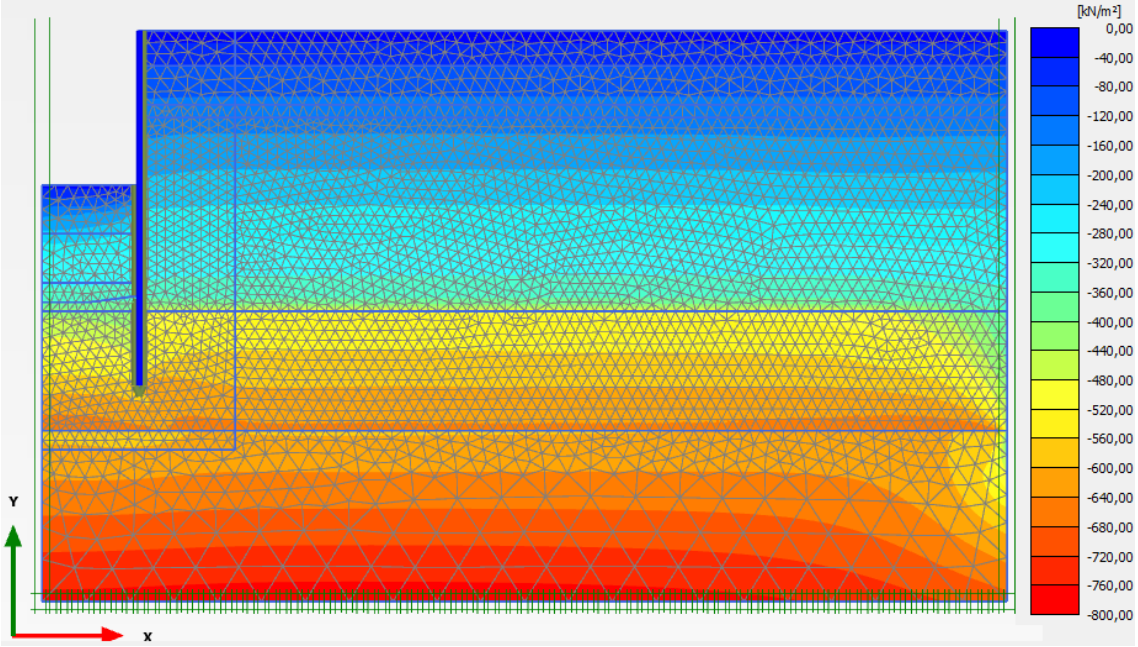

Figure A.9 Effective mean stress p' on an intermediate stage (scaled up $5E^{-3}$ times).
Max. value (blue, negative) = -11.62 kN/m² and Min. value (red, negative) = -782.0 kN/m²

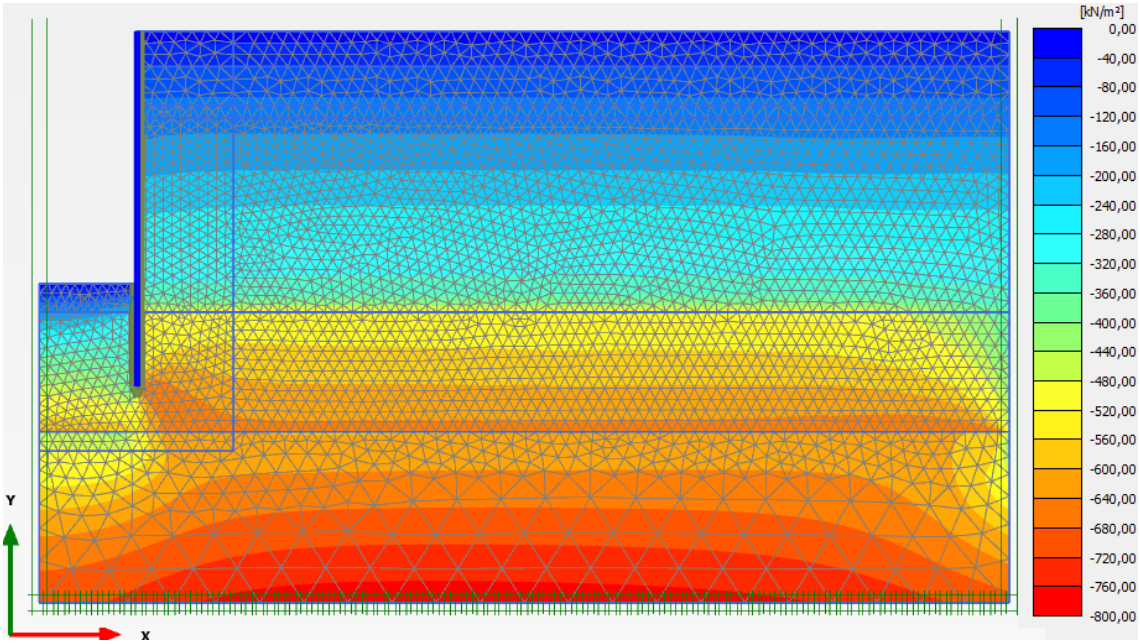

Figure A.10 Effective mean stress p' after the excavation ends (scaled up $5E^{-3}$ times).
Max. value (blue, negative) = -7.55 kN/m² and Min. value (red, negative) = -784.2 kN/m²

It can be seen the deviatoric stress, q, on an intermediate stage and after the excavation ends, Figure A.11 and A.12.

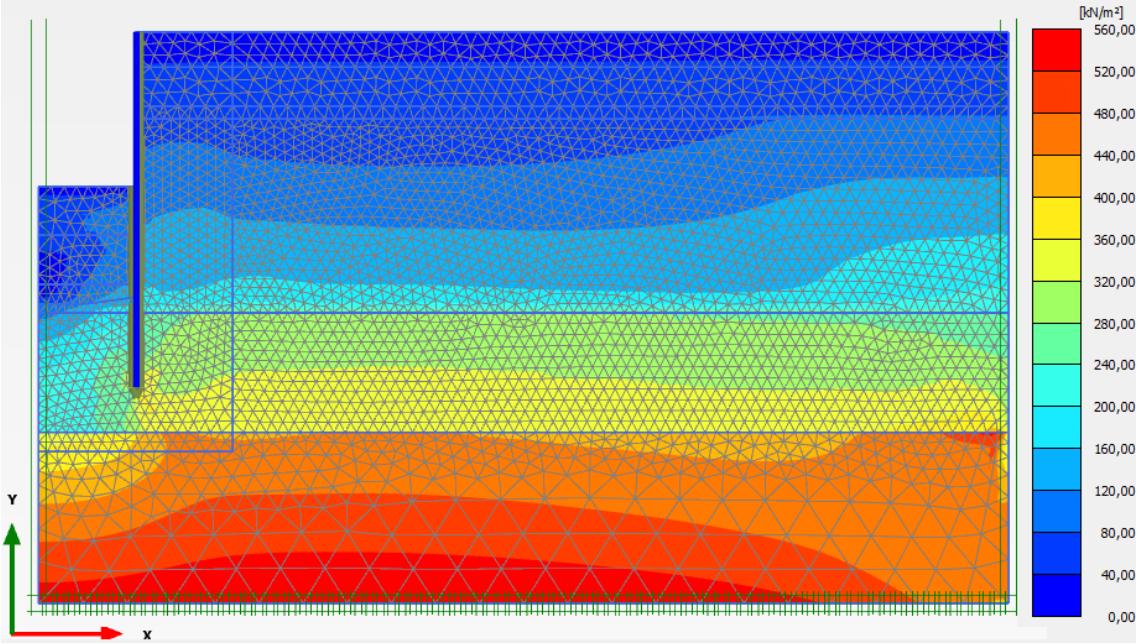

Figure A.11 Deviatoric stress q on an intermediate stage (scaled up $5E^{-3}$ times).
Max. value (red, positive) = 553.6 kN/m² and Min. value (blue, positive) = 1.345 kN/m²

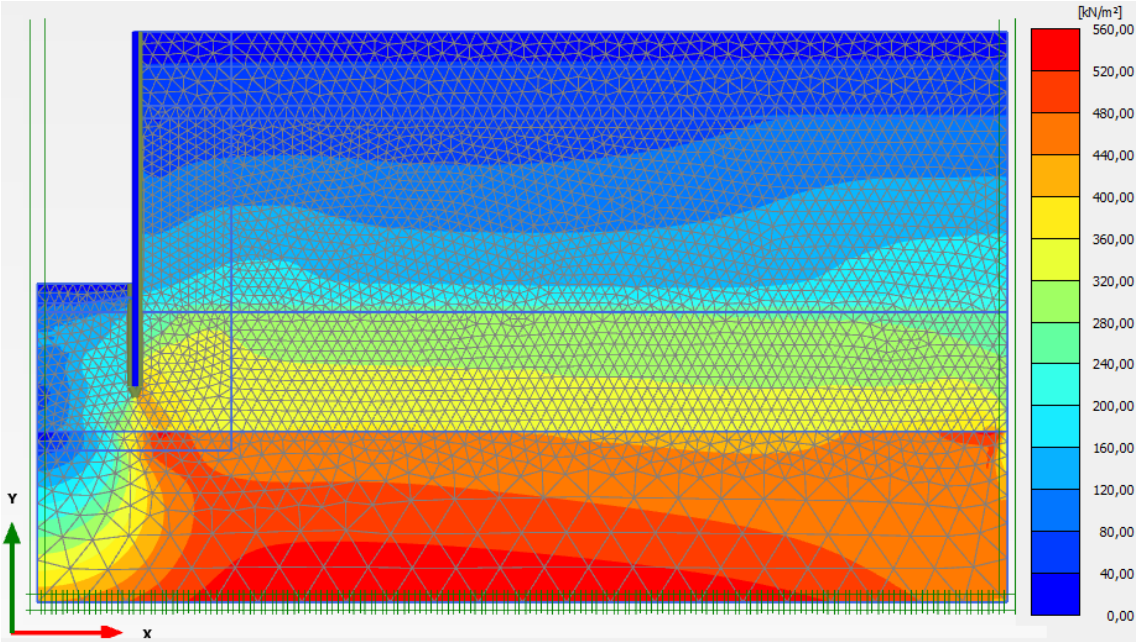

Figure A.12 Deviatoric stress q after the excavation ends (scaled up $5E^{-3}$ times).
Max. value (red, positive) = 559.0 kN/m² and Min. value (blue, positive) = 4.321 kN/m²

Total deviatoric strain

Figure A.13 and A.14 show the total deviatoric strain, γ_s, on an intermediate stage and after the excavation ends. It can be seen that maximum total deviatoric strain is generated behind the diaphragm wall and on the shaft excavation surface closer to the lining wall in a small zone. Deviatoric strains are small in these cases.

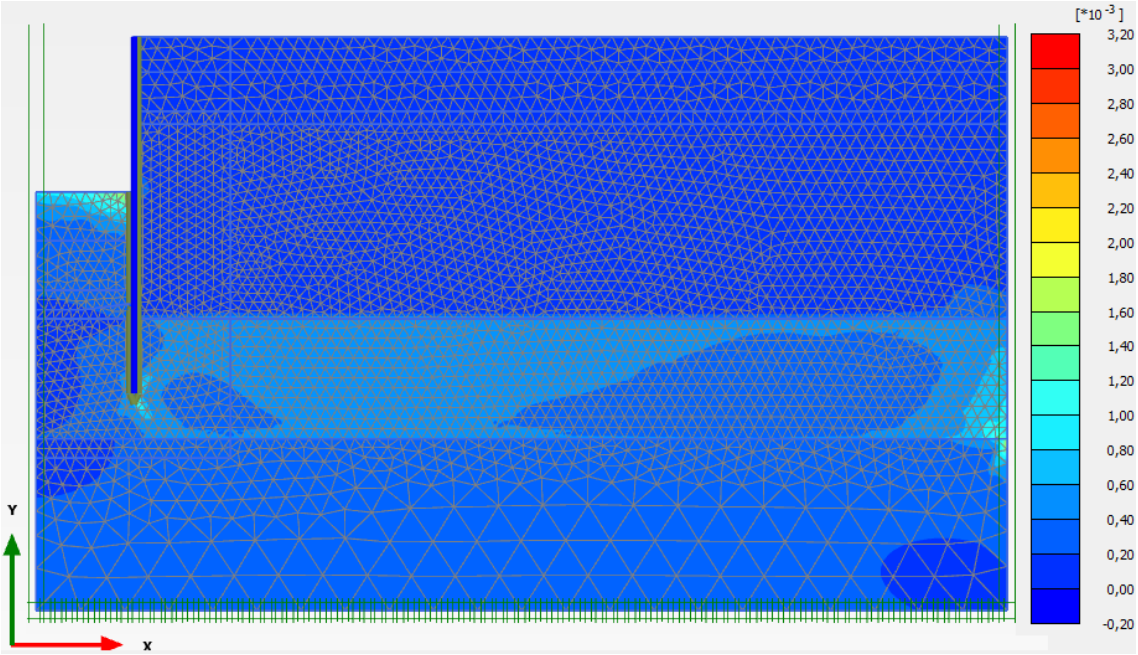

Figure A.13 Total deviatoric stain γ_s on an intermediate stage (scaled up 200 times). Max. value (blue, positive) = 3.172E^{-3} and Min. value (red, positive) = 1.162E^{-6}

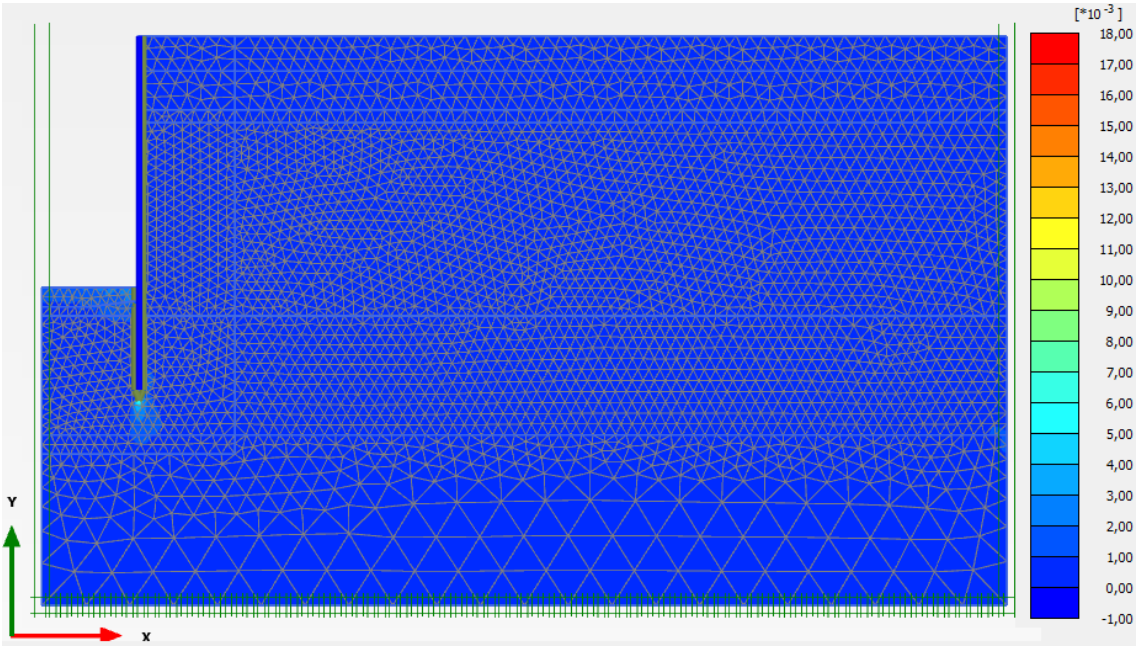

Figure A.14 Total deviatoric stain γ_s after the excavation ends (scaled up 200 times). Max. value (blue, positive) = 0.01765 and Min. value (red, positive) = 0.7762E^{-6}

Groundwater pressure

Figure A.13 and A.14 show the pore water pressure, p_{water}, on an intermediate stage and after the excavation ends. It can be seen that the pore water pressure on the passive side of the wall is increasing during the excavation progress.

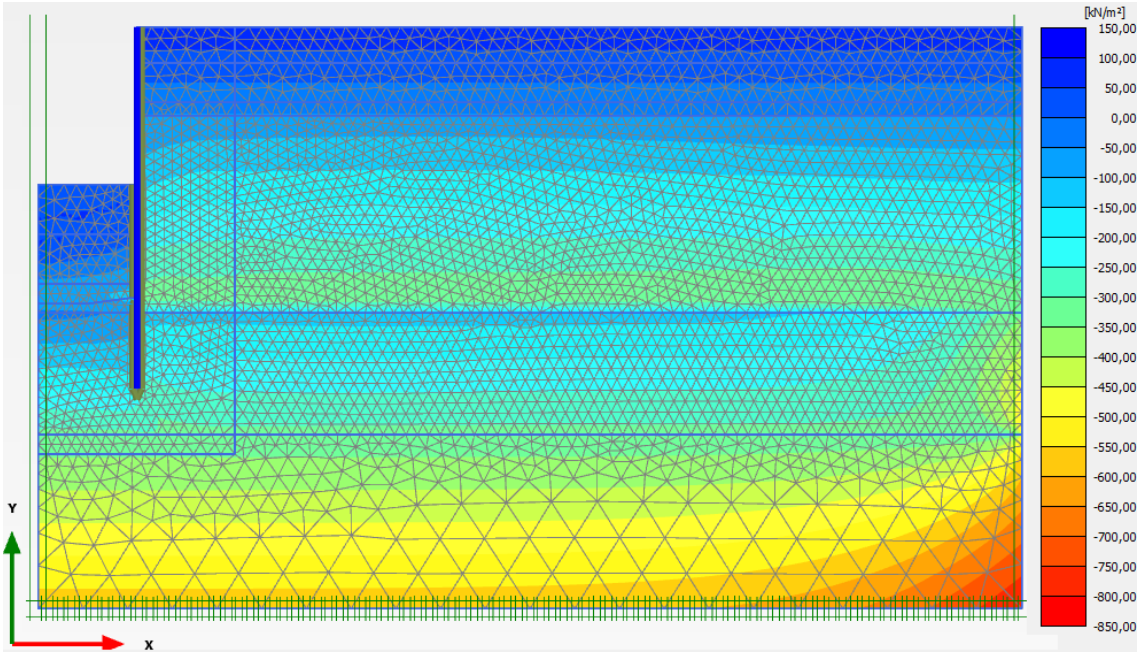

Figure A.15 Pore water pressure p_{water} on an intermediate stage (scaled up $5E^{-3}$ times) (Pressure = negative). Max. value (blue, positive) = 100.0 kN/m² and Min. value (red, negative) = -800 kN/m²

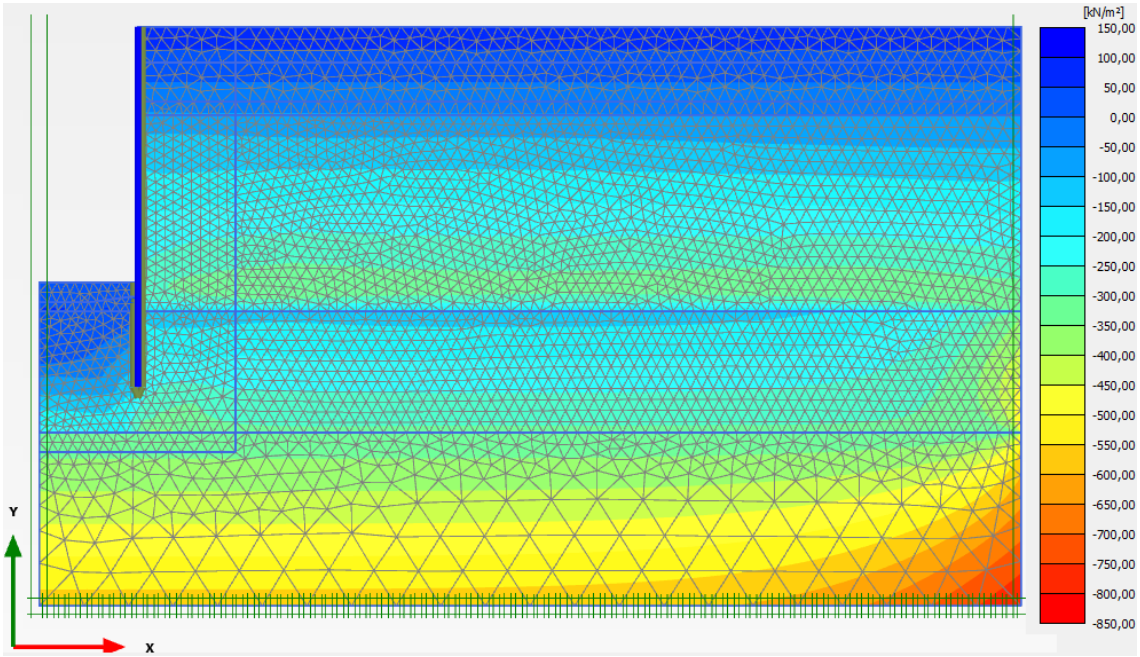

Figure A.16 Pore water pressure p_{water} after the excavation ends (scaled up $5E^{-3}$ times) (Pressure = negative). Max. value (blue, positive) = 100.0 kN/m² and Min. value (red, negative) = -800 kN/m²

Auxiliary Shaft

Construction Stages

As described in Section 5.3 and 5.4, the geometry, the boundary conditions, the mesh and the materials are introduced in the software. Figure A.17 shows a few stages to reproduce the model of the Auxiliary Shaft, there is one stage for each cluster that is removed. Figure A.17 (a) and (b) presents the initial stage and the sheet pile installation. Figure A.17 (c) and (d) shows the sheet

pile excavation. After finishing the excavation protected by the sheet pile, the Sprayed Concrete Lining starts. As described in Section 5.4, the SCL has different properties that depends on time, Figure A.17 (e), (f), (g) and (h) shows the SCL development, where the yellow line (Initial Young) are the material properties after 0.25 days; the blue line (Primary Young), after 0.625 days and the red line (Primary Old), after 28 days. Figure A.18 shows the stage after the excavation ends.

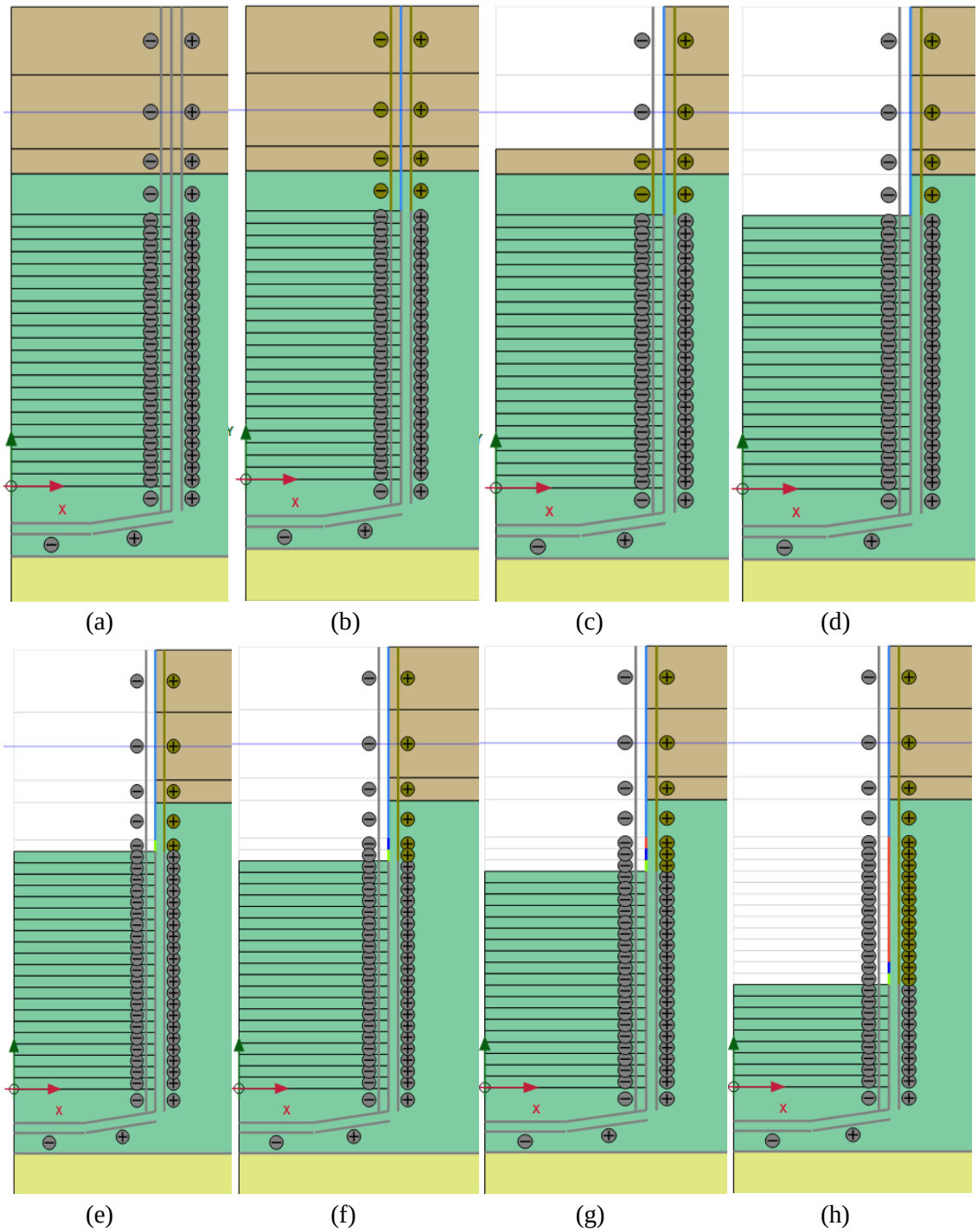

Figure A.17 Excavation stages of the Auxiliary Shaft

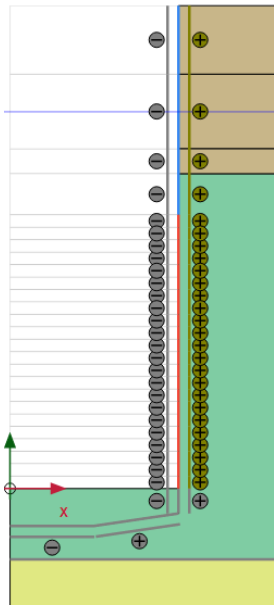

Figure A.18 Stage after the Auxiliary Shaft excavation ends

As described in Main Shaft Section in the Annex 1, it has been created a dewatering stage, Figure A.19 shows the *Flow Conditions*, before every excavation stage and it has been defined a groundwater head for the drains from Figure 4.2 and Figure 5.6. It can be seen that the groundwater flow is open on the right boundary along the vertical contour and closed on the left boundary along the vertical contour (where is located the symmetry axis).

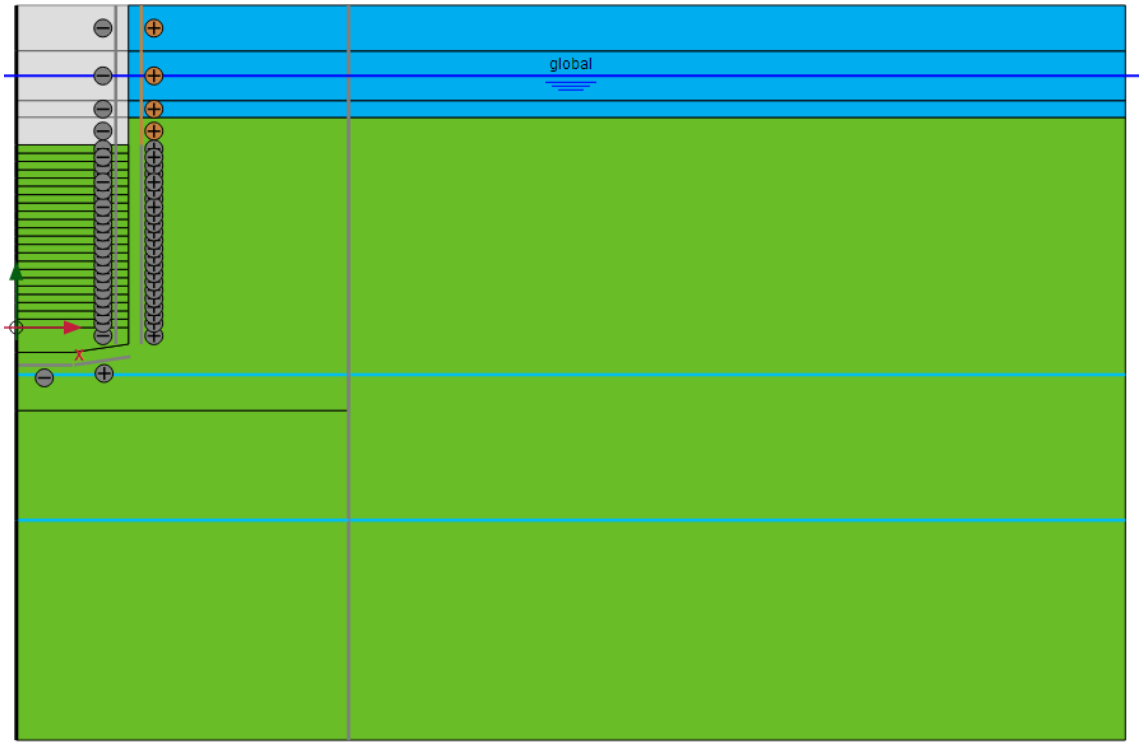

Figure A.19 Flow conditions for each dewatering stage from the Auxiliary Shaft

Deformed mesh

Figure A.20 and A.21 show the deformed mesh on an intermediate stage (transition from sheet pile wall to SCL) and on the final stage, respectively. Wherein the ground movement is produced by the changes on the groundwater level. Moreover, the ground movement after the excavation ends is clearly generate by the shaft excavation.

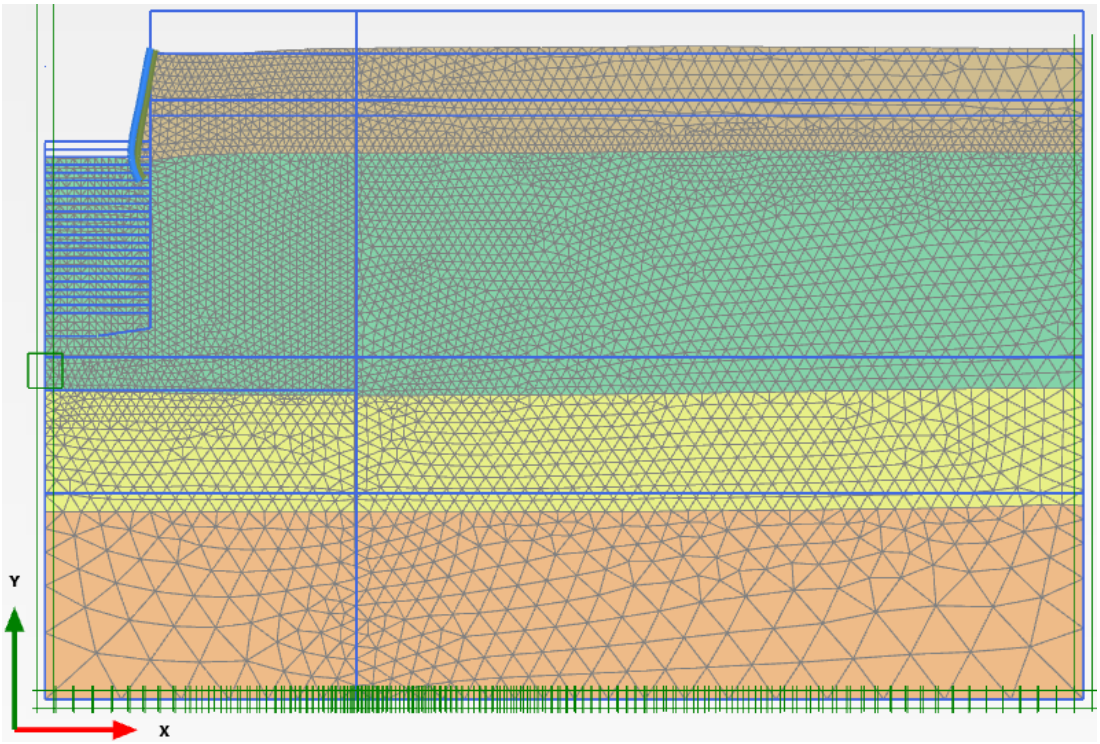

Figure A.20 Deformed mesh |u| on an intermediate stage (scaled up 200 times). Max. value = 0.03081 m

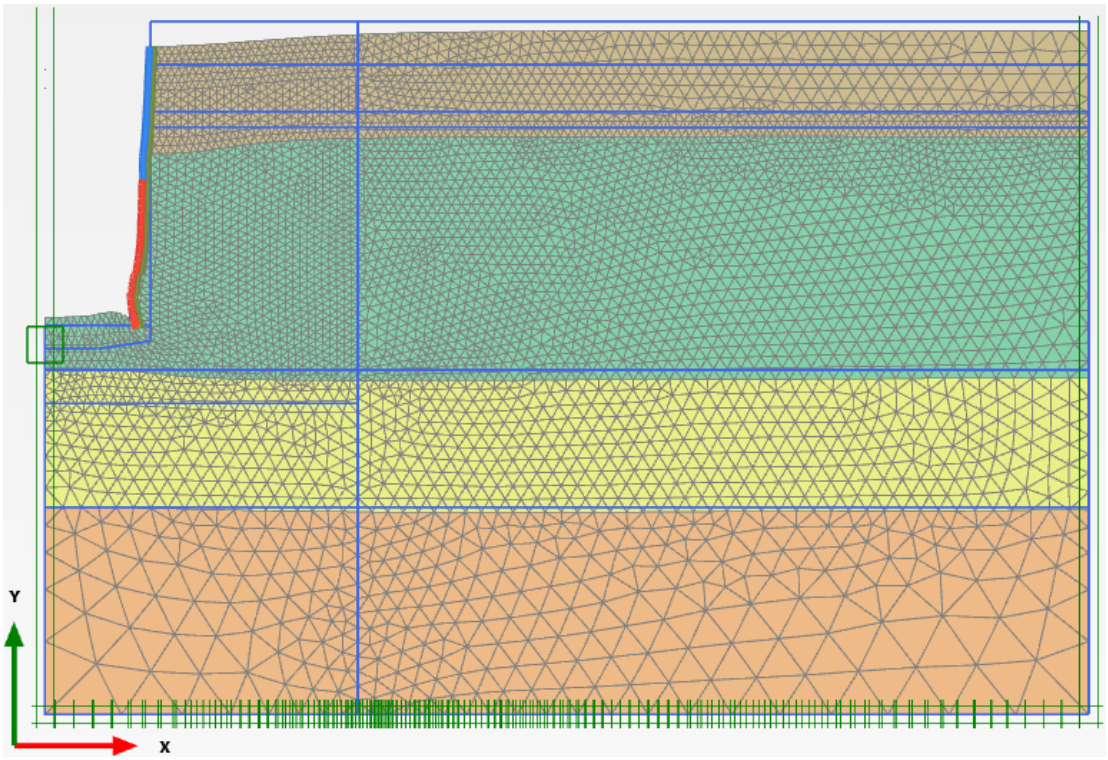

Figure A.21 Deformed mesh |u| after the excavation ends (scaled up 50 times). Max. value = 0.07009 m

Cartesian total stresses

It can be seen the vertical total stress, σ_{yy}, on an intermediate stage and after the excavation ends, Figure A.22 and A.23. Wherein, the vertical total stress varies on the passive side of the wall as described on Main Shaft Section.

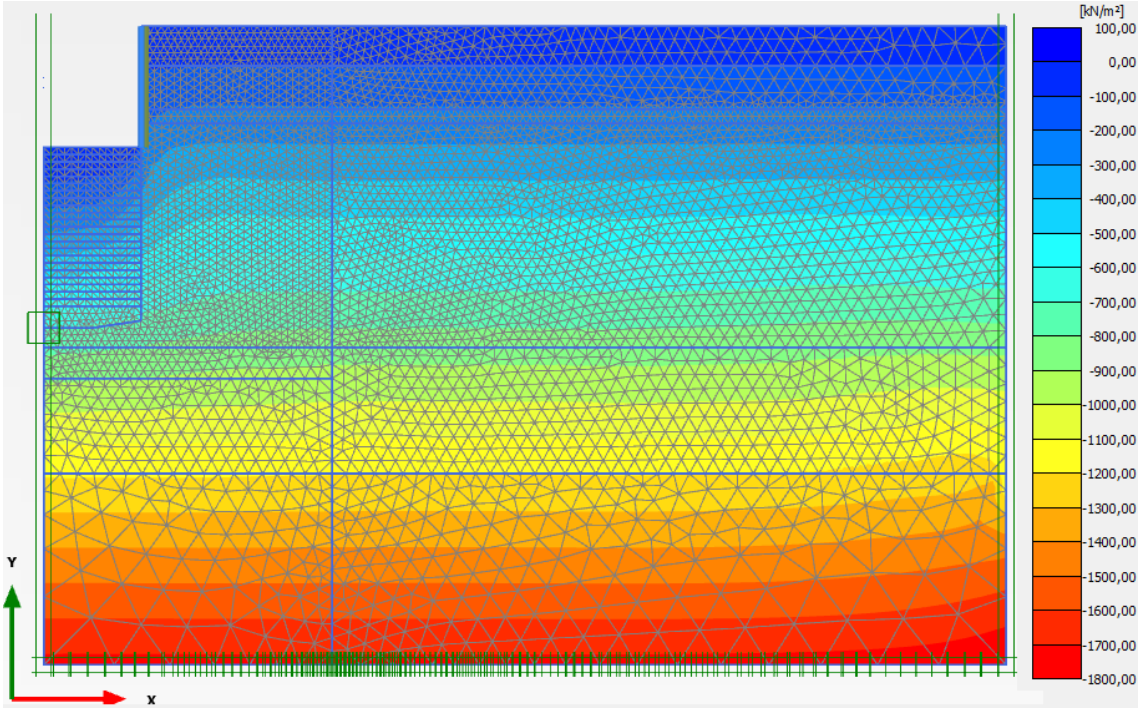

Figure A.22 Vertical total stress σ_{yy} on an intermediate stage (scaled up $2E^{-3}$ times).
Max. value (blue, positive) = 1.974 kN/m² and Min. value (red, negative) = -1790 kN/m²

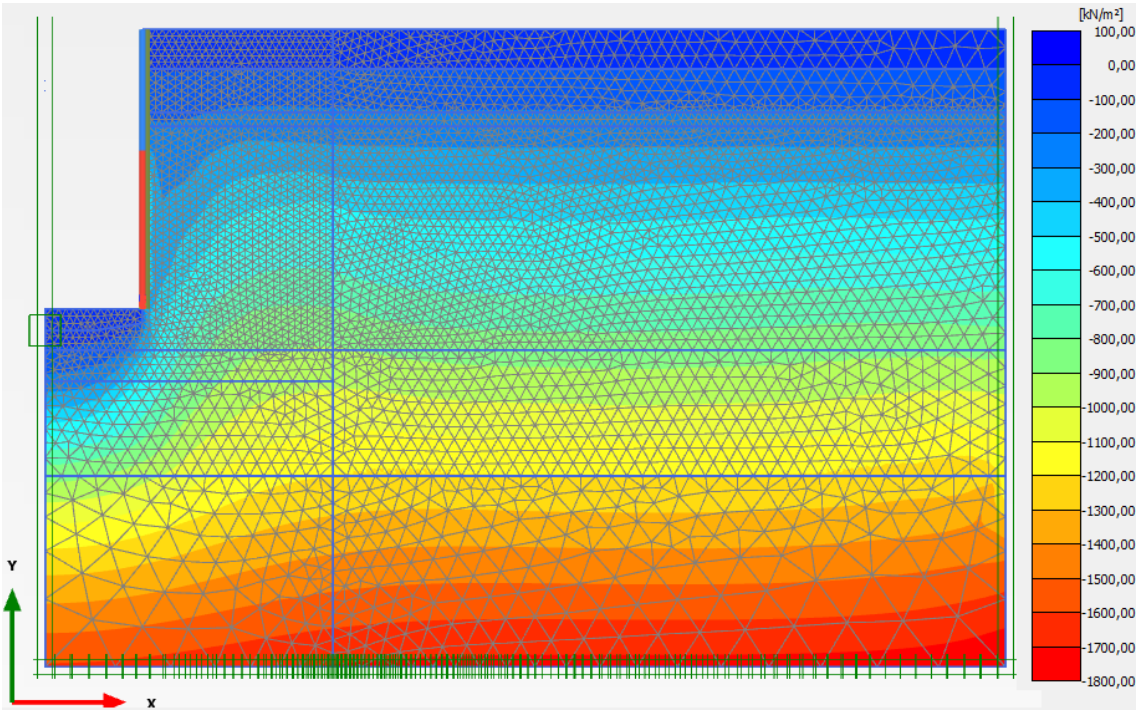

Figure A.23 Vertical total stress σ_{yy} after the excavation ends (scaled up $2E^{-3}$ times).
Max. value (blue, positive) = 6.139 kN/m² and Min. value (red, negative) = -1793 kN/m²

Figures A.24 and A.25 show the horizontal total stress, σ_{xx}, on an intermediate stage and after the excavation ends.

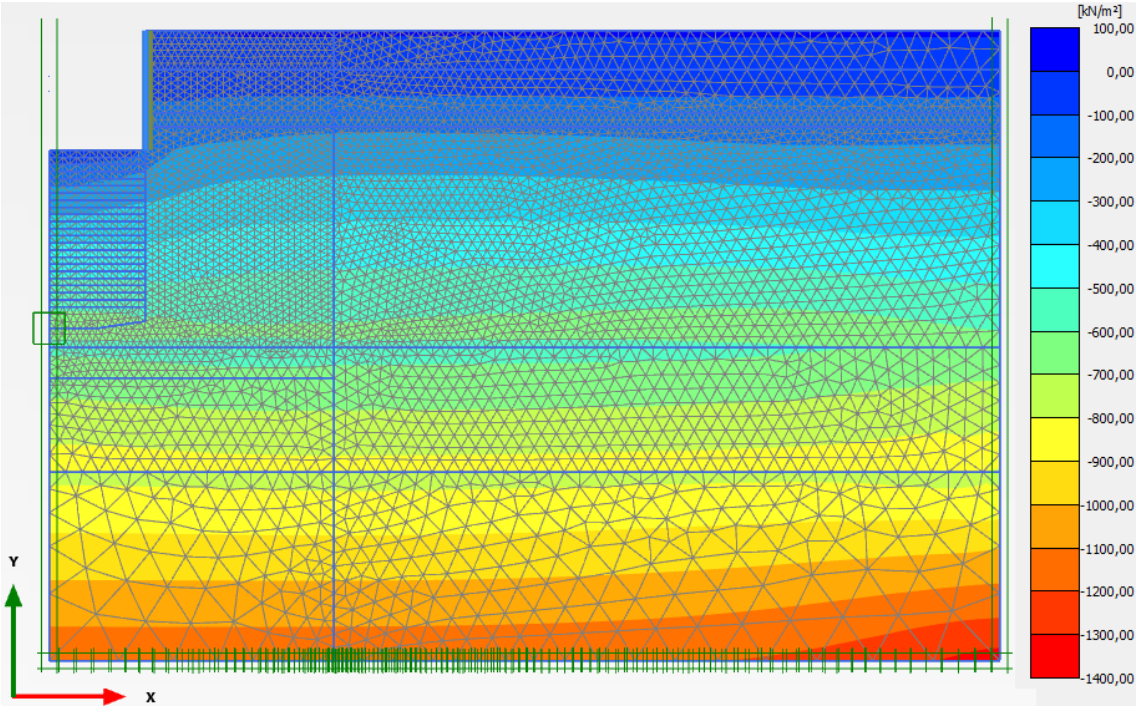

Figure A.24 Horizontal total stress σ_{xx} on an intermediate stage (scaled up $2E^{-3}$ times). Max. value (blue, positive) = 11.67 kN/m² and Min. value (red, negative) = -1349 kN/m²

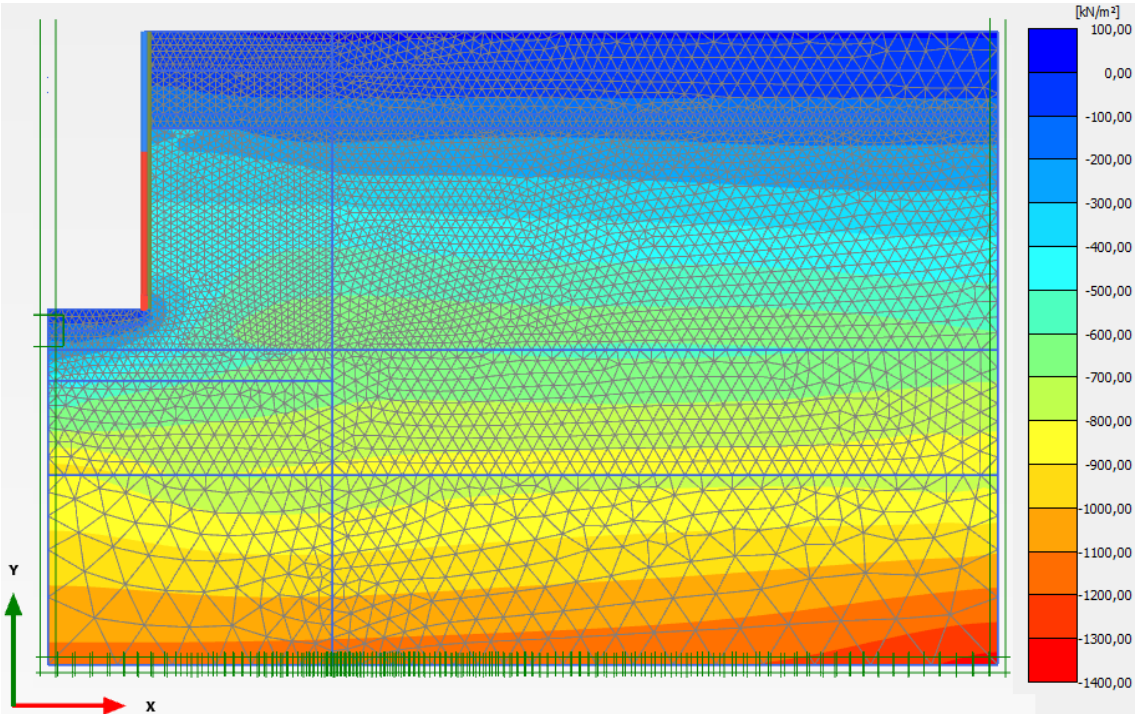

Figure A.25 Horizontal total stress σ_{xx} after the excavation ends (scaled up $2E^{-3}$ times). Max. value (blue, positive) = 16.05 kN/m² and Min. value (red, negative) = -1350 kN/m²

Effective mean stress and deviatoric stress

Figure A.26 and A.27 show the effective mean stress, p', on an intermediate stage and after the excavation ends

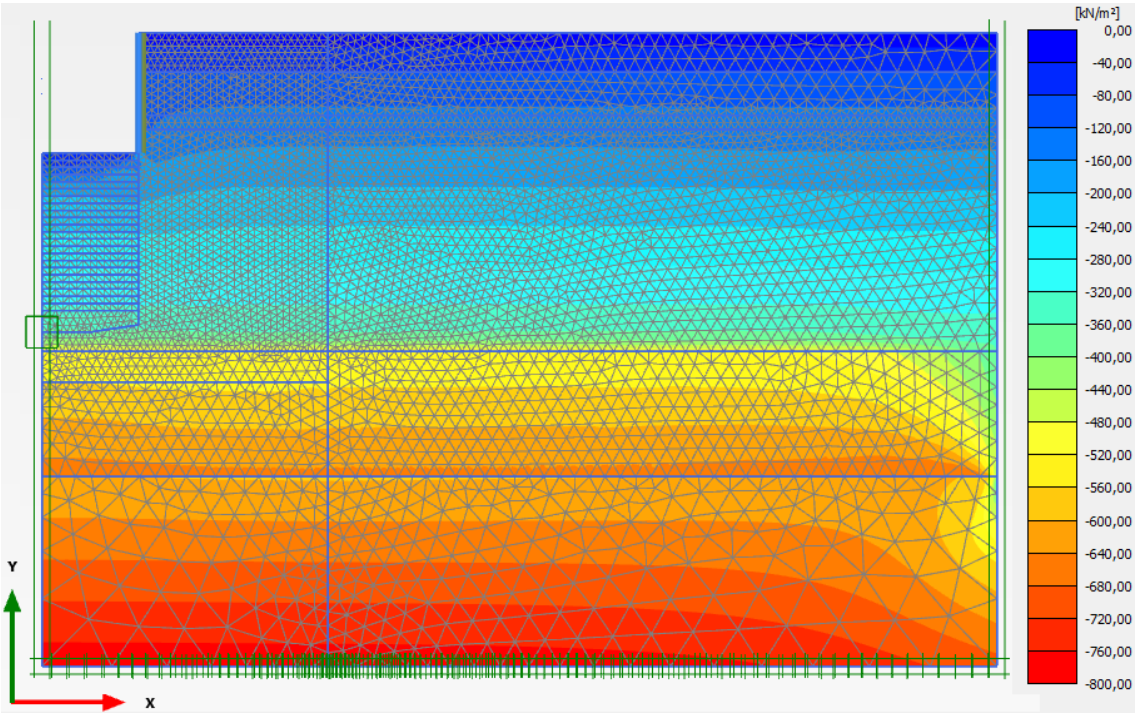

Figure A.26 Effective mean stress p' on an intermediate stage (scaled up $5E^{-3}$ times).
Max. value (blue, negative) = -15.85 kN/m² and Min. value (red, negative) = -783.5 kN/m²

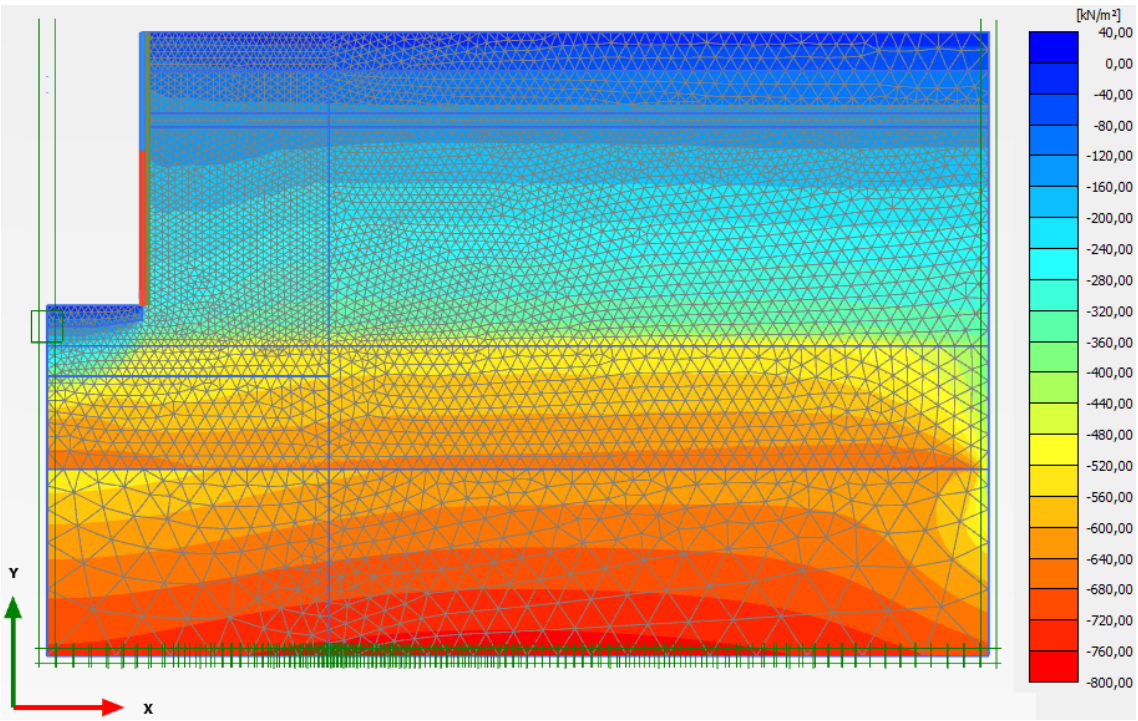

Figure A.27 Effective mean stress p' after the excavation ends (scaled up $5E^{-3}$ times).
Max. value (blue, positive) = 0.9607 kN/m² and Min. value (red, negative) = -786.3 kN/m²

It can be seen the deviatoric stress, q, on an intermediate stage and after the excavation ends, Figure A.28 and A.29.

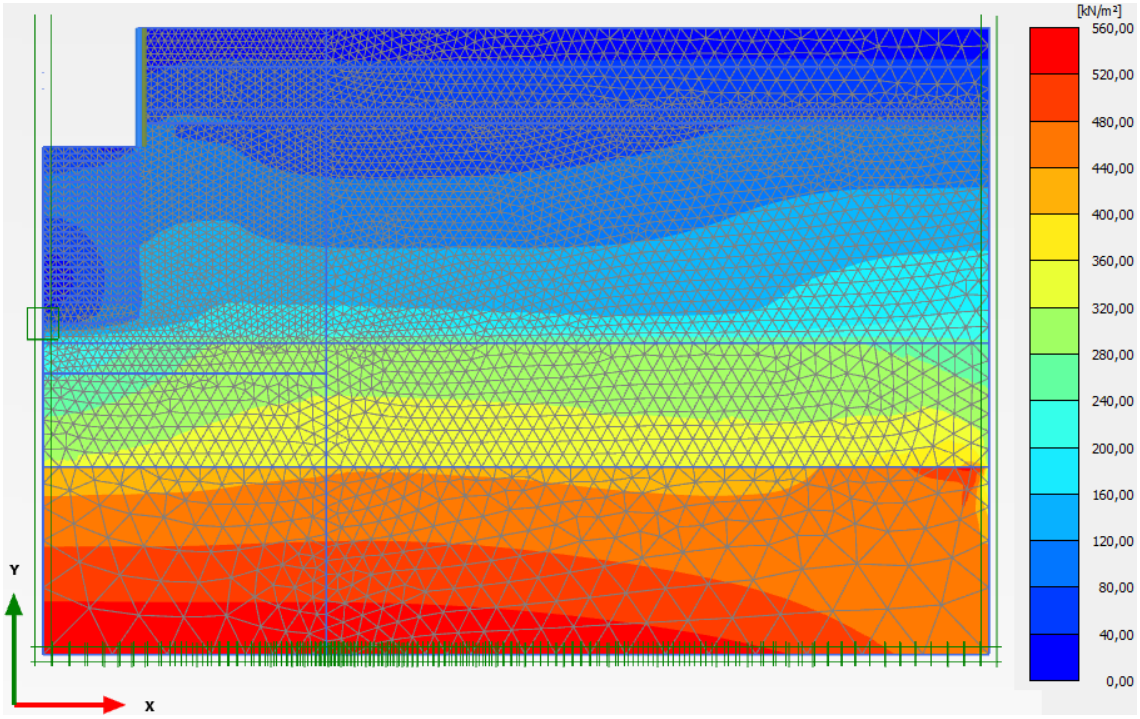

Figure A.28 Deviatoric stress q on an intermediate stage (scaled up $5E^{-3}$ times).
Max. value (red, positive) = 557.8 kN/m² and Min. value (blue, positive) = 1.278 kN/m²

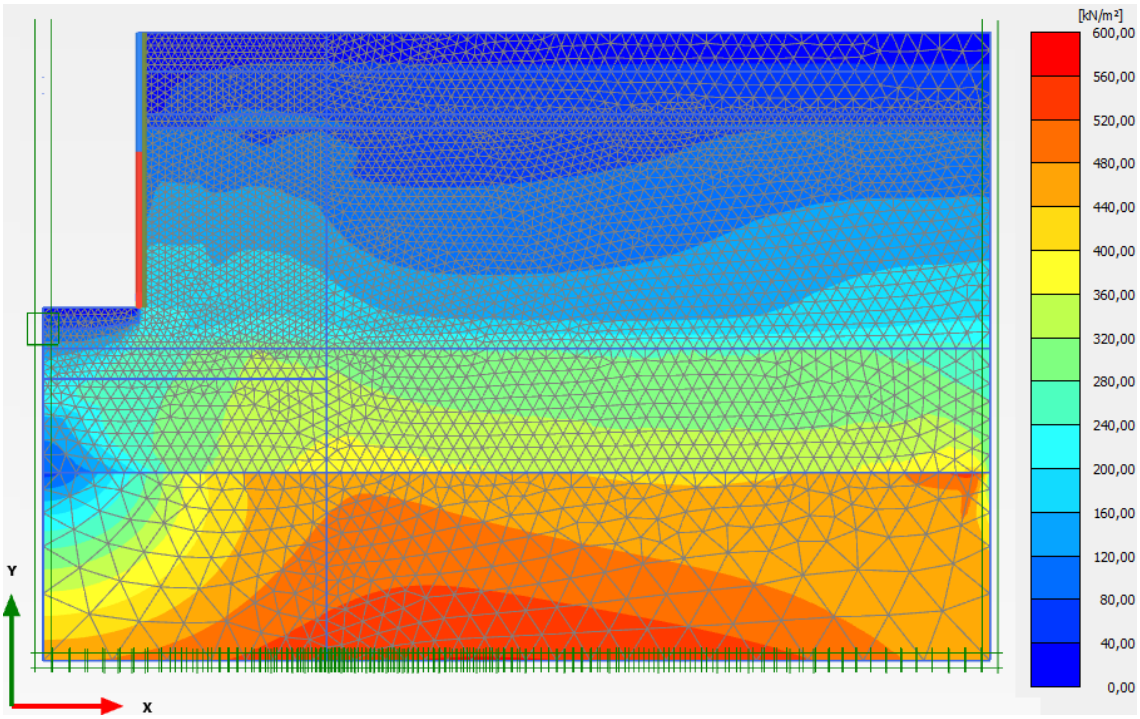

Figure A.29 Deviatoric stress q after the excavation ends (scaled up $5E^{-3}$ times).
Max. value (red, positive) = 562.4 kN/m² and Min. value (blue, positive) = 2.188 kN/m²

Total deviatoric strain

Figures A.30 and A.31 show the total deviatoric strain, γ_s, on an intermediate stage and after the excavation ends. It can be seen that maximum total deviatoric strain is generated under the lining wall when the construction method is excavation before support (EBS).

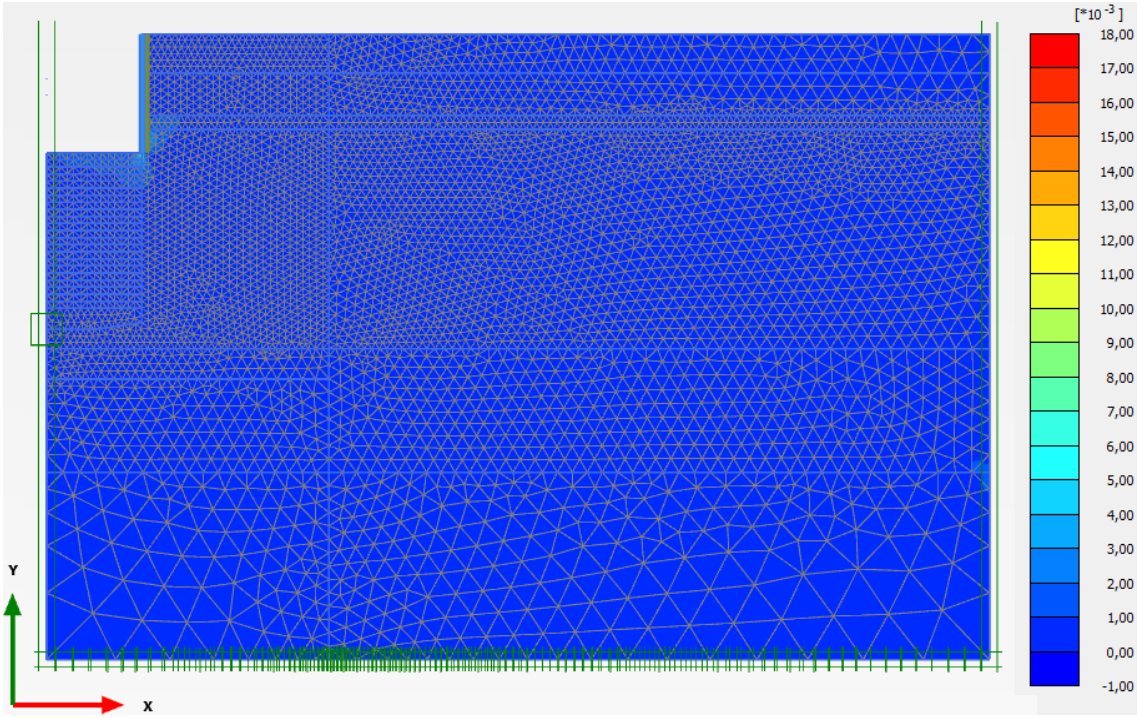

Figure A.30 Total deviatoric stain γ_s on an intermediate stage (scaled up 200 times). Max. value (blue, positive) = 0.01764 and Min. value (red, positive) = 5.452E^{-6}

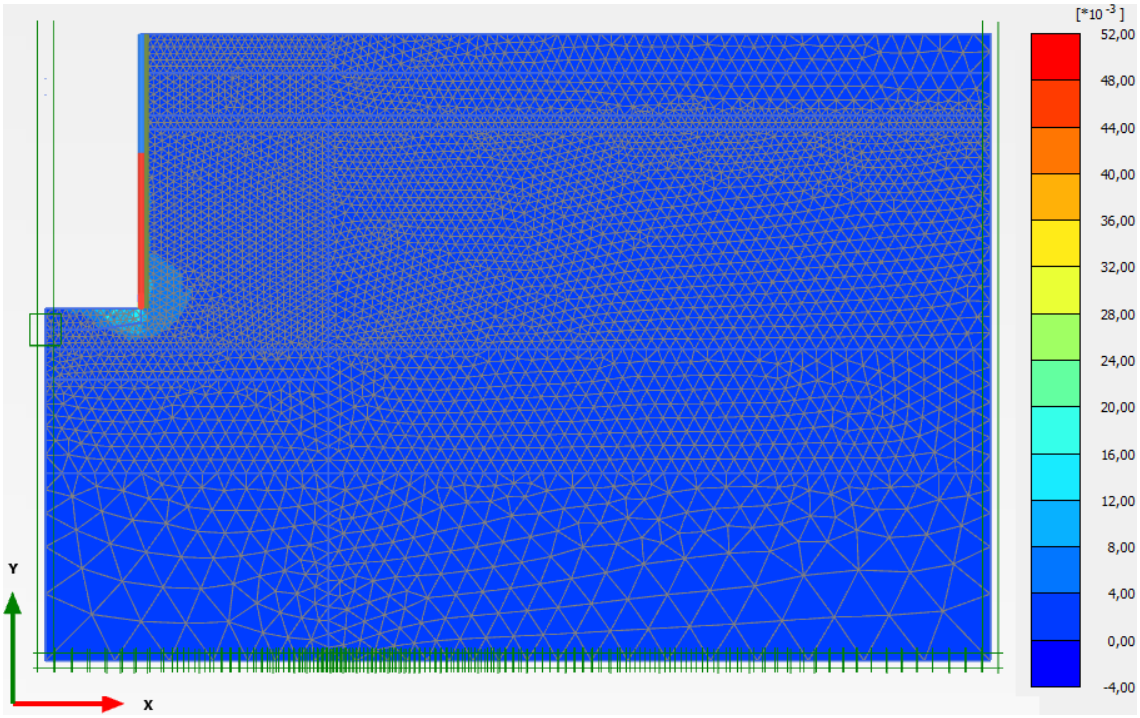

Figure A.31 Total deviatoric stain γ_s after the excavation ends (scaled up 200 times). Max. value (blue, positive) = 0.05035 and Min. value (red, positive) = 8.766E^{-6}

Groundwater pressure

Figures A.32 and A.33 show the pore water pressure, p_{water}, on an intermediate stage and after the excavation ends. It can be seen that the pore water pressure on the passive side of the wall is increasing during the excavation progress. After the excavation ends, the pore water pressure increases behind the wall, in the active side of the wall.

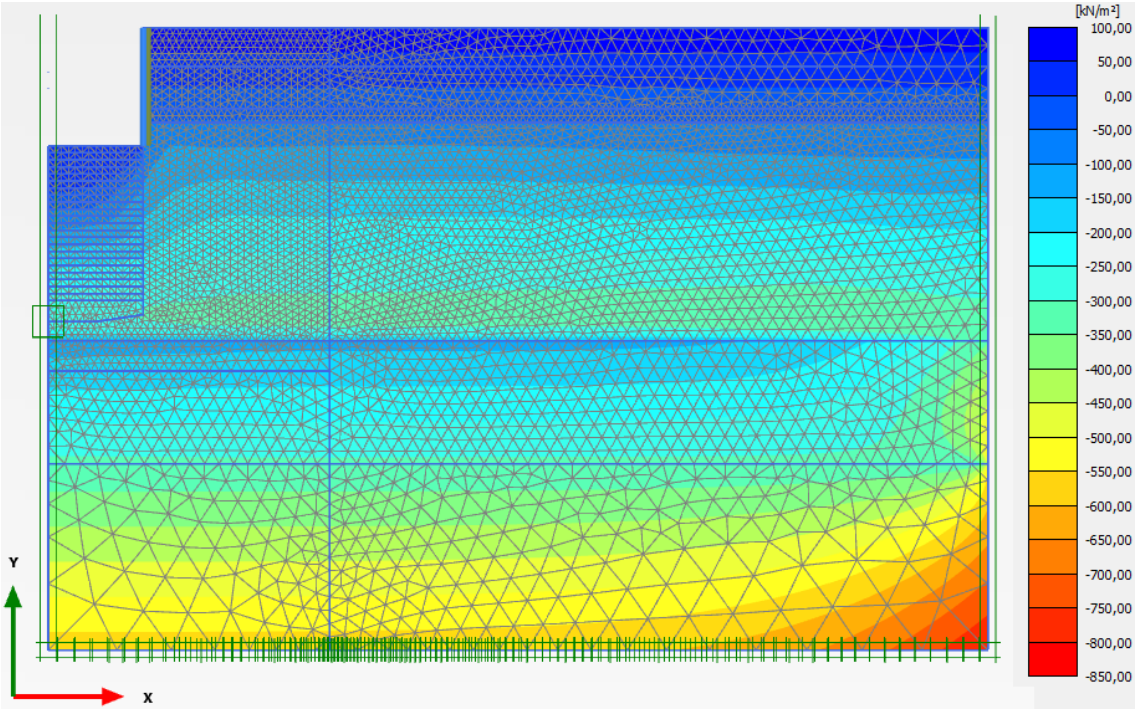

Figure A.32 Pore water pressure p_{water} on an intermediate stage (scaled up $5E^{-3}$ times) (Pressure = negative). Max. value (blue, positive) = 85.0 kN/m² and Min. value (red, negative) = -800.1 kN/m²

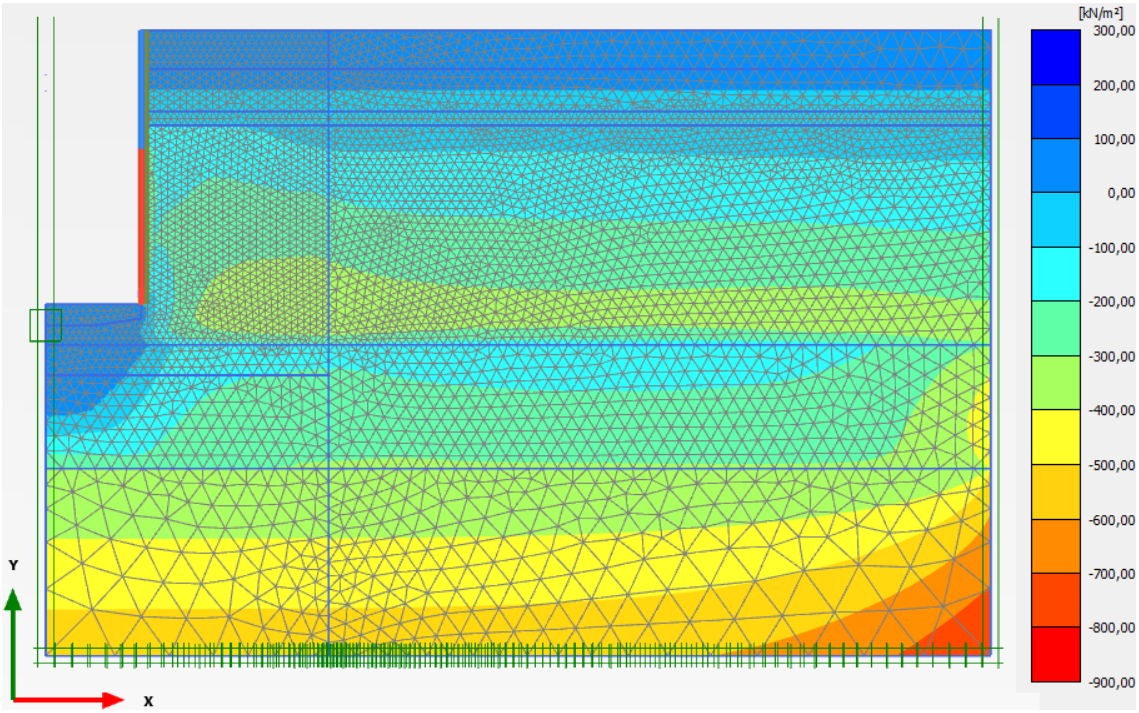

Figure A.33 Pore water pressure p_{water} after the excavation ends (scaled up $5E^{-3}$ times) (Pressure = negative). Max. value (blue, positive) = 224.3 kN/m² and Min. value (red, negative) = -852.9 kN/m²